BOUNCING AND COALESCENCE OF BINARY DROPLETS UNDERGOING OFF-CENTER COLLISIONS: A NUMERICAL STUDY BASED ON VOLUME-OF-FLUID METHOD

CHENGMING HE

PhD

The Hong Kong Polytechnic University

2020

The Hong Kong Polytechnic University

Department of Mechanical Engineering

Bouncing and Coalescence of Binary Droplets Undergoing Off-center Collisions: A Numerical Study Based on Volume-of-fluid Method

Chengming He

A thesis submitted in partial fulfillment of the

requirements for the degree of Doctor of Philosophy

July 2019

CERTIFICATE OF ORIGINALITY

I hereby declare that this thesis is my own work and that, to the best of my knowledge and belief, it reproduces no material previously published or written, nor material that has been accepted for the award of any other degree of diploma, except where due acknowledgement has been made in the text.

__________________________ (Signed)

______He Chengming_______(Name of student)

Abstract

Binary droplet collision in gaseous environment is of relevance to many natural and industrial processes, which has been studied substantially to probe more complicated physics in the context of various spray processes. Compared to the extensively studied head-on droplet collision, the thesis attempts to focus on the three-dimensional (3D) off-center droplet collision, which is more general and practical but less investigated, and strives to numerically reveal both macroscopic and microscopic dynamics for bouncing and coalescence based on a volume-of-fluid (VOF) method. There are four parts in the thesis.

1. Considering the facts that the elevated pressure environment promotes droplet bouncing in the real combustion chambers, and to serve for the modeling of Lagrangian simulations of sprays, the off-center collision of binary bouncing droplets of equal size was studied numerically by a volume-of-fluid (VOF) method with two marker functions. A non-monotonic kinetic energy recovery with varying impact parameters was discovered, and it can be explained by the prolonged entanglement time and the enhanced internal-flow-induced viscous dissipation for bouncing droplets at intermediate impact parameters.

2. The collision between initially spinning droplets, which occurs frequently in the practical sprays but is generally ignored in the previous studies, was numerically studied, with emphasis on the influences of rotation axis of spinning droplet on the droplet collision dynamics. The helicity analysis can be used to describe the "orthogonality" of droplets translational and spinning motions.
3. To help understand the non-monotonic ignition delay time with impact parameters for the collision between two hypergolic ignition droplets, the off-center coalescence between two nonreactive droplets of unequal sizes were numerically studied. A general non-monotonic internal mass entanglement with varying the impact parameter was observed, which verifies that the ignition process upon the collision between two hypergolic ignition droplets is probably dominated by the internal mass entanglement in the preliminary collision stage.
4. The internal mass entanglement, also referred as jet-like internal "mixing", were analyzed to be attributed to a main vortex ring generated during the binary droplet coalescence, which was motivated by the vortex-ring generation during droplet colliding with liquid pool. The correlation between the main vortex ring and the jet-like "mixing" were verified and presented by using a vortex-ring-based Reynolds number.

Publications Arising from the Thesis

[1] **He C.**, Xia X., Zhang P.*, Vortex-dynamical implications of nonmonotonic viscous dissipation of off-center droplet bouncing, Physics of Fluids, 2020.32(3): 032004.

[2] **He C.**, Xia X., Zhang P.*, Non-monotonic viscous dissipation of bouncing droplets undergoing off-center collision. Physics of Fluids, 2019. 31(5): 052004.

[3] Zhang D., **He C.**, Zhang P. *, Tang C., Mass interminglement and hypergolic ignition of TMEDA and WFNA droplets by off-center collision. Combustion and Flame, 2018. 197: 276. (co-first author)

[4] Xia X., **He C.**, Yu D., Zhao J.,Zhang P.*, Vortex-ring-induced internal mixing upon the coalescence of initially stationary droplets. Physical Review Fluids, 2017. 2(11): p. 113607. (co-first author)

[5]. **He C.**, Zhang P.*, Dynamics of binary droplet collision in gaseous environment, SCIENTIA SINICA Physica, Mechanica & Astronomica, 2017. 47(7): 070013. (review paper)

[6] **He C.**, Zhang P.*, A Computational Study of Spinning Effects on Bouncing and Coalescence of Head-on Colliding Droplets, Physics of Fluids (to be submitted)

[7]. **He C.**, Zhao J., Yu D., Zhang P., Unequal-size Droplet Collison and Internal Mixing, Proceedings of the 8th European Combustion Meeting, 18-21 April 2017, Dubrovnik, Croatia.

Acknowledgements

First, I would like to express my sincere gratitude to my supervisor, Prof. Peng Zhang, for his tremendous supports during my entire PhD study period. His insightful opinions always help me reach the essence of the problems and keep my research on the right track. It is very lucky for all our group members who have realized the rigorous scientific research attitudes under the active influences of Prof. Zhang's enthusiastic research spirits.

I would like also to thank my co-supervisor, Dr. Randolph C.K. Leung for his kind help with my research. Great thanks are owed to the department staffs that provide help and decent working place for my PhD study.

Special thanks should also be given to Prof. Xi Xia for his great help in the results analysis. I would like also to thank Dr. Dawei Zhang for our cooperation work, and all my group members, Prof. Zhenyu Zhang, Dr. Xuren Zhu, Dr. Dehai Yu, Dr. Kun Wu, and Mr. Yicheng Chi, who helped me during my Ph.D. study period.

Finally, I would like to express my full love to all my families for their unreserved supports in my life. Hope best for all of them.

Nomenclature

Physical quantities

A_H	Hamaker constant
D	Droplet diameter
E_k	Kinetic energy
f_E	Kinetic energy dissipation factor
h	Gas film thickness
k_B	Boltzmann constant
p	Pressure
R	Droplet radius
S	Surface area
t	Physical time
t_{osc}	Characteristic oscillation time
U	Experimental relative velocity between two colliding droplets
V	Volume of fluid droplets
α	Mass diffusivity
θ	Angle between rotation axis and defined x-axis
λ	Mean free path
μ	Dynamic viscosity
ρ	Density
σ	Surface tension coefficient
ϕ	Viscous dissipation rate
χ	Projection of the mass center connection line in the direction perpendicular to U
ω	Angular velocity

Mathematical and numerical parameters

c	Volume fraction
C	Time-dependent dye function concentration φ in the merged droplet
C_0	Dye function concentration φ in the initially unmixed droplets
C_∞	Dye function concentration φ in the fully mixed droplets
$\boldsymbol{D}$	Deformation tensor
f	Volume-of-fluid (VOF) function
H	Heaviside function
N	Mesh refinement level
$\boldsymbol{n}$	Normal to the local interface
$\boldsymbol{t}$	Shear to the local interface
$\boldsymbol{u} = (u, v, w)$	Velocity vector
δ_s	Dirac delta function
κ	Local curvature
φ	Mass dye function with $\varphi = 1$ in the smaller droplet otherwise $\varphi = 0$
$\boldsymbol{\omega}$	Vorticity

Non-dimensional and normalized variables

B	Impact parameter, $B = 2\chi/(D_S + D_L)$
Ca	Capillary number, $Ca = \mu_S U/\sigma_S$
Kn	Knudsen number, $Kn = \lambda/h$
M	mixing index, $M = 1 - \left(\int_V \lvert C - C_\infty \rvert H(f-1) dV\right) / \left(\int_V \lvert C_0 - C_\infty \rvert H(f-1) dV\right)$
Oh	Ohnesorge number, $Oh = \mu_S/\sqrt{\rho_S D_S \sigma_S}$
Pe	Peclet number, $Pe = UD_L/\alpha$
Re	Reynolds number, $Re = \rho_S U D_S/\mu_S$

T	Non-dimensional time, $T = t/t_{osc}$
We	Weber number, $We = \rho_S D_S U^2/\sigma_S$
We^*	Symmetry weber number, $We^* = \Delta^3 We/[12(1+\Delta^3)(1+\Delta^2)]$
Δ	Size ratio of the larger droplet to the smaller droplet, $\Delta = D_L/D_S$

Subscripts

cr	Critical value
c	Values of characteristic scale
eff	Effective quantity, for example effective viscosity
g	Fluid properties of the surrounding gas (air) environment
L	Fluid properties of the larger droplet
ref	Reference value
S	Fluid properties of the smaller droplet
0	Values at the initial instant
∞	Infinity, for example infinity-shear viscosity

Table of Contents

List of Figures

List of Tables

1 Introduction

1.1 Background

Binary droplet collision in gaseous environment is of relevance to many natural and industrial processes, such as raindrop formation, ink-jet printing[1], spray combustion[2, 3], hypergolic ignition in rocket propulsion system, droplet manipulation in microfluidics[4, 5], and various applications involving functional interfaces[6-9] in materials science. Specifically, the coalescence and breakup of cloud droplets during the falling process account for the mechanisms of raindrop formation. In the spray combustion of diesel engines, the nozzle jet flow breaks up and generates a mass of fuel droplets that collide with each other under the turbulence flow in the combustion chamber, and their distributions of size, number density, velocity, and subsequent evaporation and combustion processes are accordingly influenced. In the rocket propulsion system, the hypergolic ignition process highly depends on the propellent droplet deformation, the internal mass mixing, and the subsequent chemical reactions in the liquid phase. Similarly, in the biochemical engineering, microscale droplets with micro reactants are often used as reaction carriers in which the droplet coalescence and subsequent internal mixing process are vital for the reaction control.

Generally, binary droplet collision in the sprays occurs with the droplet diameter less than one millimeter and the colliding process within several milliseconds. Thus, experimental observations and measurements on that such small length scale and short time scale heavily rely on high speed camera with high-resolution lens. As early as 1977, Bradley and Stow[10] performed an experiment of the collision between two water droplets. Thereafter, a large number of experimental studies on the binary droplet collision have been reported in the literature and summarized in a few excellent reviews[11, 12].

Collision outcomes between two droplets of equal size as increasing the relative impact inertia, such as coalescence, bouncing, separation, and splashing, can be phenomenologically described as follows. Impact inertia drives the interfaces to approach and thereby a squeezed gas film simultaneously forms by the entrained gas. Once the gas film thickness has reached the scale of hundreds of angstroms, the intermolecular (Van der Waals) attractive force[13] becomes dominant, pulls the droplet interfaces closer, and finally leads to interface merge. When the impact inertia is small, the sufficient time for the drainage of entrapped gas allows the gas film thickness to approach to the scale in which Van der Waals force becomes effective and finally leads to droplet coalescence. As increasing the impact inertia, the time of gas drainage process is comparable to that of droplet deformation, and droplet interfaces tend to bounce off if the gas film thickness cannot reach Van der Waals scale. As further increasing the impact inertia, the inertia force can overcome the gas film resistance and merge the interfaces forcedly, meanwhile a small bubble forms by the entrapped gas. The minor bubble entrapment is a general phenomenon during the binary droplet collision that has been observed in the previous experiments, as shown in Figure 1.1. When the impact inertia is large enough exceeding the surface tension restraint and cannot be consumed by the inner viscous dissipation, the droplet separation occurs followed by the droplet coalescence with large deformation. As further increasing the impact inertia to an extreme high level, the splashing happens and generates numerous small children droplets induced by the capillary instability of the formed thin liquid film.

Binary droplet collision in gaseous environment is a multi-scale, multi-physics, and nonlinear problem. The droplet diameter is sub-millimeter scale whereas the gas film thickness can be as small as 10 nanometers, and the mean free path of air gas in 1 atm is around 100 nanometers. It is apparently seen that the multi-physics flow between the gas film – ranging from continuous flow, slip flow, transition flow, and free molecular flow. Meanwhile, the problem becomes nonlinear owing to the large droplet deformation after inelastic collisions and the induced internal viscous flow.

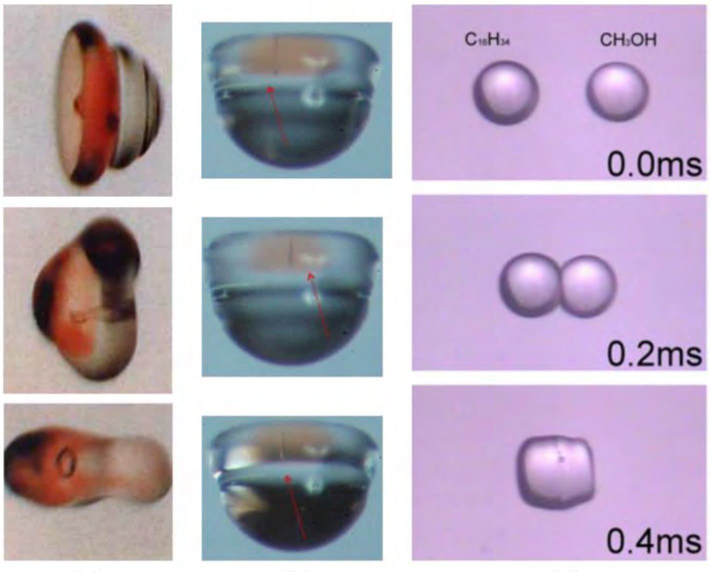

(a) (b) (c)

Figure 1.1 Enlarged photographs adapted from (a) Ashgriz and Poo[14], (b) Tang *et al.*[15], and (c) Wang *et al.*[16] showing trapped air bubbles during binary droplet collision.

Experimental, theoretical, and numerical methods are all indispensable to study binary droplet collision. The theoretical analysis, such as an energy balance or a force/momentum balance, can obtain some qualitative findings based on the assumptions and simplified models, but they are not adequate to study the complicated problem. For the experimental methods, the stable droplet generation, the controllability of the collision parameters (for example collision velocity and angle), and the high-quality images of droplet deformation have been well developed in the previous experimental studies. However, the flow field visualization and measurement are still challenging currently. For the available numerical methods, they can help to analyze the microscopic flow field once the numerical simulations have been sufficiently validated by experimental observations. But it is noted that the numerical method cannot predict the droplet collision outcomes from the first principle if not considering the lubrication layer theory, rarefied gas effects, and Van der Waals force[17]. Overall, binary droplet collision is the simplest case but of significance to the fundamental understanding of the complex spray processes.

1.2 Research objectives

Experimental observation is a direct method to discover and describe the macroscopic characteristics of collision outcomes between binary droplets. However, simply experimental observations are difficult to describe the microscopic characteristics of the inner flow upon the droplet collision since the droplet size in the sprays is as small as $O(100)$ micrometers or even smaller. Thus, in the present thesis, the numerical methods with sufficient validations by experiments are mainly concerned for the fundamental understanding of the collision dynamics between binary droplets.

The numerical method solves the unsteady, incompressible, and variable-density Navier-Stokes equations with surface tension. The Volume-of-fluid (VOF) method was adopted to track the free interface, which has been implemented in an open source code, Gerris[18, 19], featuring the quadtree/octree adaptive mesh refinement, the geometrical VOF interface reconstruction, and continuum surface force (CSF) with height function curvature estimation.

Compared to the extensively studied head-on collisions in the literatures, the present study attempts to focus on the three-dimensional (3D) off-center collisions between binary droplets, which is more general and practical but less investigated. However, 3D numerical simulations substantially increase the computational cost so that sometimes it is unpractical to set a large number of calculations. To circumvent these difficulties, the numerical methods have been modified according to the specific physical problems, such as the multiple VOF functions and collision-oriented adaptive mesh refinement technics.

The overarching objective of the present thesis is to study impact parameter effects on off-center droplet collisions: coalescence and bouncing. The specific objectives can be summarized as follows:

(1) To model 3D droplet bouncing in Lagrangian simulation of sprays, because the elevated pressure in the real engine conditions promotes droplet bouncing. A practically useful formula correlating the kinetic energy dissipation factor with the impact parameter for various Weber numbers and Ohnesorge numbers was desired.

(2) To understand the collision dynamics between two droplets with initial self-rotations because the rotation effects are generally ignored in the literatures.

(3) To understand the effects of size ratio, Weber number, and impact parameter on the internal mass entanglement undergoing off-center droplet collision, and the correlation between the mass entanglement and hypergolic ignition for binary collision between reactive droplets.

(4) To understand the physical mechanism of the internal "mixing" associated with the formation of jet-like structure by vortex-dynamical interpretations.

1.3 Outline of thesis

In the present work, a detailed literature review is introduced in Chapter 2. It includes the experimental observations on the binary collision between identical droplets, between droplets of unequal size, between droplets of different fluids (either miscible or immiscible), and between other (charged or reactive) droplets, followed by the theoretical analysis about the transitions between different collision outcomes in the regime diagram.

The methodology of the numerical scheme solving unsteady, incompressible, variable-density Navier-Stokes equation and the free interface tracking methods are introduced in Chapter 3, with particular emphasis on the Volume-of-Fluid (VOF) method.

The off-center collision of binary bouncing droplets of equal size was numerically studied by using a volume-of-fluid (VOF) method with two marker functions in Chapter 4. The numerical studies and helicity analysis on the binary collision between two initially spinning droplets were presented in Chapter 5. The off-center coalescence between two nonreactive droplets of unequal sizes were numerically studied in Chapter 6 for creating the correlation between the internal mass entanglement and the hypergolic ignition process. The coalescence between two initially stationary droplets were numerically studied in Chapter 7 with emphasis on the vortex-dynamical interpretations to explain the jet-like internal “mixing”. Finally, general conclusions and the future research interests in binary droplet collision are summarized in Chapter 8.

2 Literature review

2.1 Physical governing parameters

The dynamics of binary droplet collision in the isothermal static gas environment can be described by a variable set Q as

$$Q = f\left(U, \chi, D_S, \rho_S, \mu_S, \sigma_S, D_L, \rho_L, \mu_L, \sigma_L, \rho_g, \mu_g\right) \tag{2.1}$$

in which including 12 controlling parameters, namely the relative velocity U, the impact parameter χ (the projection of mass center distance in the direction perpendicular to the relative velocity), the diameter, D_S and D_L, density, ρ_S and ρ_L, viscosity, μ_S and μ_L, and surface tension coefficient, σ_S and σ_L, for small and large droplet respectively, the density ρ_g and viscosity μ_g for gas, as shown in Figure 2.1.

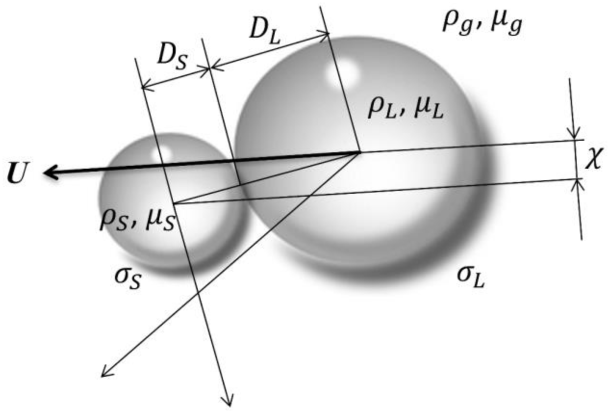

Figure 2.1 Schematic of binary droplet collision.

Then, choosing the diameter D_S, density ρ_S, and surface tension σ_S of small droplet (denoted by subscript 'S') as the basic units, a dimensionless variable $\tilde{Q}$ can be obtained as

$$\tilde{Q} = f\left(We, B, \Delta, Oh; \frac{\rho_L}{\rho_S}, \frac{\mu_L}{\mu_S}, \frac{\sigma_L}{\sigma_S}, \frac{\rho_g}{\rho_S}, \frac{\mu_g}{\mu_S}\right) \tag{2.2}$$

The Weber number is defined as

$$We = \frac{\rho_S D_S U^2}{\sigma_S} \tag{2.3}$$

representing the ratio of droplet inertial force to surface tension force.

The impact parameter is defined as

$$B = \frac{2\chi}{D_S + D_L} \tag{2.4}$$

characterizing the mass center deviation of the off-center collision ($0.0 < B < 1.0$) to the head-on collision ($B = 0.0$), in which $B \geq 1.0$ denotes the grazing collision that two droplets cannot collide.

The Ohnesorge number is defined as

$$Oh = \frac{\mu_S}{\sqrt{\rho_S D_S \sigma_S}} \tag{2.5}$$

representing the ratio of droplet viscous force to surface tension force. It is noted that the Oh number is still valid for describing the collision between non-Newtonian droplets except that it is local shear-rate-dependent but not a constant.

The size ratio is defined as

$$\Delta = \frac{D_L}{D_S} \tag{2.6}$$

The Reynolds number is defined as

$$Re = \frac{\rho_S U D_S}{\mu_S} \tag{2.7}$$

that can be calculated by Oh and We as $Re = \sqrt{We}/Oh$, thus it will not be presented as an independent parameter in the present thesis.

The other five parameters affecting the binary droplet collision can be justified based on the following considerations. The density ratio ρ_L/ρ_S, viscosity ratio μ_L/μ_S, and surface tension ratio σ_L/σ_S describe the fluid properties of small and large droplets, and they are unity if considering the simplest case of the collision between two identical droplets. The surface tension difference $(\sigma_L/\sigma_S \neq 1)$ between two miscible droplets can induce the Marangoni effects upon droplet coalescence. In addition, the gas-fluid density ratio and viscosity ratio are approximately of the order of $\rho_g/\rho_S \sim O(10^{-3})$ and $\mu_g/\mu_S \sim O(10^{-2})$, respectively. They have insignificant influences on the binary droplet collision with values in that small ranges[15, 20-23], however, they are increasingly effective when the density and viscosity of gas are comparable to that of fluids.

Consequently, the Weber number We, the impact parameter B, the Ohnesorge number Oh (or Reynolds number Re), and the size ratio Δ are four primary parameters that frequently discussed in the present binary droplet collision problems.

2.2 Binary collision between identical droplets

A nomogram in the $We - B$ parameter space[24, 25] was proposed for the binary collision between identical droplets: (I) coalescence after minor deformation, (II) bouncing, (III) coalescence after substantial deformation, (IV) coalescence followed by separation for near head-on collisions, (V) coalescence followed by separation for off-center collisions, and (VI) splashing at extreme large $We \sim O(10^2)$, as the schematic regime and experimental images shown in Figure 2.2.

In the context of raindrop formation, the earlier studies were focused on the collision between two water droplets in atmosphere air[14, 25-28].[14, 25-28]. Figure 2.3(a) shows the $We - B$ collision regime diagram between two identical water droplets. Ashgriz and Poo[14] observed three collision outcomes: droplet permanent coalescence at small We and either reflexive separation (at small B) or stretching separation (at large B) at large We. Qian and Law[25] also found bouncing between two water droplets at relative larger B for near grazing collisions. Rabe *et al.*[28] yielded the similar results as Ashgriz and Poo without observing the phenomenon of droplet bouncing.

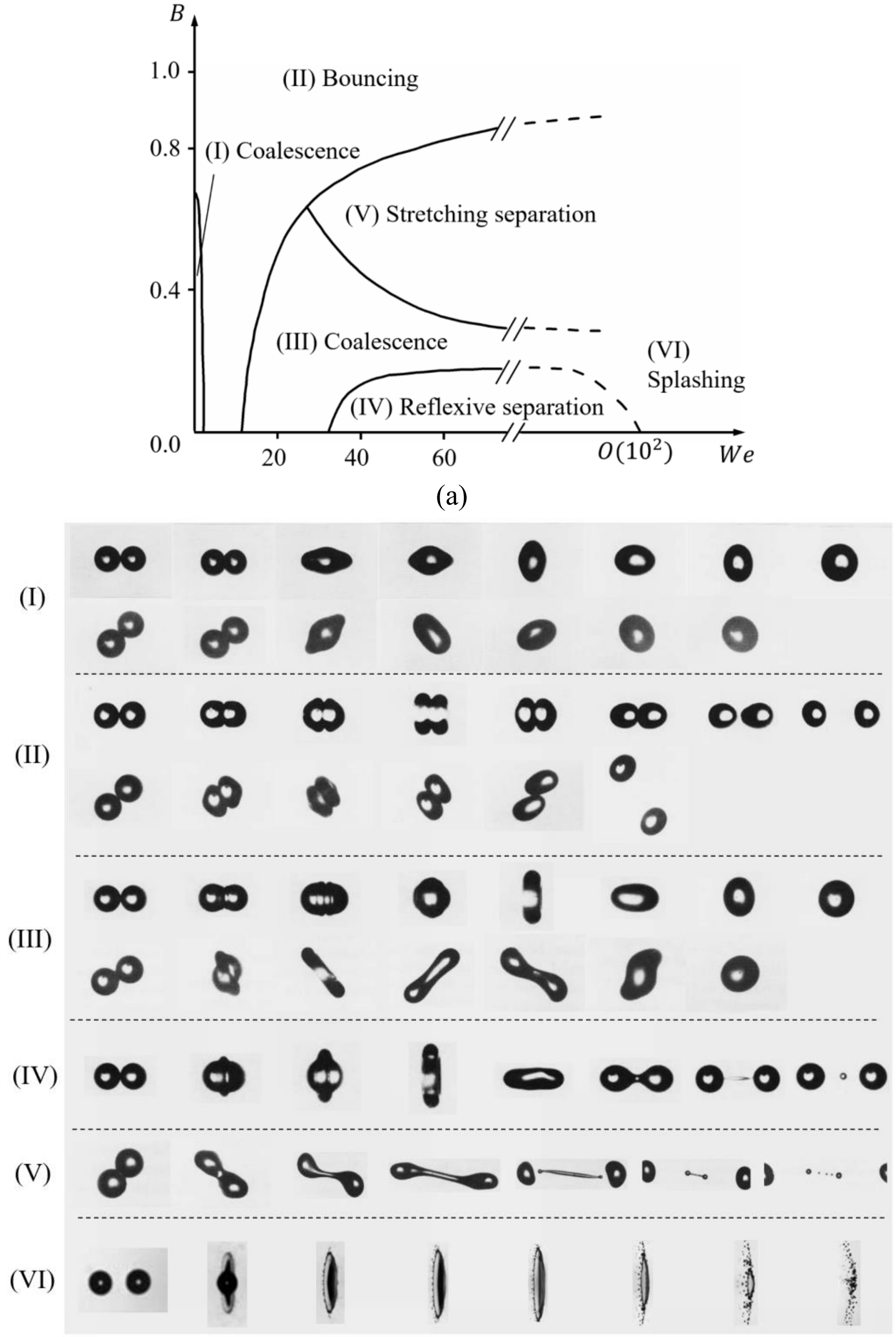

(a)

(b)

Figure 2.2 (a) Sketched regime nomogram and (b) experimental images[24] (first row for head-on collisions and second row for off-center collisions) for binary collision between identical droplets: (I) coalescence ($We = 0.19$), (II) bouncing ($We = 3.6$), (III) coalescence ($We = 13.4$), (IV) reflexive separation ($We = 45.6$), (V) stretching separation ($We = 54.3$), and (VI) splashing[29] ($We = 1593$).

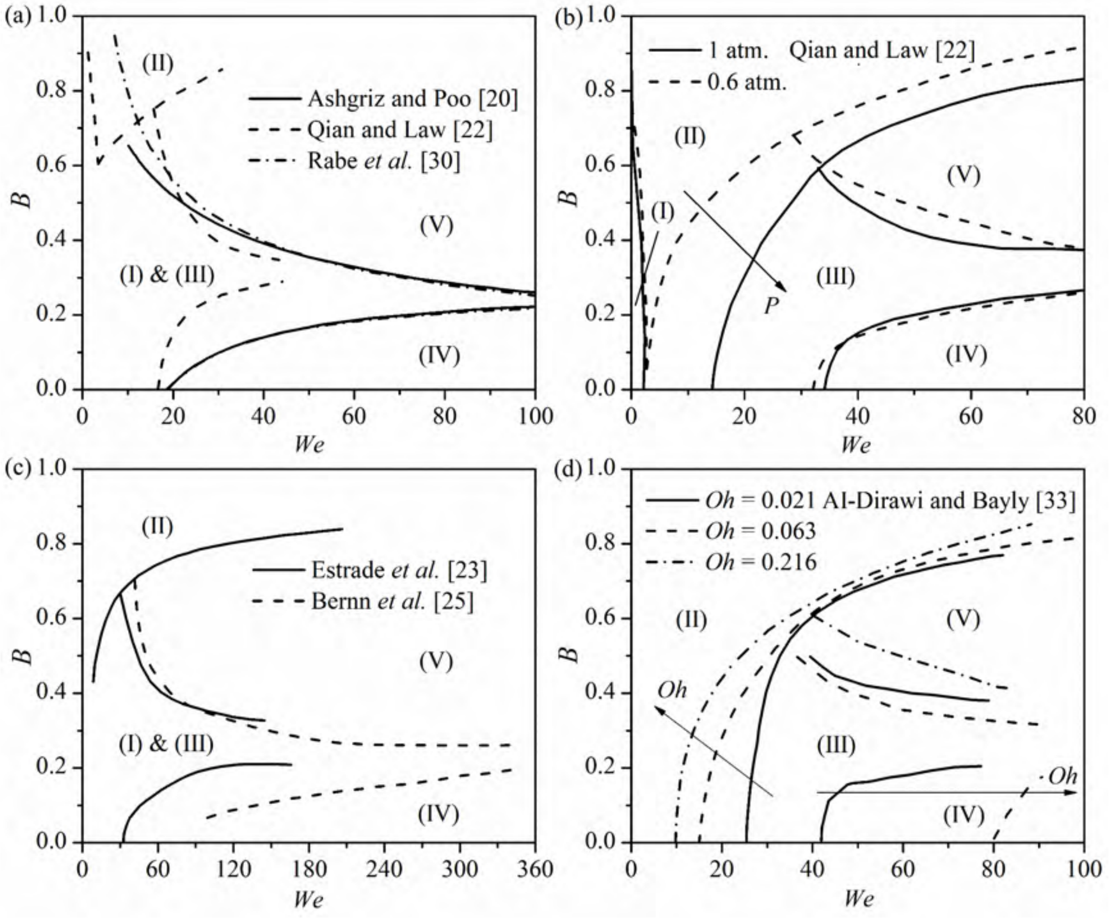

Figure 2.3 $We - B$ regime diagram for the binary collision between identical droplets: (a) water, (b) alkanes, (c) organics, and (d) high-viscosity aqueous solution.

However, the collision behaviors of hydrocarbon droplets are significantly more complex than that of water droplets. Motivated to understand the dense spray of fuel droplets in real engine conditions, Law and coworkers systematically studied the collision dynamics between hydrocarbon (such as n-heptane, n-decane, n-dodecane, n-tetradecane, and n-hexadecane) droplets in various gaseous environments (air, nitrogen, helium and ethylene) with different pressures in the range of 0.6 ~ 12 atm. Figure 2.3(b) shows the $We - B$ collision regime diagram between two identical alkane droplets in 1 atm. nitrogen environment. Jiang *et al.*[24], and Qian and Law[25] found that the head-on collision occurs bouncing phenomenon for tetradecane droplets whereas only permanent coalescence for water droplets, showing a nonmonotonic transition from coalescence after minor deformation (I) to bouncing (II) and to coalescence after substantial deformation (III) as increasing We. Furthermore, their results also show that the regime boundaries between different collision outcomes can be significantly affected by the properties of the ambient gas, such as the gas pressure, gas molecular weight and viscosity, and gas molecular structures. More specifically, for head-on droplet collisions, bouncing for alkane droplets is absent at lower pressures, as the regime diagram at 0.6 atm shown in Figure 2.3(b), although it is observed at atmospheric pressure. Similarly, the bouncing phenomena can be observed for water droplets at higher pressures although it is absent at atmospheric pressure, which indicates that increasing gas pressure promotes bouncing while decreasing pressure promotes coalescence. The substantiating experimental results also indicate that the liquid vapor enrichment promotes droplet merging. In the recent years, more comprehensive studies about the gas environment effects on the binary droplet collision have been performed extensively.

Figure 2.3(c) shows the $We-B$ collision regime diagram between two identical droplets of organics in atmosphere air. Estrade *et al.*[30] studied the collision regime between two ethanol droplets, which is similar to that of water droplets. Brenn *et al.*[31] focused on the collision regime of separation between two propanol droplets and studied the number of satellite droplets formation. They reported that different droplet sizes (i.e. different Oh) lead to different results of satellite droplet formation even at same We and B, which implies that Oh effect is a significant factor to the droplet collision but has often been missed in the current $We-B$ nomogram. Willis and Orme[32, 33] studied the stretching deformation after the collision between two silicon-based oil droplets under vacuum environment and found that it became difficult to observe droplet separation, in which the critical We for the transition between coalescence and separation is nearly 100 times larger than that of water droplets under atmosphere air.

Figure 2.3(d) shows the $We-B$ collision regime diagram between two identical droplets of high-viscosity aqueous solution. The deviation between collision regimes in $We-B$ parameter space is attributed to the ignored Oh effects. In fact, it is difficult to experimentally change Oh among a wider range but with other parameters remain unchanged. This is because for a certain fluid Oh only depends on the droplet diameter, and the droplet with large diameter is hard to be spherical while small diameter is hard to be generated. Thus, the high-viscosity aqueous solution produced by adding additives into water allows us to easily study the Oh effects on the binary droplet collision. In recent ten years, Gotaas *et al.*[34]

Sommerfeld and Kuschel[35], Finotello *et al.*[36], and AI-Dirawi and Bayly[37] studied the effects of viscosity on the collision regime transitions with Oh in a wider range of $0.021\sim0.44$. It is observed in Figure 2.3(d) that, as increasing Oh, the regime boundary between bouncing (II) and coalescence (III) moves towards smaller Oh, the regime boundary between coalescence (III) and reflexive separation (IV) moves towards larger Oh for near head-on collisions, and the regime boundaries between stretching separation (V) and either bouncing (II) or coalescence (III) are insensitive to the variation of Oh for off-center collisions.

Overall, a complete regime nomogram for the binary collision between identical droplets ($\varDelta = 1.0$) should be in the three-dimensional $We - B - Oh$ parameters space. The comprehensive studies on the transitions between different collision outcomes are benefit to the modelling of binary droplet collision that serves for the Lagrangian simulations of sprays. The classical O'Rourke model[38] and latter some other improved models by considering complex but complete collision outcomes have been studied extensively in the past years.

Furthermore, Table 2.1 summaries all the above discussed experimental studies for a quick reference to the readers, including the research interests and relevant experimental parameters.

Table 2.1 Summary of the previous experimental studies on the binary collision between identical droplets.

Year, Authors	Fluid properties	Drop diameter (μm)	Medium	We	B	Oh	Research interests
1968, Adam *et al.*[26]	water (charged)	120, 600	1 atm. air	2~100, 10~400	0.0~0.95	0.011, 0.0048	coalescence and separation
1972, Brazier-Smith *et al.*[27]	water	300~1500	1 atm. air	0.5~180	0.0~1.0	0.0030~0.0068	coalescence efficiency and criteria for separation
1989, Brenn and Frohn[39]	Propanol-2	70~200	1 atm. air	20~1000	0.0~1.0	0.042~0.071	droplet size effects on coalescence and separation
1990, Ashgriz and Poo[14]	water	200~1000	1 atm. air	1~100	0.0~1.0	0.0037~0.0083	theoretical prediction of reflexive and stretching separation
1992, Jiang *et al.*[24]	water, n-alkane	300	1 atm. air	0.1~100	0.0~1.0	0.0068~0.030	non-monotonic collision outcomes and theoretical model for reflexive and stretching separation
1997, Qian and Law[25]	water, tetredecane	200~400	0.6~12 atm. air, nitrogen	0.2~100	0.0~1.0	0.0059~0.036	effects of ambient gas (pressure, viscosity, and molecular structure)
1999, Estrade *et al.*[30]	ethanol	80~300	1 atm. air	10~200	0.0~1.0	0.017~0.032	theoretical prediction of bouncing

2003, Willis and Orme[33]	silicon-based oils	467	vacuum	300~4000	0.0	0.07~0.22	viscosity effects on droplet maximum deformation
2006, Brenn *et al.*[31]	propanol-2	60~140	1 atm. air	40~280	0.0~1.0	0.050~0.077	size effects on droplet breakup and instability
2007, Roth *et al.*[40]	water	220	1 atm. air	500~2600	0.0~1.0	0.0079	collision outcomes at high We
2007, Gotaas *et al.*[34]	n-decane, MEG, DEG	324~375	1 atm. air	13.6~316	0.0~1.0	0.012~0.35	viscosity effects on droplet collision
2008, Pan *et al.*[41]	tetradecane	200~340	1 atm. air	2.3~13.6	0.0	0.028~0.036	energy budget for droplet coalescence and bouncing
2009, Pan *et al.*[29]	water, alkane, and glycerin	700~1200	1 atm. air	50~5100	0.0	0.0033~0.011	droplet splattering at extreme high We
2010, Rabe *et al.*[28]	water	220~450	1 atm. air	20~280	0.0~1.0	0.0055~0.0079	regime nomogram in $We_c - B$ (symmetry We_c)
2016, Sommerfeld and Kuschel [35]	alcohols and PVP K30, and sucrose	380	1 atm. air	0~100	0.0~1.0	0.049~0.37	modeling of droplet collision outcomes for different viscosities
2018, Finotello *et al.*[36]	glycerol-water	700	1 atm. air	0~100	0.0~1.0	0.021, 0.064, 0.38	viscosity effects on droplet collision
2019, AI-Dirawi and Bayly [37]	2%, 4%, 8% HPMC	360~390	1 atm. air	0~100	0.0~1.0	0.021, 0.063, 0.22	a new model for bouncing regime

2.3 Binary collision between droplets of unequal sizes

Binary collision between identical droplets is the specific case whereas the collision between two droplets of unequal sizes occurs frequently in the realistic situations. However, considering the size ratio effect (Δ) results in the collision regime nomogram too complicated to be a four-dimensional parameter space, i.e. $We - B - Oh - \Delta$. It is reasonable to analyze the collision outcomes by focusing on any three parameters as a variable set. And Oh effects on $We - B$ nomogram has been briefly discussed in Section 2.2.

2.3.1 Δ effects on $We - B$ nomogram

The symmetry of droplets deformation can be broken for the collision between two droplets of unequal sizes, as the early experimental images by Bradley and Stow[10] and Ashgriz and Poo[14] shown in Figure 2.4. Accordingly, the regime boundaries between different collision outcomes in $We - B$ parameter space are influenced by Δ. Figure 2.5 shows the similar results adapted from Ashgriz and Poo[14] and Rabe *et al.*[28] that the colliding droplets tend to merge with increasing the values of Δ, which is manifested by the enlarged area of the coalescence regime in $We - B$ nomogram with regime boundary between coalescence and reflexive separation moving towards smaller B whereas the boundary between coalescence and stretching separation moving towards larger B. Brazier-Smith *et al.*[27] explained that droplet separation is not so easily achieved for higher values of Δ (for fixed We and B) because less angular momentum is available to pull the two drops apart, and proposed a simple criterion for droplet separation based on energy considerations that the boundary between coalescence and separation is obtained by the same amount of rotational kinetic energy and surface energy required to form two drops. It then spawned the early studies on the prediction of size ratio effects on the coalescence-separation boundary in the aspects of energy balance (Ashgriz and Poo[14], Rabe *et al.*[28], and Estrade *et al.*[30]).

Figure 2.4 Experimental images of collision between two droplets of unequal sizes: water droplets of $\Delta = 1.41$, $We \approx 20$[10] at (a) $B = 0.0$ and (b) $B = 0.9$, and (c) water droplets of $\Delta = 2.0$, $We = 56$ and $B = 0.0$[14].

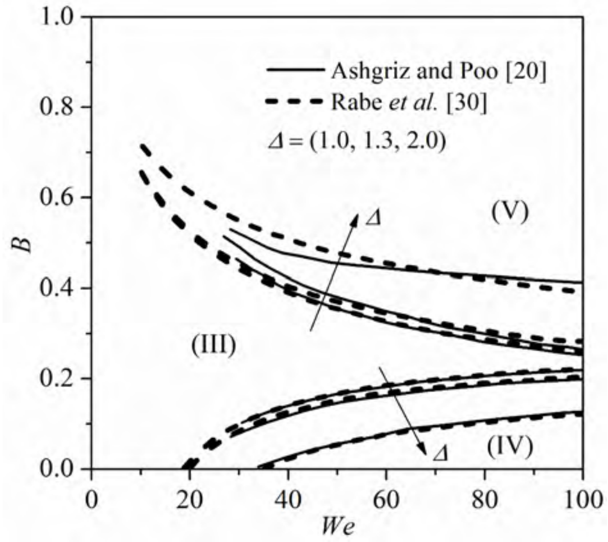

Figure 2.5 Variation of $We - B$ regime boundary for three difference size ratios, 1.0, 1.3, and 2.0, adapted from Ashgriz and Poo[14] ($Oh = 0.068$) and Rabe *et al.*[28] ($Oh = 0.055 \sim 0.078$).

2.3.2 Oh effects on $We - \Delta$ nomogram ($B = 0$)

Testik[42] and Tang *et al.*[43] mainly studied the head-on collision outcomes in the $We - \Delta$ parameter space for different fluids (equivalent to different Oh). Although droplet coalescence is promoted as increasing Δ, it is still observed bouncing and separation for the binary collision between two droplets of unequal sizes, as the experimental images adapted from Tang *et al.*[43] shown in Figure 2.6. $We - \Delta$ regime diagrams for head-on collisions between water, decane, and tetradecane droplets in Tang *et al.*[43] show that the critical We of the transition from bouncing (II) to coalescence (III) is slightly influenced by the Δ whereas the critical We of the transition from coalescence (III) to reflexive separation (IV) increases significantly with increasing Δ, which is understood as a results of the enhanced viscous dissipation with increasing Δ that thereby suppresses the droplet separation.

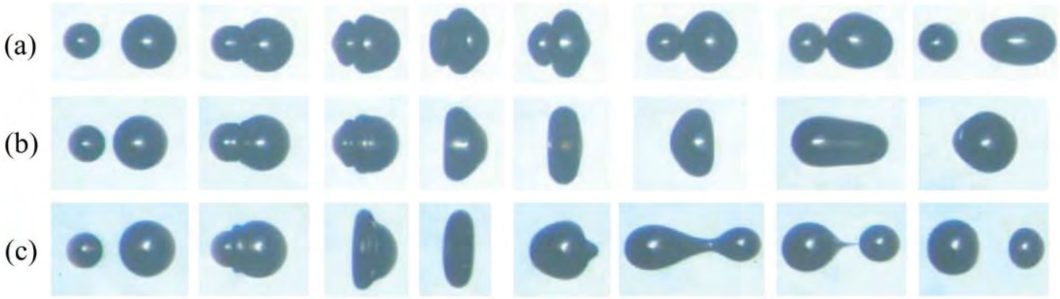

Figure 2.6 Head-on collisions between two tetradecane droplets of unequal sizes[43]. (a) $We = 7.3,\ \Delta = 1.46$, bouncing; (b) $We = 13.8,\ \Delta = 1.46$, coalescence; and (c) $We = 52.8,\ \Delta = 1.50$, reflexive separation.

In the aspect of energy budget, this observation can also be understood as that[28] the ratio of total kinetic energy to total surface energy decreases as increasing Δ and thereby reduces the possibility of occurrence of the separation. The symmetry Weber number, We^*[28], reflecting the ratio of overall kinetic energy E_{k0} over the surface energy S_0 can be defined as

$$We^* = \frac{E_{k0}}{\sigma S_0} = \frac{\Delta^3}{12(1+\Delta^3)(1+\Delta^2)} We \qquad (2.8).$$

in which We and Δ play the competitive roles that increasing We promotes droplet separation whereas increasing Δ promotes droplet coalescence.

Then the $We^* - Oh$ regime diagram is shown in Figure 2.7 by revisiting the original data from Tang *et al.*[43] to study Oh effects on head-on droplet collisions. From energy considerations, droplet bouncing occurs at small We^*, followed by droplet coalescence at intermediate We^* and droplet separation at large We^*. It is observed no bouncing regime for small Oh. The critical We^* on the boundary for both bouncing-coalescence transition and coalescence-separation transition increases with increasing Oh. Owing to the competitive roles of We and Δ included in We^*, it is observed a banded transition zone in which the same We^* would either result in separation or coalescence depending on which factor plays a dominant role between We and Δ, while beyond the transition zone shows unique collision outcomes.

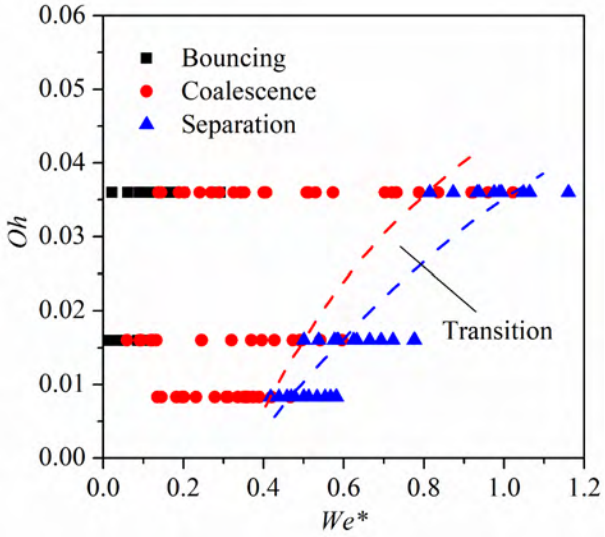

Figure 2.7 Head-on collision outcomes between two droplets of unequal sizes[43] in $We^* - Oh$ parameter space.

Furthermore, particularly in the regime of droplet coalescence, interesting phenomena of internal mushroom-like jet structure can be observed. Tang *et al.*[15] reported a non-monotonic variation of mushroom-like jet structures for the collision between two droplets of unequal sizes as increasing the impact inertia (We or We^*).

More specifically, as shown in Figure 2.8, the mushroom-like jet structure (type I) emerges at small We^*, however, such a jet structure disappears as increasing We^*, and another mushroom-like jet structure (type II) reemerges with further increasing We^* while it shows different appearances. They explained that, the type I jet at small We^* is driven by surface tension force with droplets merging at center that close to the axis; such jet structure disappears at large We^* owing to the suppressed concentration of mass momentum (strong damping) along the central line with droplets merging at a significantly flattened surface; and the type II jet at higher We^* is driven by impact inertia that strong droplet stretching in the direction of impact carries the spreading out mass of the small droplet into the large droplet to form a centrally hollow jet and thereby different from type I jet.

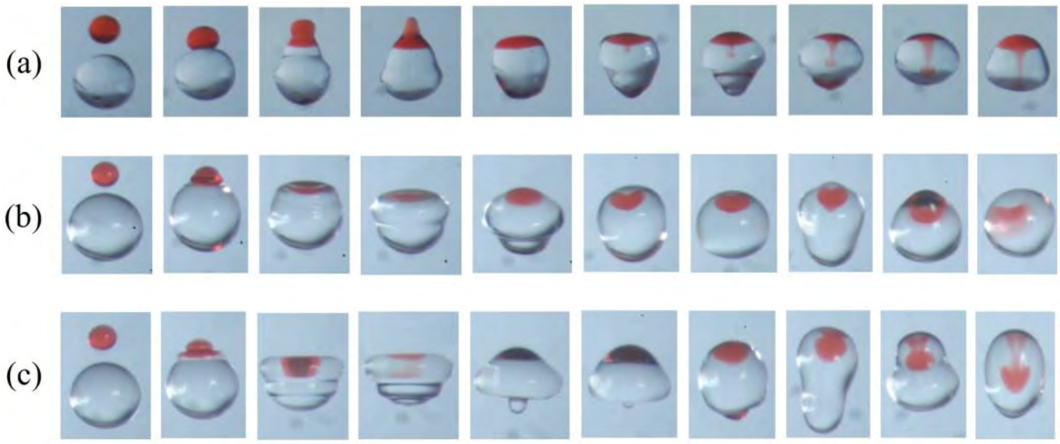

Figure 2.8 Mixing pattern during collision of water droplets for (We, Δ, We^*)[15]: (a) type I jet at (0.47,1.86,0.0075), (b) no jet at (8.59,2.61,0.15), and (c) type II jet at (17.2,2.43,0.19).

The $We^* - Oh$ parameter space in Figure 2.7 can be further developed by including the mushroom-like jet structure varying with Oh, as shown in Figure 2.9. It is observed no mushroom-like jet structure for binary collisions between tetradecane droplets ($Oh = 0.036$). It indicates that there exist a maximum Oh above which mushroom-like jet structure is absent. With decreasing Oh, the coalescence regime consists of type I jet zone for low We^*, soft merging, type II jet zone for high We^*, hard merging, and interestingly no jet zone separating two types of jet zones. The no jet zone is shrinking with decreasing Oh.

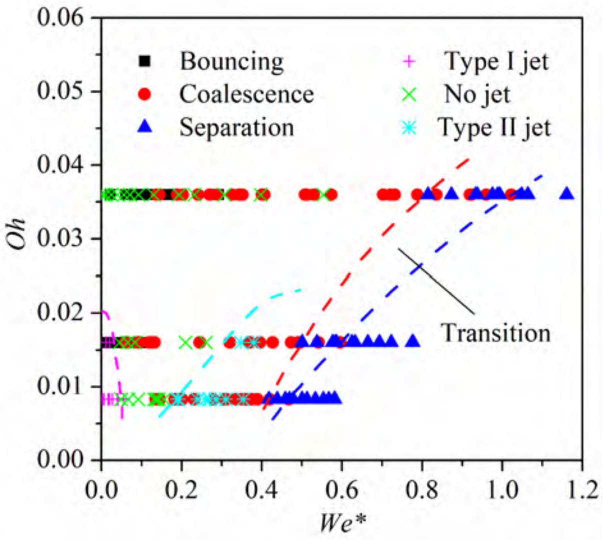

Figure 2.9 Regime nomogram for mushroom-like jet structure upon droplet coalescence in $We^* - Oh$ parameter space.

2.3.3 $\varDelta - Oh$ nomogram ($We \approx 0$ and $B = 0$)

For the above discussed surface tension driven flow that accounting for the generation of type I jet structure, a critical and idealized state is the coalescence between two initially stationary droplets with vanishing We and $B = 0$. Anilkumar *et al.*[44] experimentally studied the coalescence between two initially stationary droplets of unequal sizes in the cell filled with a specific water-glycerin solution. As shown in Figure 2.10(a) and (b), it is observed the mushroom-like jet structure upon the coalescence of droplets with small viscosity while no jet for droplets with large viscosity owing to the enhanced viscous damping. Based on the understanding of type I jet that driven by surface tension force, it is physically inferred, in fact also verified by several numerical simulations, that the mushroom-like jet structure can be promoted by a larger size disparity because the pressure difference, $4\sigma {D_S}^{-1}(1 - \mathit{\Delta}^{-1})$, close to the merge point is enlarged so that to strengthen the mass momentum of small droplet merging into the large droplet. With further increasing $\mathit{\Delta}$, as shown in Figure 2.10(c), the formed bulge during droplet merging process would be pinched off by the interface capillary wave to generate a smaller daughter droplet.

It is noted that experimental studies about the coalescence between two initially stationary droplets under gas environment is scarce in the literature. This is because it is difficult to maintain the droplet generation with such low velocity, droplet spherical shape, and most importantly the spatial possibility to collide at the same time. The alternative methods can be achieved by locating the larger droplet on the hydrophobic solid surface[45] or on the top of a nozzle outlet[46], in which the “wall effects” of surface or nozzle on the coalescence process cannot be overlooked except the capillary wave which travels down the larger bottom hemisphere has not reached the bottom wall when the physical process already ends up. Otherwise, the reflected wave would influence the coalescence process.

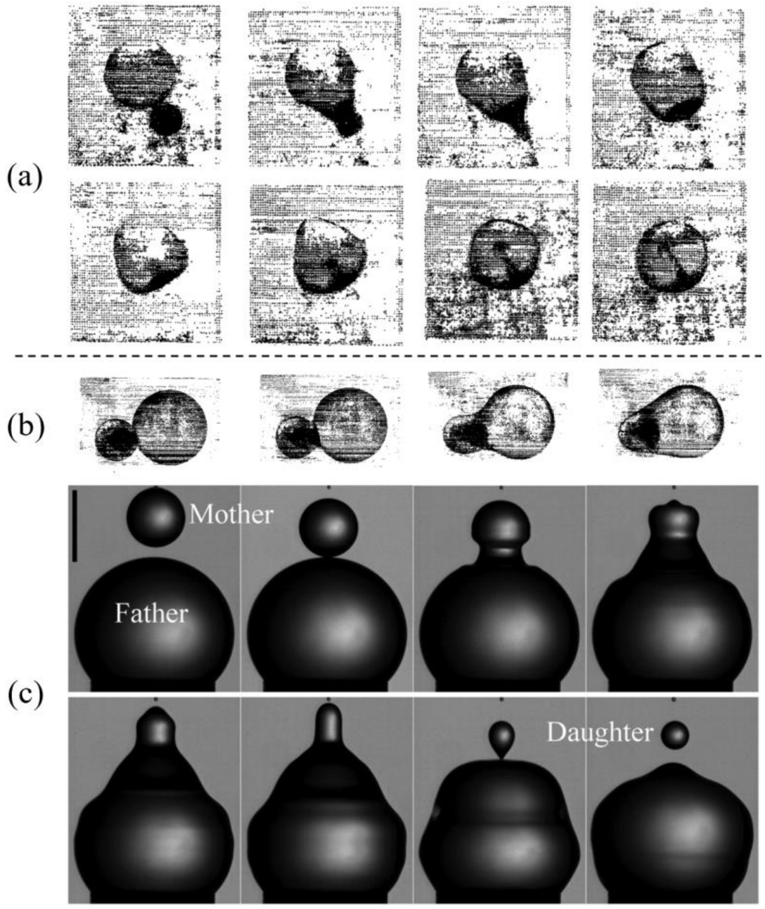

Figure 2.10 Typical sequence for the coalescence between two initially stationary droplets: (a) a mixture of silicone oil and bromobenzene with a measured viscosity of 3.3 cP[44], (b) highly viscous silicone oil with measured viscosity of 99 cP[44], and (c) a satellite pinch-off[46] for distilled water drops with $\Delta = 2.72$.

Considering the experimental difficulties for the coalescence between two initially stationary droplets, the "numerical experiments" after sufficient validations by Xia *et al.*[23] verified that the mushroom-like jet structure was suppressed by increasing the droplet viscosity while promoted by the size disparity, as the jet regime nomogram in the $\Delta - Oh$ parameter space shown in Figure 2.11. There exist a maximum value of Oh_{jet} that above which mushroom-like jet structure is absent. For the same token, Zhang *et al.*[46] experimentally determined a regime boundary with the critical Δ that above which the pinch-off occurs, as the dashed area shown in Figure 2.11. Both the critical Δ for mushroom-like jet regime and pinch-off regime increase monotonically with Oh.

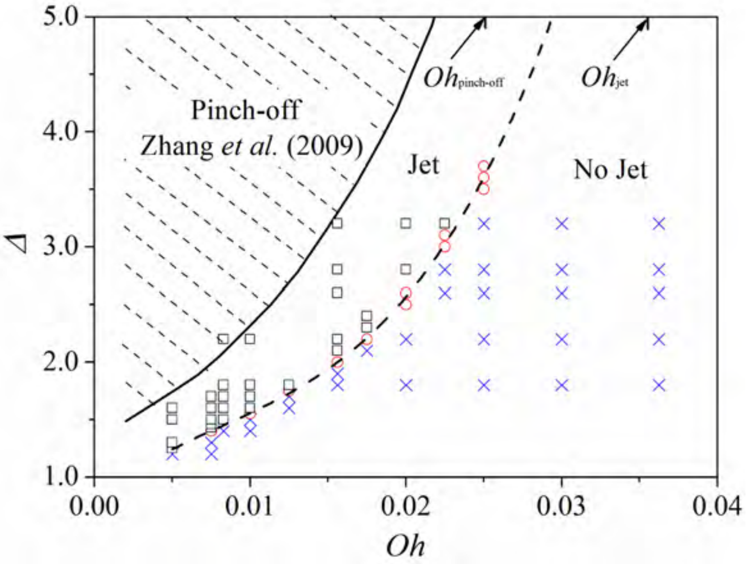

Figure 2.11 Regime nomogram of initially stationary droplet coalescence in the $\Delta - Oh$ parameter space, adapted from Xia *et al.*[23]. The mushroom-like jet structure is denoted by the square, the no-jet regime by the cross, and the transition by the circlet. The dashed area corresponds to the ranges of Δ and Oh occurring droplet pinch-off, experimentally given by Zhang *et al.*[46].

2.4 Binary collision between droplets of different fluids

The macroscopic collision outcomes[47-53] of binary collision between droplets of different fluids, such as bouncing, coalescence, and separation, are not essentially different from that of collisions between droplets of same fluid, and thereby showing the similar regime nomogram in $We-B$ parameter space[47-49] although the regime boundaries move with the liquid properties and collision parameters. However, the microscopic characteristics during the collision process between different droplets are of interests and more complex owing to the effecting parameters of droplets density, viscosity, and surface tension ratio as illustrated in Equation 1.1. Generally, the collisions between droplets of different fluids can be divided into two main types, namely the miscible droplet collision and immiscible droplet collision.

2.4.1 Miscible droplet collision

Figure 2.12 shows experimental images for the binary collision between droplets of different miscible liquids, in which the different collision outcomes compared to the binary collision between identical droplets are must originated from the density, viscosity, and surface tension differences between different miscible droplets. Chen[47] compared the collision between diesel-diesel droplets and diesel-ethanol droplets, as shown in Figure 2.12(a) and (b), and found nearly the same droplet deformation and reflexive separation. This is because diesel (take pure tetradecane as an example) and ethanol droplets have similar surface tension coefficient and density although the viscosity of diesel is approximately twice to that of ethanol.

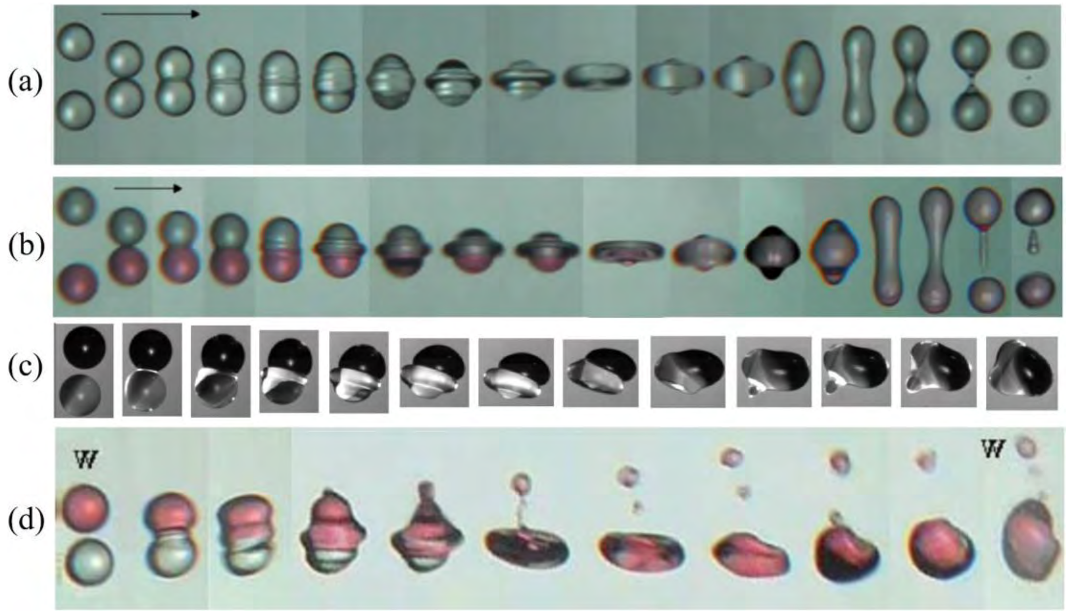

Figure 2.12 Typical sequence for the binary collision between droplets of different miscible liquids: (a) reflexive separation for diesel-diesel droplets at $We \approx 35$[47], (b) reflexive separation between diesel and ethanol (colored) droplets at $We \approx 35$ [47], (c) coalescence between a high viscous droplet (upper) and a low viscous droplet (below)[53], and (d) head-on coalescence between ethanol and water (colored) droplets at $We \approx 20$[49].

To analyze the effects of viscosity disparity, Focke *et al.*[53] experimentally studied the collision between two miscible droplets (nearly same surface tension and density) with different viscosities (2.6mPas and 60mPas), as shown in Figure 2.12(c). The results show that viscosity disparity can delay the droplet initial coalescence, and the droplet with low viscosity moves faster and slightly overlays the interface of the droplet with high viscosity. The viscosity effect affects the droplet deformation in a passive way to modulate the internal flow strength to a minor extent so that not likely to induce the transition of collision outcomes significantly.

However, it is observed substantially asymmetric deformation during the collision between water and ethanol droplets with satellite droplets generation, as shown in Figure 2.12(d). This is attributed to the Marangoni flow induced by the surface tension difference ($7.29 \times 10^{-2}\,\mathrm{N/m}$ for water and $2.23 \times 10^{-2}\,\mathrm{N/m}$ for ethanol). The Marangoni stress drives the mass of ethanol droplet diffusing along the interface of water droplet and thereby the induced ring-like (for head-on collision) Marangoni flow along the interface converges to one point on the symmetry axis to generate satellite droplets. The similar phenomenon upon the droplet coalescence with a reservoir has also been experimentally observed by Blanchette *et al.*[54] and numerically analyzed by Sun *et al.*[55]. In addition, Blanchette[56] numerically studied the Marangoni-flow-induced mixing within stationary coalescing drops and steadily flowing drops, and the results showed that surface tension variations might result in faster mixing than geometric effects.

Marangoni effects can be produced by adding surfactants into aqueous solutions. It is worthy to mention that the surfactant can be used to suppress the coalescence of the dispersed fluid phase inner the continuous fluid phase, for example the water-in-diesel emulsion. The emulsified fuel with water is benefit for the prevaporization (micro-explosion) that results in severe disruptive burning arising from dilution effects in both the gas- and liquid-phase reactions and those from the secondary atomization effects of the primary emulsified fuel spray[57, 58]. The rheology of emulsion can be influenced by various factors, such as density and viscosity of dispersed and continuum phase, size, distribution and volume fraction of the dispersed phase, and the interface rheology. Pal[59] found that the apparent viscosity of emulsion increases significantly by reducing the size of the dispersed phase. Chen *et al.*[60] experimentally studied the binary collision between water-in-diesel emulsion droplets of equal size. The results showed that the critical We of the regime boundary between coalescence and separation was larger than that for biodiesel droplet collision. This can be understood as a result of the interaction between micro dispersed water droplets which increases the apparent viscosity significantly and thereby suppresses the droplet separation. Furthermore, Pan *et al.*[61] found that the Marangoni stress induced by the surface tension gradient along the interface (diffusive and nonuniform distribution of surfactants) was opposite to the gas drainage direction among the gas film and thereby promote droplet bouncing.

2.4.2 Immiscible droplet collision

Different from the miscible droplet collision involving the interdiffusion induced by density, viscosity, and surface tension disparity, for the collision between immiscible droplets, there always exist an interface between different phases and a moving three-phase contact line. The near head-on collisions between immiscible droplets have been selected to be more representative to reflect the distinctive outcomes compared to the collision between droplets of same fluid.

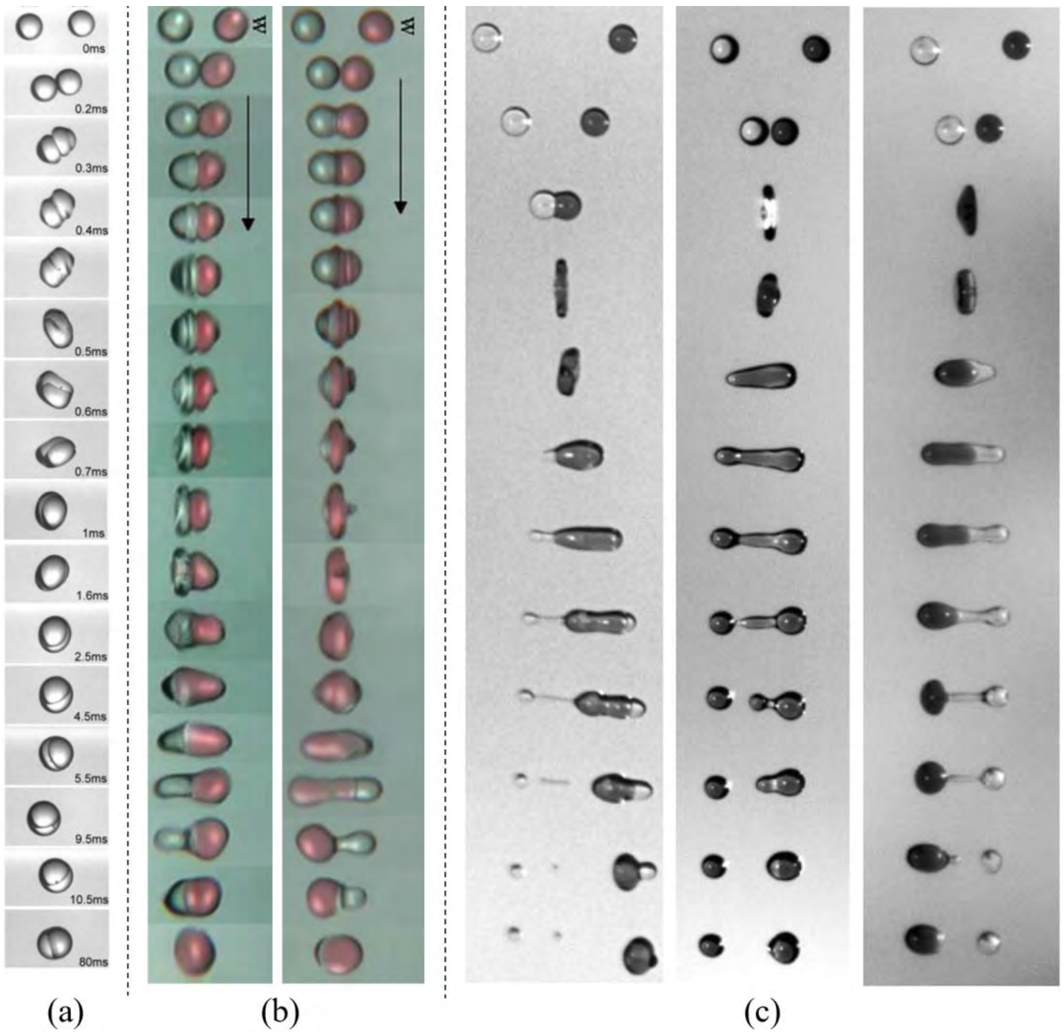

Figure 2.13 Typical sequence for the binary collision between droplets of different immiscible liquids: (a) coalescence between methanol and hexadecane droplets[16], (b) termed "overlying coalescence" between diesel (left) and water (right) droplets[48], and (c) termed "quasi-reflective separation", "single-reflex separation", and "crossing separation" between glycerol solution (left) and silicon oil (right) droplets[62].

Figure 2.13 shows experimental images of binary collision between immiscible droplets. A clear separating interface[16] can be observed between different droplets in Figure 2.13(a) owing to the immiscibility, and it is seen an entrapped bubble as illustrated by the small black dot. As shown in Figure 2.13(b), the symmetry of droplet coalescence process has been broken showing the diesel droplet (small surface tension) overlays[48] along the interface of water droplet (large surface tension). The transparent diesel droplet tends to separate either from left or from right of the merged droplets. Consequently, as shown in Figure 2.13(c), the termed “quasi-reflective separation” and “crossing separation”[62] are observed with different separated droplets. Furthermore, the termed “single-reflex separation” occurs resulting in two encapsulated drops. The detailed mechanism occurring such rich phenomena for immiscible droplets collision has not been sufficiently understood, which is probably correlated to the time scale of overlaying process and droplet deformation process.

Specifically, for the termed “overlaying coalescence” (or referred as liquid encapsulation by Planchette *et al.*[50, 63]), it is observed that the encapsulating droplet either overlays partially of the encapsulated droplet to form a “Janus droplet”[64] in Figure 2.13(a) or overlays completely to form a “liquid shell”[63] in Figure 2.13(b) and (c). Planchette *et al.*[50] studied the influence of the liquid properties, i.e. viscosity, density, surface and interfacial tensions, on the liquid encapsulation efficiency. Regardless of the dynamical encapsulation process, the equilibrium states between two immiscible droplets (complete engulfing, partial engulfing, and non-engulfing) involving the three-phase contact line are determined by spreading parameters

$$S_i = \sigma_{jk} - \left(\sigma_{ij} - \sigma_{ik}\right) \qquad (2.9).$$

If assuming, without loss of generality, the convention of designating phase-1 to be that for which $\sigma_{12} > \sigma_{23}$, it follows from Equation (2.9) that $S_1 < 0$ [52, 65]. Therefore, there are only three possible sets of values of S_i that satisfying $S_1 < 0, S_2 < 0$ and $S_3 > 0$ for complete engulfing, $S_1 < 0, S_2 < 0$ and $S_3 < 0$ for partial engulfing, and $S_1 < 0, S_2 > 0$ and $S_3 < 0$ for non-engulfing, which are also indicated by Pannacci *et al.*[66] in a regime of spreading parameters.

2.5 Binary collision between droplets of non-Newtonian fluids

Generally, most of the fluids in the engineering applications somehow reflect the non-Newtonian flow characteristics that the apparent viscosity is a function of the local shear rate. The most common shear-thinning (shear-thickening) liquids are that whose viscosity decreases (increases) with increasing local shear rate. However, it is found that the experimental studies of binary collision between non-Newtonian fluids are scarce in the literature[11]. That is probably attributed to the practical difficulties in generating spatially and temporally stable non-Newtonian droplet, which usually have very large low-shear-rate viscosity[67].

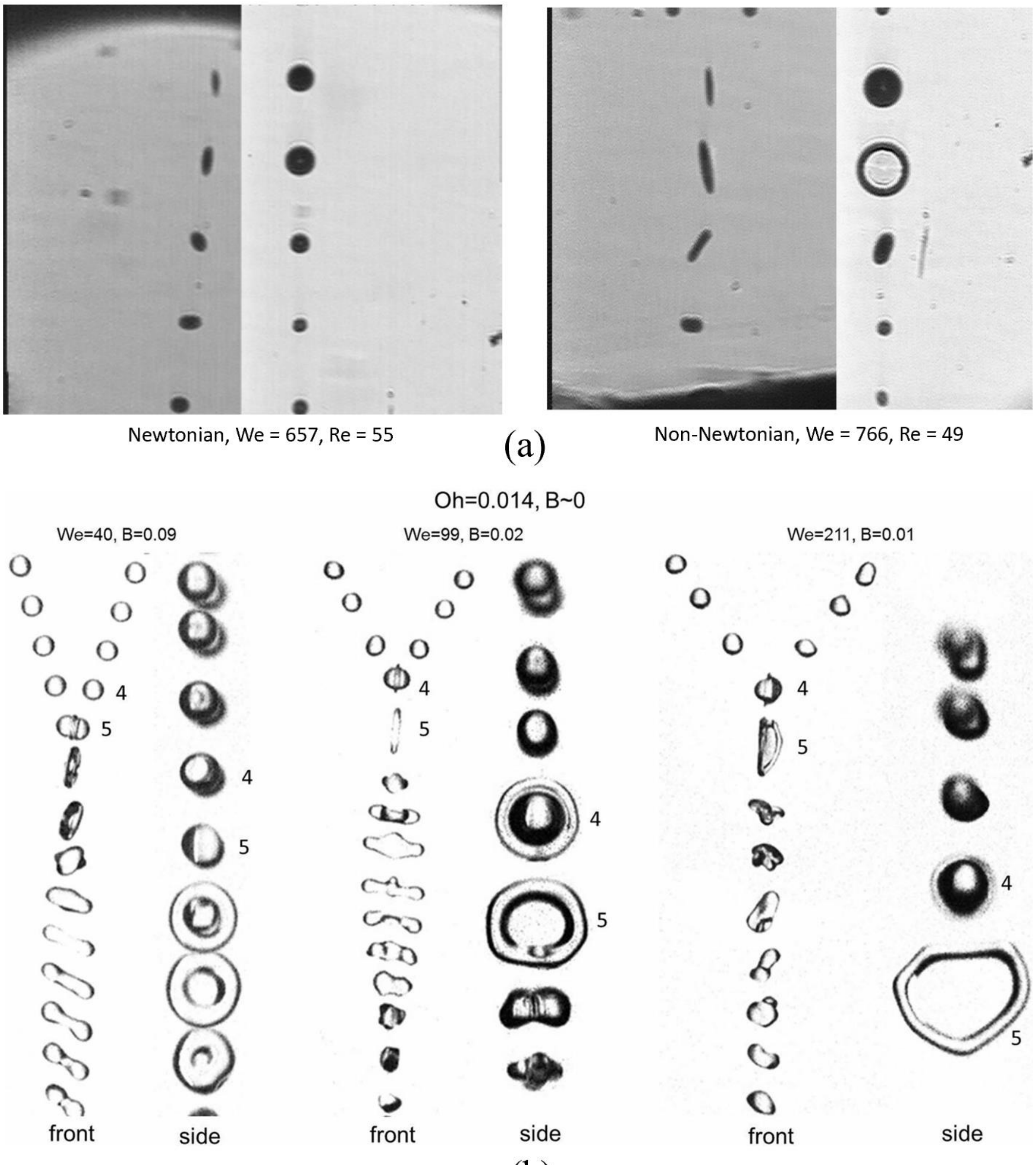

(b)

Figure 2.14 Binary collision between droplets of shear-thinning fluids: (a) CMC aqueous solution[68] and (b) xanthan[69].

Figure 2.14 shows few currently available experiments about the non-Newtonian droplet collision. Motzigemba *et al.*[68] experimentally studied the binary collision between shear-thinning droplets of water/carboxymethylcellulose (CMC) aqueous solution and found that the droplet deformation can be enhanced by the shear-thinning effects when compared to the collision between Newtonian droplets at approximate We, as shown in Figure 2.14(a). Finotello *et al.*[69] studied the binary collision between xanthan droplets and observed a thick toroidal rim during the droplet spreading process from the side view of camera, as shown in Figure 2.14(b). The diameter of this thick toroidal rim expands with increasing We, however, no separation has been observed for We up to 211 even at the averaged relatively small $Oh = 0.014$. It is seemingly that the shear-thinning effects of non-Newtonian droplets promote the droplet maximum deformation due to the reduced local viscosity but probably not favors droplet separation for some unknown mechanisms.

To analyze the microscopic flow of the binary collision between non-Newtonian droplets, several numerical studies have been conducted recently. Focke and Bothe[70] numerically showed that the collision outcomes between two identical shear-thinning droplets can be repeated by the collision between two Newtonian droplets with an equivalent effective viscosity μ_{eff} of the value between the infinity-shear viscosity μ_∞ and zero-shear viscosity μ_0. Chen and Yang[71] qualitatively described the collision outcomes transition between two shear-thinning droplets by using a Volume-of-fluid (VOF) method. Sun *et al.*[72, 73] performed comprehensive numerical studies about the collision dynamics between non-Newtonian droplets by using phase field method combined with Lattice Boltzmann (LBM) method.

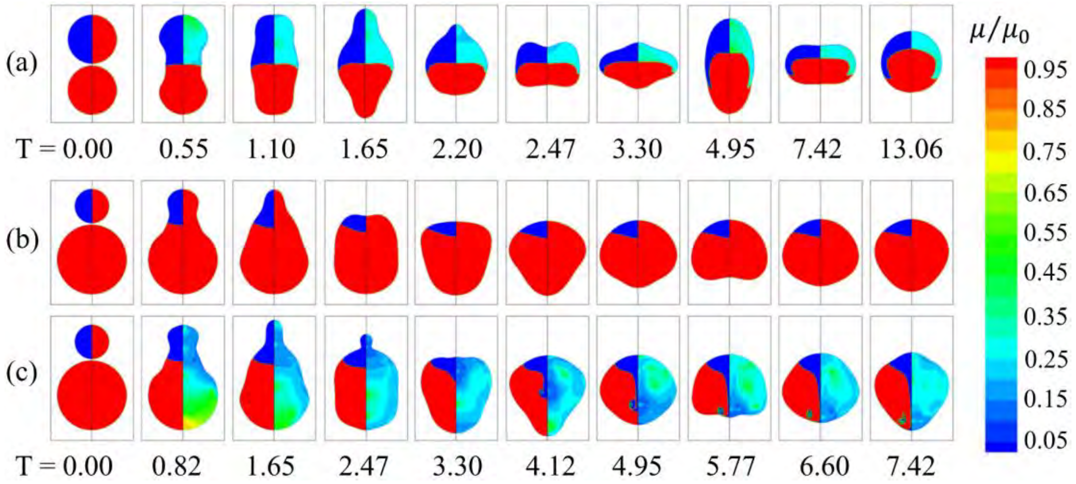

Figure 2.15 Coalescence between Newtonian droplet and non-Newtonian droplet[72]. (a) non-Newtonian droplet (upper) and Newtonian droplet (below), $\Delta = 1, Oh = 0.01$ and $Oh_\infty = 0.0015$; (b) both droplets are Newtonian, $\Delta = 2$ and $Oh = 0.05$; and (c) both droplets are non-Newtonian, $\Delta = 2, Oh = 0.05$ and $Oh_\infty = 0.002$.

More specifically, Figure 2.15(a) showed the initially stationary coalescence between one shear-thinning droplet (upper) and one Newtonian droplet (below) with the same density, zero-shear viscosity, and surface tension. It is observed that the Newtonian droplet is encapsulated by the non-Newtonian droplet owing to the locally reduced viscosity by shear-thinning effect, which is similar to the collision between one high viscous droplet and one low viscous droplet simulated by Focke *et al.*[53]. As shown in Figure 2.15(b), no mushroom-like jet structure can be observed for the collision between two Newtonian droplets with $\Delta = 2$ and $Oh = 0.05$, which is consistent with the previous results[44] that the internal jet is suppressed by large viscosity. However, it is clearly seen the mushroom-like jet structure for the collision between two shear-thinning droplets with $\Delta = 2, Oh = 0.05$ and $Oh_\infty = 0.002$, as shown in Figure 2.15(c). Considering that the initially stationary coalescence between two shear-thinning droplets is a surface tension driven flow, thus it is inferred that the internal jet can be further promoted significantly as increasing We because the local shear rate became higher under large impact inertia.

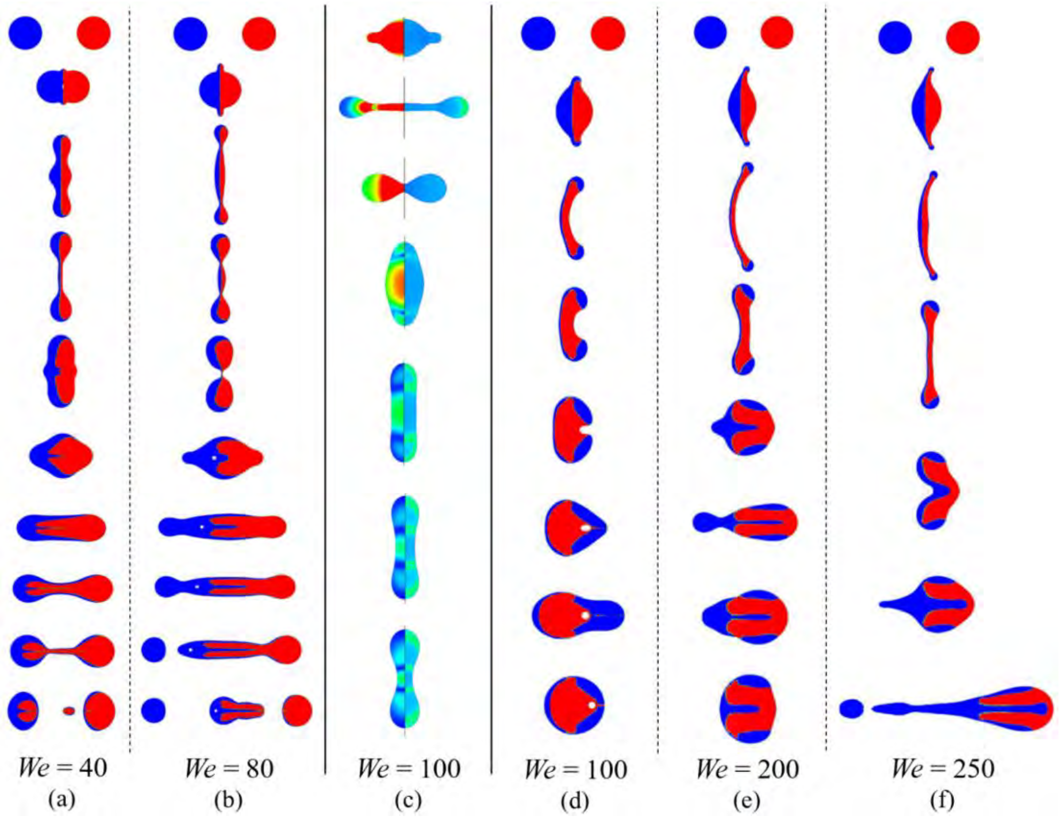

Figure 2.16 Head-on collisions of non-Newtonian droplets[73]: (a) $We = 40$ and (b) $We = 80$ for two different shear-thinning fluids; (c) $We = 100$ for two identical shear-thickening droplets; (d) $We = 100$, (e) $We = 200$, and (f) $We = 250$ for one shear-thinning droplet (left) and another shear-thickening droplet (right).

Sun *et al.*[73] further numerically studied the binary collision between different non-Newtonian droplets of equal size and non-vanishing We. Figure 2.16(a) and

2.16(b) showed the collision between two droplets with different shear-thinning effects, which indicates that the disparity of shear-thinning effects can enhance the droplet deformation at small We so that easily to separate the merged droplets into several small droplets. In addition, the separated droplets are still mixed with masses from two initial droplets, even though the separation was not desired for the internal mass intermingling. Figure 2.16(c) showed the collision between two identical shear-thickening droplets. The droplet deformation was significantly suppressed owing to the increased viscosity so that the droplet separation cannot occur even at a large We. Figure 2.16(d)-2.16(f) showed the collision between one shear-thinning droplet and one shear-thickening droplet for different We from 100 to 250. It is seen that internal mass intermingling can be promoted by shear-thinning effects and droplet separation can be suppressed by shear-thickening effects so that to allow sufficient mixing, which is a promising concept for the fluid-phase fuel-oxidizer hypergolic ignition system in the rocket engine.

2.6 Binary collision between other (charged or reactive) droplets

The rich phenomena of binary droplet collision are of increasingly interests by considering more factors, for example, the collision between charged droplets under electrical field or the collision between reactive droplets involving phase change and chemical reactions.

Ristenpart *et al.*[74] reported that the oppositely charged droplets tend to bounce off at high electrical field strengths that are supposed to coalescence at low field strengths. The high-resolution images focusing on the transient formation of a meniscus bridge between the bouncing droplets show that this temporary bridge is unstable[75] with respect to capillary pressure when it forms in an electric field exceeding a critical strength. The external electrical force influences coalescence, separation, and satellites ejection between liquid metal droplets[76]. The effects of an external electric field on droplet coalescence can be found in a review paper by Kavehpour[77].

Generally, the combustion of impinging fuel sprays[2, 3, 78] in the engines experiences several stages such as sprays breakup involving droplet collision, droplet heating, vaporization, and combustion in the gas phase. In terms of the micro-explosion phenomena induced by internal superheating that benefits to the prevaporization and second atomization, Wang *et al.*[16, 79] reported that the micro-explosion was only observed for the collision-generated droplets and believed to be initiated by the air bubbles entrapment during the collision.

A representative binary droplet collision and subsequent ignition process between two reactive droplets, for example the hypergolic ignition between N, N, N’, N’−tetramethylethylenediamine and white fuming nitric acid droplets, has been experimentally identified by Zhang *et al.*[80], as the shadowgraph images shown in Figure 2.17. The entire process can be visually divided into five stages: Stage I (0 ms – about 4.0 ms): droplet coalescence and deformation; Stage II (about 4.0 ms – about 20.0 ms): droplet heating and vaporization; Stage III (about 20.0 ms – about 30.0 ms): rapid vaporization and reactions; Stage IV (about 30.0 ms – about 31.0 ms): ignition in gas phase; and Stage V (after about 31.0 ms): flame propagation and combustion. Zhang *et al.*[80] found the seemingly counterintuitive results that, in a certain (relying on Δ) range of We, the ignition delay times increase with We. This result can be speculatively attributed to the recently identified phenomena in droplet coalescence and internal mixing[15] that the jet-like mixing patterns emerge at relatively small and large We but disappear at intermediate We. It indicates that the ignition process upon the collision between two hypergolic ignition droplets is probably dominated by the internal mass entanglement in the preliminary collision stage.

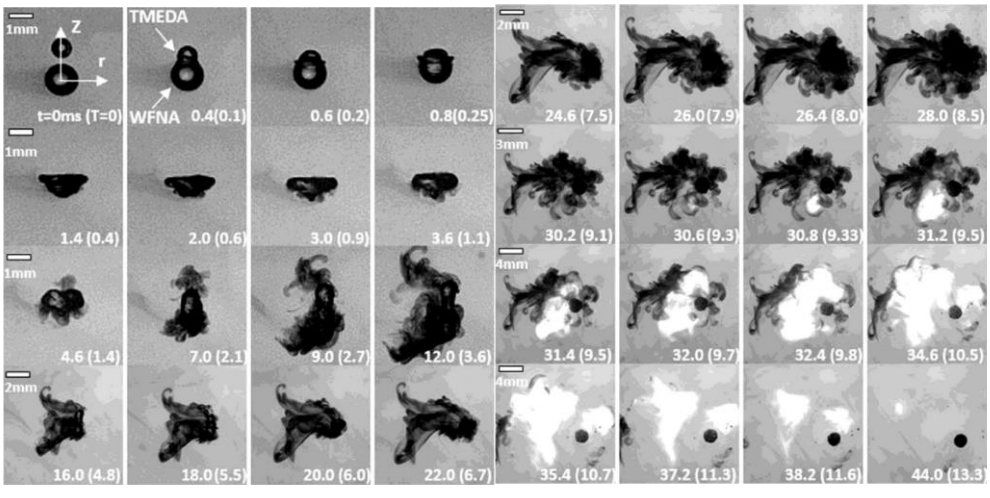

Figure 2.17 Shadowgraph images of the hypergolic ignition at selected times[80].

2.7 Theoretical and numerical predictions on binary droplet collision

We believe that a qualitatively understanding of the binary droplet collision has been obtained from the above discussions about the experimental phenomena. However, more general conclusions about the dynamics of collision process, such as coalescence, bouncing, separation, and splashing, and accurate predictions on the collision outcomes are anticipated. Considering the complexity of binary droplet collision with so many controlling parameters, the theoretical analysis can be initiated from the simplest model of the head-on collision between identical droplets, and then extended to more general case of off-center collision between droplets of unequal sizes.

2.7.1 Coalescence – bouncing transition with minor droplet deformation

As Qian *et al.*[25] reported that high pressure environment, equivalent to high gas-fluid density ratio according to the equation of state of gas, favors bouncing after collisions between two identical droplets, their further study indicated that it is easily to occur droplet bouncing under 7.5 atm helium than 1 atm nitrogen although the gas density is almost the same. This is because the viscosity of 7.5 atm helium is 11% larger than that of 1 atm nitrogen, which might account for the easily droplet bouncing.

Then, Bach *et al.*[81] proposed that the mean free path of the ambient gas

$$\lambda = \frac{\mu}{\rho}\sqrt{\frac{\pi m}{2k_B T}} \tag{2.10}$$

plays significant roles on the gas film draniage. Thus, the rarefied gas effect among the gas film region has to be considered to accuratly describe the transition between coalescence and boucning. The resutls showed that the critical Knudsen number of the transition state, $Kn = \lambda/a$ (a is droplet radius), was independent of We, but increased with the increase of viscosity and decreased as increasing the ambient gas pressure. Binary droplets after the collision tend to bounce off with small gas mean free path, i.e. the smaller viscosity or larger environemtn pressure. That explains why the 7.5 atm helium favors dropelt bouncing than 1 atm Nitrogen because the mean free path of the former is 2.5 times smaller than that of the latter. However, this theory was only valid for the cases with $We \ll 1$ but not for dropelt collision with large deformation.

2.7.2 Coalescence – bouncing – coalescence transition

Zhang and Law[17] proposed a model, combining the lubrication layer theory, the pressure correction by the rarefied gas effects among the gas film, the Van der Waals attractive force, and the viscous dissipation evaluation, to predict the nonmonotonic coalescence-bouncing-coalescence transition as increasing We for the head-on droplet collision.

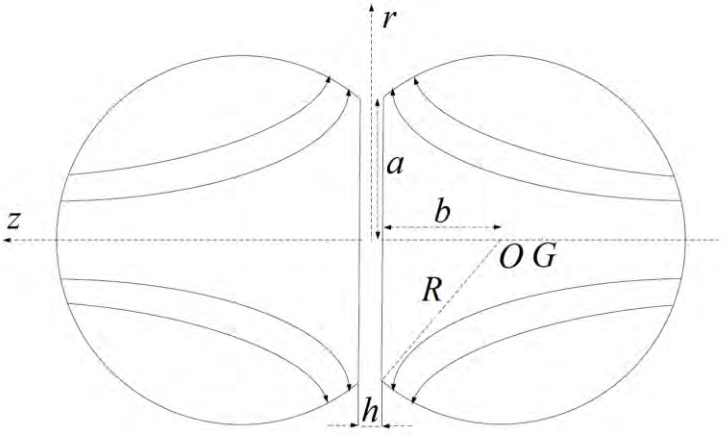

Figure 2.18 Schematic of the analyzed droplet configuration[17]. The three time-dependent variables describing the droplet geometry and dynamics are the radius of the flattened interface $a(t)$, the perpendicular distance from the center of the spherical surface to the flattened interface $b(t)$, and the distance between the impacting interface $h(t)$.

Topological changes of the droplet free interface at large We are complicated than that at small We, thus the small spherical perturbation analysis cannot be available any more. The realistic droplet deformation can be described by a truncated sphere with a flattened cap, as shown in Figure 2.18. The problem can be simplified to focus on only one droplet because of the symmetry between identical droplets. Three independent time-dependent variables describing the geometrical droplet deformation and dynamics are, the radius of the flattened interface $a(t)$, the perpendicular distance from the center of the spherical surface to the flattened interface $b(t)$, and the distance between the impacting interfaces $h(t)$. The droplet radius $R(t)$ can be expressed using the above three variables as $R^2(t) = a^2(t) + b^2(t)$.

The correlations between these variables can be established based on the mass, momentum, and energy conservation laws. The mass conservation $dM/dt = 0$ has

$$\frac{d}{dt}(2R^3 + 3R^2b - b^3) = 0 \tag{2.11}$$

The deceleration by decreasing b or acceleration by increasing b of the droplet mass center $G = b + 3(R-b)^2/\,[4(2R-b)]$ can be described as

$$\frac{d^2}{dt^2}\left(G + \frac{h}{2}\right) = \int_0^a p_g\left(r, z = \frac{h}{2}; t\right) 2\pi r dr \tag{2.12}$$

in which the right-hand side of equation (2.12) is the resistance force $F(t)$ on the flattened interface by the gas film pressure p_g.

The energy conservation has

$$\frac{d}{dt}(E + \Sigma) = \dot{W} - \phi \tag{2.13}$$

where $E = M(G + h/2)^2/2$ the translation energy of the droplet mass center, $\varSigma = \sigma\pi(3R^2 + 2Rb - b^2)$ the surface energy, $\dot{W} = F\dot{h}/2$ the power of gas film resistance force, and ϕ the total viscous dissipation rate of the inner flow. Once the flows inner gas film region and droplet are known, the gas film resistance F and viscous dissipation rate ϕ can be calculated, and the ordinary differential equations describing the droplet deformation and coalescence can be solved accordingly.

As discussed before, the minimum gas film thickness h can reach 10 nanometers whereas the mean free path λ of atmosphere air in 1 atm is about 100 nanometers, resulting in the Knudsen number $Kn = \lambda/h$ as large as 10. Thus, the rarefied gas effect among the gas film must be considered to accurately estimate the pressure distribution, otherwise the exceeding resistance force induced by the overestimated pressure prevents the droplet interfaces from approaching sufficiently to the Van der Waals scale as small as $O(10^2)$ nm, and thereby always leads to droplet bouncing.

In addition, the gas film thickness is assumed to be far less than the radius of the flattened interface because of the sufficiently large droplet deformation, i.e. $h \ll a$, thus the local gas film flow can be approximated as the rarified gas flow between two flattened interfaces (the approaching velocity and the radius expansion rate of the flattened interface are dh/dt and $\kappa = (da/dt)/a$, respectively). Zhang and Law[17] derived a solution that valid for a wide range of Kn by solving Boltzmann equation with Bhatnagar-Gross-Krook (BGK) model as

$$p_g' = \frac{3\mu_g}{h^3}(r^2 - a^2)\left(\frac{dh}{dt} + 2\kappa h\right)/f(Kn) \tag{2.14}$$

where

$$f(Kn) = \begin{cases} 1 + 6.0966Kn + 0.9650Kn^2 + 0.6967Kn^3 \ (Kn < 1) \\ 8.7583Kn^{1.1551} \ (Kn \geq 1) \end{cases} \tag{2.15}$$

It is noted that equation (2.14) can be degenerated to continuous lubrication flow if the rarefied gas effects are not considered.

It is worthy to mention that the Van der Waals force accounting for the droplet coalescence mechanism can be included by adding another amount of negative pressure[13] on the droplet interface as

$$p_{vdW} = -\frac{A_H}{6\pi h^3} \tag{2.16}$$

where the Hamaker constant $A_H = O(10^{-21} - 10^{-18})\ \mathrm{J}$ is very small. The negative pressure increases cubically with decreasing the gas film thickness h and finally becomes significantly effective to rupture the interface only when the gas film thickness is sufficiently small. Consequently, the estimated pressure among the gas film region is a sum of the corrected pressure by rarified gas effects and the Van der Waals negative pressure: $p_g = p_g' + p_{vdW}$.

We can still yield some useful understandings although the analytical solutions are difficult to describe the unsteady droplet deformation and complicated inner flow in the realistic situations. Zhang and Law[17] simplified the droplet deformation as a rapidly expanding or contracting disk (analogous to Von Karman rotated disk flow), in which the viscous effects are mainly restricted into a thin layer close to the flattened interface $(\eta \sim \sqrt{\nu_l/\kappa})$. The simplified velocity field is given as

$$u = \frac{1}{2}\nu_l \eta^2 r e^{-\eta z}, v = -\nu_l \eta (1 - e^{-\eta z}) \tag{2.17}$$

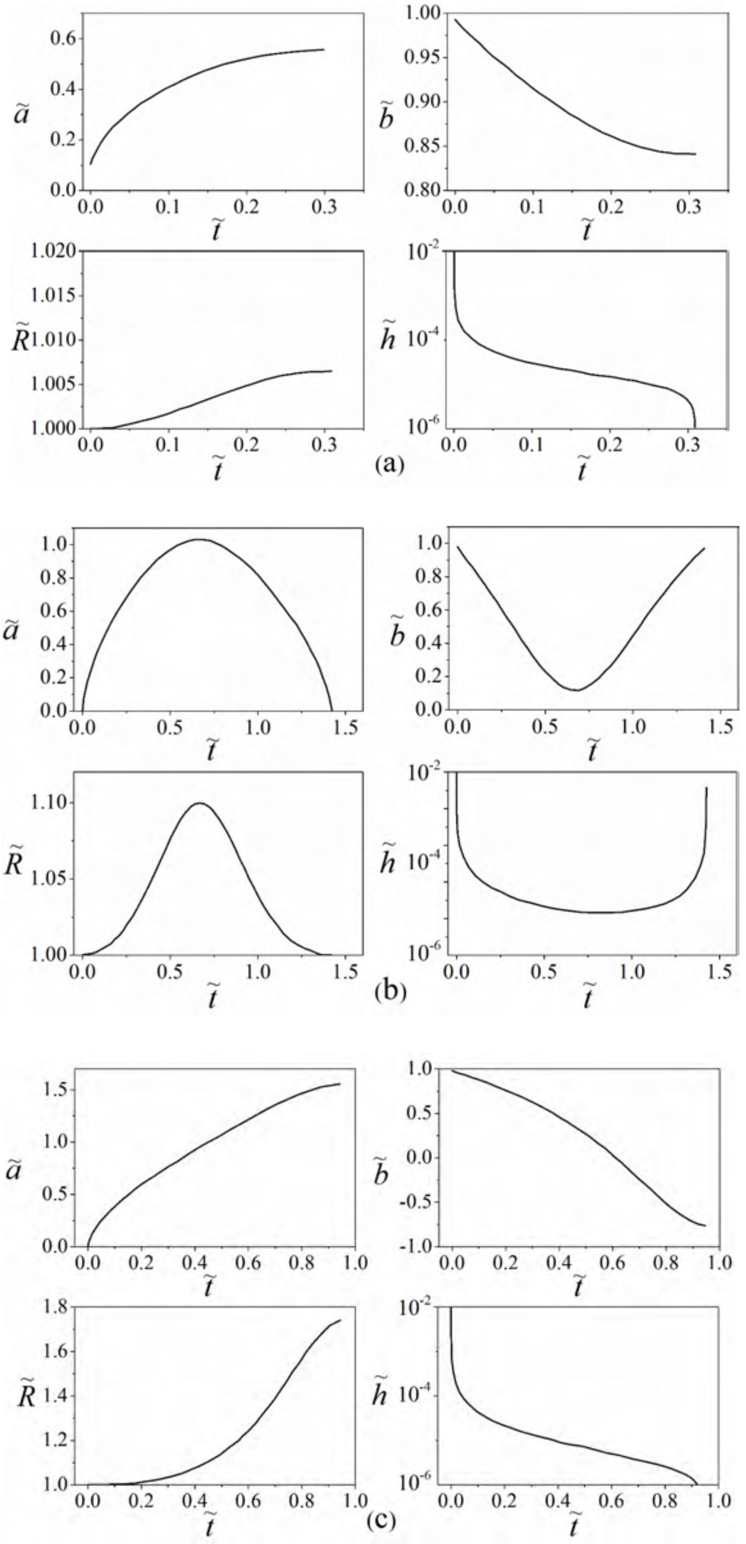

Figure 2.19 Evolution of the time-dependent variable $\tilde{a}$, $\tilde{b}$, $\tilde{R}$, and $\tilde{h}$ describing the tetradecane droplet[17] (a) coalescence (I) at $We = 0.8$, (b) bouncing (II) at $We = 6.1$, and (c) coalescence (III) at $We = 34.1$.

It shows the boundary-layer-like characteristics of the internal-flow-induced viscous dissipation during the radial expansion process. Then the total viscous dissipation rate ϕ can be calculated.

The model has been validated to successfully predict the non-monotonic coalescence-bouncing-coalescence transition with large droplet deformation, as the examples of binary collision between tetradecane droplets shown in Figure 2.19. It is worthy to mention that the model prediction fails if ignoring no matter what viscous dissipation, rarefied gas effects, or Van der Waals force. Furthermore, the Knudsen number Kn, the Hamaker constant $\tilde{A}_H$, and the capillary number $Ca = \mu_g V_0/\sigma$ relevant to the initial values of the dynamics system, are indispensable to describe the droplet collision in the gaseous environment.

2.7.3 Coalescence – separation transition

Based on the negligible inviscid flow for the binary collision between water droplets, Ashgriz and Poo[14] proposed the capillary wave instability mechanism for the criteria of droplet reflexive separation. As pointed by Stone and Leal[82], the droplet filament should be stretched sufficiently to develop instable capillary waves if the capillary instability accounts for the mechanism of droplet separation, however, this cannot be observed in the previous experiments. Later, Jiang *et al.*[24] focused on the binary collision between alkane droplets (with viscosity larger than water) and showed that the critical We of the transition from coalescence to reflexive separation for head-on collisions increases as increasing the viscosity.

Qian and Law[25] proposed a theoretical model (based on energy conservations between kinetic energy, surface energy, and viscous dissipation) to predict the critical transition between coalescence and reflexive separation for the head-on collision between identical droplets. It is found that the critical Weber number We_c is linearly dependent on the Ohnesorge number $Z = 16\,\mu/(\rho R\sigma)^{1/2}$ as

$$We_c = \beta Z + \gamma \tag{2.18}$$

It is a general conclusion for many different fluids (Oh), as number points shown in Figure 2.20, where β is a geometric parameter and independent of the fluid properties, while γ is the additional surface energy induced by the droplet deformation. This can be understood as that, the initial total kinetic energy of droplets occurring separation can be divided into two parts, one is for overcoming viscous dissipation and interface oscillation, and another is for compensating the addition of surface energy owing to droplet deformation. Then, Tang *et al.*[43] extended the model to binary collision between droplets of unequal sizes and found the similar expression as Qian and Law[25], in which the parameters $\beta(\Delta)$ and $\gamma(\Delta)$ are size ratio dependent. The parameters in the model were determined from fitting the experimental data of tetradecane droplets, and they were also satisfactorily valid for water and decane droplets.

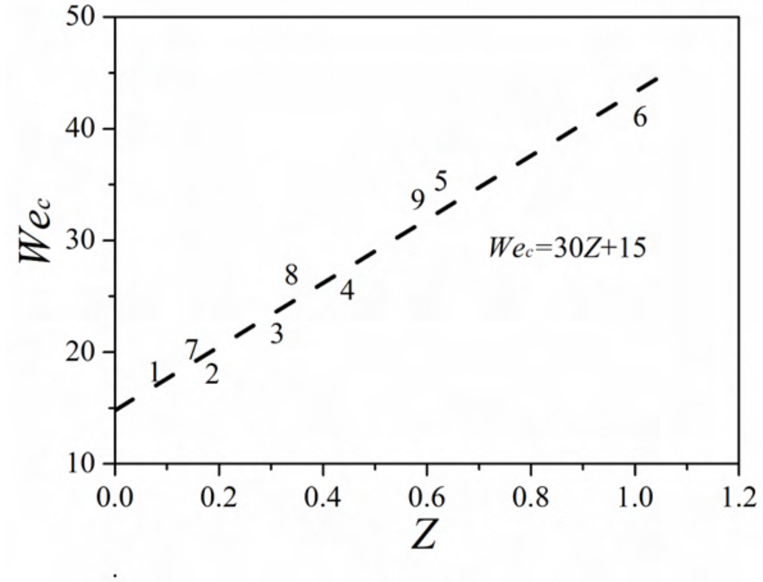

Figure 2.20 Critical Weber number versus Ohnesorge number for the regime boundary between coalescence (III) and separation (IV) in air environment[25]. Number 1 to 8 denote different cases of droplet collision of different fluids under a certain ambient gas environment.

To further study the deviations between the model prediction and experiments, Tang *et al.*[43] performed a simple sensitivity analysis on the viscous dissipation and residual surface energy at different collision stages. It indicated that the viscous dissipation in the second stage (i.e. contracting stage from maximum droplet deformation to firstly recover to the approximately spherical shape driven by surface tension) contributed to the majority of the overall viscous dissipation and thereby suppressed the droplet reflexive separation. The critical We_c increases with increasing Δ owing to the enhanced viscous dissipation by internal flow.

Furthermore, for more general situation of off-center droplet collision, Ashgriz and Poo[14], Jiang *et al.*[24], and Rabe *et al.*[28] have also conducted some preliminary theoretical analysis on the prediction of the regime boundary between coalescence and stretching separation.

2.8 Summary

This literature review summarizes the previous studies on the binary droplet collision influenced by various parameters in accordance with the non-dimensional parameter analysis. Various distinctive collision outcomes have been identified and compared for each controlling parameter. Experimental, theoretical, and numerical methods are all indispensable to study binary droplet collision. The experimental method is a most direct way to study binary droplet collision but still challenging on the visualization and analysis on the microscopic flow filed that merits further development. The theoretical analysis can obtain some general conclusion but is hardly to predict the entire complicated and unsteady collision process involving multi-scale and multi-physics characteristics. Similarly, the numerical simulation also cannot predict the droplet collision although they are useful to analyze the microscopic flow filed once has been validated by experimental observations sufficiently.

Compared with the extensively studies on the effects of size ratio, Weber number, Ohnesorge number, and impact parameter on the binary droplet collision, the binary collision between droplets of different fluids, the non-Newtonian fluids effects, the pressure effects, and more practically the real sprays involving large amount of binary droplet collision have been paid increasing attentions in the recent years.

3 Numerical methodology

3.1 Background

Extensive advances have been achieved in the numerical simulation of droplet collision, by employing various interface tracking methods such as the Front Tracking (FT) method, the Volume-of-Fluid (VOF) method, the Level-set method[83, 84], the Phase Field method combined with Lattice Boltzmann method (LBM), the Smooth Particle Hydrodynamics (SPH) method[85, 86], the diffuse-interface method[87, 88], and other particle methods[89].

The most commonly used interface tracking methods based on the continuum flow can be divided into two types: explicit front-tracking (Lagrangian method) and implicit volume-tracking (Eulerian method). For the former, for example the FT method, the flow field is solved by Euler method while the freely convective interface is tracked by the Lagrangian method with a set of sequenced points. For the latter, such as VOF, Level-set, and Phase Field method, the free interface is presented by a defined volume fraction function.

FT method is perfectly in simulating binary droplet bouncing[41, 90] because two interfaces independently represented by two sets of sequenced points that cannot contact and without topological changes. However, to simulate droplet coalescence, it requires to merge the interface manually at predefined merging position and time. The

Lagrangian interface markers must be added or deleted according to the interface topological changes, which has more algorithm complexities than Eulerian methods to treat complex droplet deformation and remains challenging for the front-tracking family.

In terms of VOF and Level-set methods, the droplet collision outcomes are strongly influenced by the mesh resolution near the interface. Consequently, a coarse mesh would induce “premature” coalescence of the droplets that are supposed to bounce off. Then, the adaptive mesh refinement technics have been applied to increase the mesh resolution especially for the interface region so that to delay the numerical droplet coalescence. Chen and Yang[91] developed a thickness-based adaptive mesh refinement method, and they could simulate droplet bouncing with a relatively smaller number of meshes because only the interface close to the interaction region was refined. However, the time step must be significantly decreased for numerical stability, thereby restricting the computational efficiency. Coyajee and Boersma[92] proposed a modified VOF approach which applies different marker functions to describe separate interfaces so as to avoid interface coalescence on a coarse mesh. Kwakkel *et al.*[93] applied this approach to establish a droplet coalescence model by manually merging two interfaces at the experimentally verified gas film drainage time. This modified VOF method with multiple marker functions is partly similar to the front-tracking method.

Different from above mesh-dependent interface tracking methods of VOF and Level-set, the Phase Field method solving Cahn-Hilliard advection-diffusion equation can simulate droplet collision at uniform meshes, where equilibrium in a heterogeneous system is obtained by minimizing the chemical potential through a parameter of mobility. It can delay the interface merging[72, 73, 94, 95] by choosing a reasonable parameter of mobility, which is more efficient than VOF and Level-set to simulate droplet bouncing at relative coarse mesh.

However, it is noted that all the physically unrealistic interface merging mechanisms introduced to the above methods are unable to predict the binary droplet collision because of the absence of the connection between the macroscopic mechanics based on the continuum description and the microscopic mechanics implementing intermolecular forces[13] responsible for interface merging. In recent year, several attempts have been devoted for the prediction of droplet coalescence and bouncing from the first principle by implementing Zhang and Law's[17] theory as a sub-grid model. Li[96] reported preliminary success in numerically predicting droplet coalescence by using finite element method. An important comment on the Supplementary Materials of[96] indicated that the interpolation of viscosity in VOF methods grossly over-estimated the viscosity in the lubrication layer and hence the lubrication forces. Consequently, VOF methods were unable to predict the transition between coalescence and bouncing with minor droplet deformation because the thickness of the gas film cannot reach the length scale that Van der Walls force become effective. Musehane *et al.*[97] reported to successfully predict the droplet coalescence by coupling the multiple marker method[92] with a thin film drainage model based on VOF method. Rajkotwala *et al.*[98] improved and extended Local Front Reconstruction Method (LFRM) with a film drainage model based on the front-tacking method. Liu and Bohe[99] have also made some attempts on this topic. Overall, these numerical methods of predicting droplet coalescence with sub-grid models are still computationally expensive because it requires to resolve the interface mesh to the scale of $O(10)$ nm, especially in 3D simulations.

3.2 Volume-of-Fluid (VOF) method

The VOF method is noted for its mass conservation but it is difficult to evaluate the interface curvature and normal vectors merely from VOF functions. While for Level-set method, the interface normal vector and curvature can be easily obtained by the level set function but it suffers from a disadvantage of mass loss although this can be improved by using “reinitialization” technique[100]. The level set function satisfies conservative law but does not imply the mass of each fluid is also conserved.

To take both advantages of each approach, a coupled Level-set Volume-of-Fluid method (CLSVOF)[101] was developed. However, CLSVOF method introduces two different representations of the same interface (i.e. Level-set function is for the evaluation of interface curvature and normal vector and VOF function is used to ensure mass conservation[92]), which inevitably results in numerical errors for the interface positions. That is because the Level-set function is reinitialized[92, 101] and constructed from the volume fraction at each timestep as a distance function to piecewise linear interface segments. The detailed "coupled" advection algorithm is explained in[101]. Cummins *et al.*[102] argued that the errors owing to the reinitialization of Level-set function can result in the inaccurate curvature estimation that do not converge with mesh resolution.

In the present work, an alternative VOF method combining continuum surface force (CSF) with height function curvature estimation were applied. VOF/CSF method is different from CLSVOF method because the interface is only represented by the VOF function and existing no "coupling" between VOF function and height function. The height function and curvature[102, 103] can be accurately calculated from the conservative VOF function without any reinitializations.

The present VOF/CSF method has been implemented in an open source code, Gerris[18, 19], featuring the 2D/3D quadtree/octree adaptive mesh refinement, the geometrical VOF interface reconstruction, and continuum surface force (CSF) with height function curvature estimation. It solves the unsteady, incompressible, and variable-density Navier-Stokes equation with surface tension by using the classic fractional-step projection method. The temporal discretization is second-order and the Poisson equations is solved by a multi-level solver through iterative methods (Jacobi, Gauss–Seidel) using a relaxation operator. The resulting Crank–Nicholson discretization of the viscous terms is formally second-order accurate and unconditionally stable. Gerris has been demonstrated to be competent for solving a wide range of multiphase problems[15, 20, 21, 23, 91, 104-106].

3.3 Strategy of adaptive mesh refinement

For VOF simulations in Gerris, the numerical gas-liquid interface is identified by so-called “mixed cells” with $0 < c < 1$. Owing to the interface reconstruction, the spatial thickness of those “mixed cells” denoting the interface is only of one mesh size. Thus, to approach the infinite thin gas-fluid interface in real situations, the numerical interface cells must be as small as possible. A reasonable choice of adaptive mesh refinement method can reduce the total number of cells and increase the computational efficiency substantially.

To resolve the droplet interface and also the internal flow, the computational domain can be divided into three physical zones, as schematically shown in Figure 3.2, namely the gas, the interior of droplet, and the interface zone. Each zone has its own mesh refinement level denoted by N, which corresponds to a minimum mesh size of $O(2^{-N})$. Accordingly, we can use (N_1, N_2, N_3) to prescribe the refinement levels in all three zones.

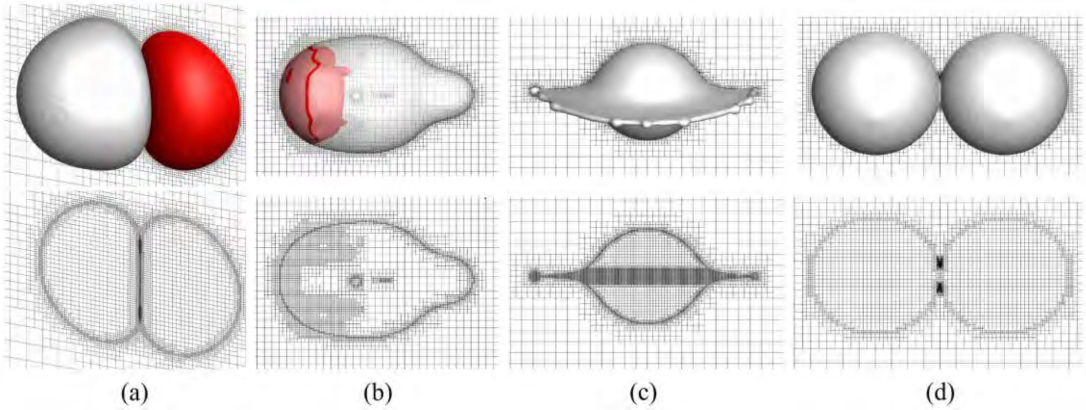

Figure 3.1 Schematic adaptive mesh refinement in 3D numerical simulation: (a) topological refinement, (b) variable-based (color function or vorticity) refinement, (c) thickness-based (film thickness) refinement, and (d) curvature-based refinement.

Based on three different physical zones, the domain can be further locally refined for different collision outcomes because the local information of flow field might be significant. As shown in Figure 3.1, four mesh refinement methods oriented to different physical problems are introduced. Figure 3.1(a) shows the topological refinement to locally refine the interface zone where the interface fragments are separated by less than two cells, which can be used to delay interface merging[91]; Figure 3.1(b) shows the variable-based refinement, for example the gradient of color function or vorticity, which can be used to study the inner mass interminglement or the vorticity dynamics[23], respectively; Figure 3.1(c) shows the thickness-based refinement, which can be used to study the droplet spreading and film dynamics for the binary droplet collision at sufficient large Weber number; and Figure 3.1(d) shows the curvature-based refinement, which can be used to study the dynamics of droplet coalescence[107] at initially short period.

3.4 Numerical specifications and preliminary validations

To solve both gas and liquid phases, it introduces a volume fraction c, where $c = 1$ for liquid phase, $c = 0$ for the gas phase, and $0 < c < 1$ for the gas-liquid interface. Then the global density and viscosity can be constructed by c as $\rho(c) = c\rho_l + (1-c)\rho_g$ and $\mu(c) = c\mu_l + (1-c)\mu_g$, in which the subscripts l and g denote the liquid and gas phases, respectively. The volume fraction c satisfies the advection equation

$$\partial c/\partial t + \nabla \cdot (c\boldsymbol{u}) = 0 \qquad (3.1).$$

The continuity and incompressible Navier-Stokes equations

$$\nabla \cdot \boldsymbol{u} = 0, \qquad (3.2)$$

$$\rho(\partial \boldsymbol{u}/\partial t + \boldsymbol{u} \cdot \nabla \boldsymbol{u}) = -\nabla p + \nabla \cdot (2\mu \boldsymbol{D}) + \sigma\kappa\boldsymbol{n}\delta_s, \qquad (3.3)$$

are solved by using the classic fractional-step projection method, where $\boldsymbol{u}$ is the velocity vector, ρ the density, p the pressure, μ the dynamic viscosity, and $\boldsymbol{D}$ the deformation tensor defined as $D_{ij} = (\partial_j u_i + \partial_i u_j)/2$. In the surface tension term

$\sigma\kappa\boldsymbol{n}\delta_s$, δ_s is a Dirac delta function, σ the surface tension coefficient, κ the local curvature, and the unit vector $\boldsymbol{n}$ normal to the local interface.

Figure 3.2 shows the axisymmetric coordinate for head-on droplet collisions with non-vanishing Weber number. The domain is $6D_S$ in length and $3D_S$ in width. The bottom boundary is the symmetric axis, which is specified as axisymmetric boundary condition while the others are specified as the free outflow boundary conditions. Two droplets collide in the axial z-direction with their velocity components $U_S = -\varDelta^3 U/(1+\varDelta^3)$ and $U_L = U/(1+\varDelta^3)$ in the mass center coordinate so that the relative velocity is U and the momentum of the collision system remains zero. The oscillation time is $t_{\text{osc}} = \sqrt{\rho_S D_S^3/\sigma_S}$, by which the non-dimensional time can be defined as $T = t/t_{\text{osc}}$.

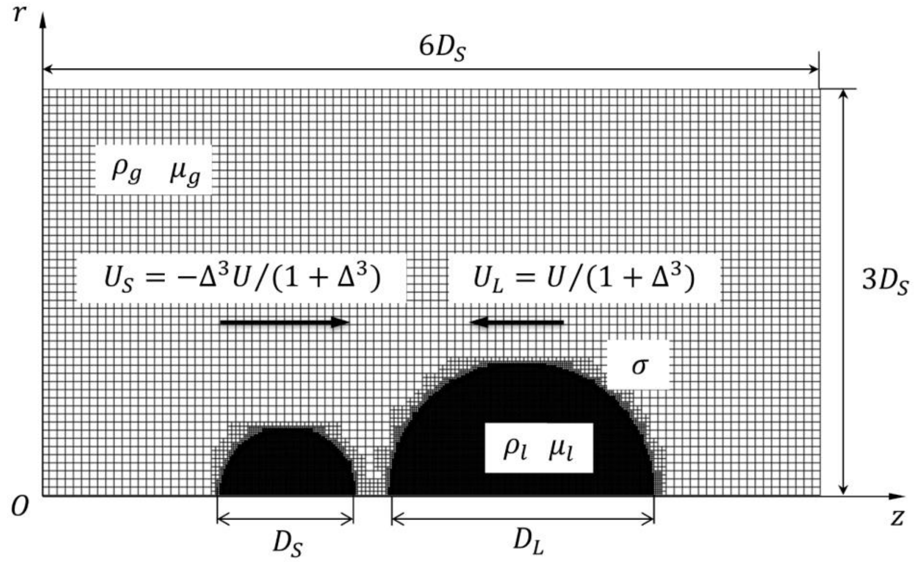

Figure 3.2 Schematic of the computational domain and adaptive mesh refinement for the head-on droplet collisions with non-vanishing Weber number.

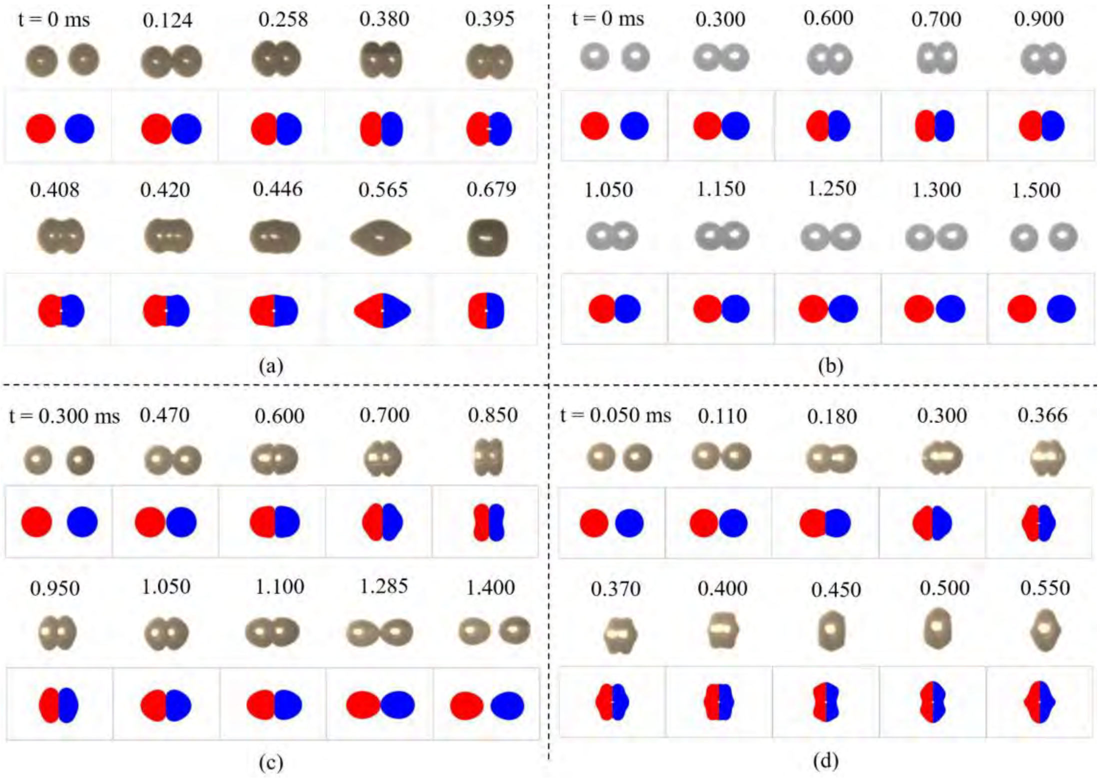

Figure 3.3 Head-on binary collisions between tetradecane droplets of equal size[41], (a) $We = 2.25$, coalescence; (b) $We = 2.27$, bouncing; (c) $We = 9.33$, bouncing; (d) $We = 13.63$, coalescence.

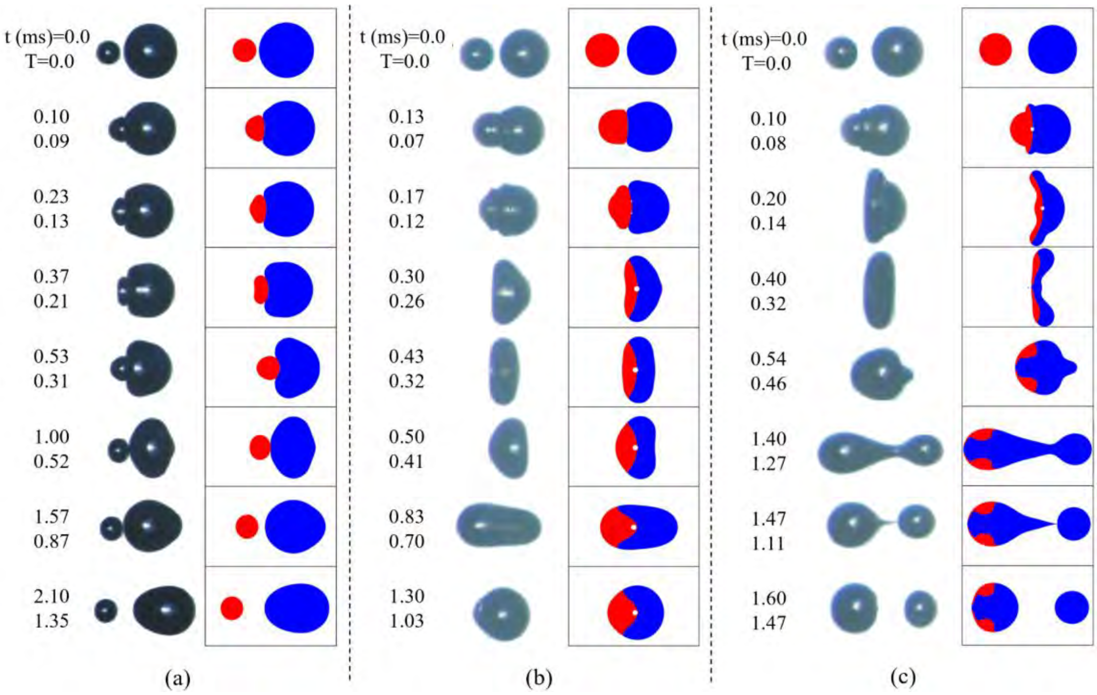

Figure 3.4 Head-on binary collisions between tetradecane droplets of unequal size[43], (a) $We = 7.0, \Delta = 2.33$, bouncing; (b) $We = 13.8, \Delta = 1.46$, coalescence; (c) $We = 52.8, \Delta = 1.50$, reflexive separation.

The preliminary validations on the head-on collision between two tetradecane droplets of equal size[41] and unequal sizes[43] are briefly presented in Figure 3.3 and Figure 3.4, respectively. The non-monotonic coalescence-bouncing-coalescence transition with increasing We is successfully simulated by choosing reasonable mesh parameters. Based on the previously discussed mesh refinement strategy for three physical zones, the mesh refinement levels for each case in Figure 3.3 are (4,6,8), (4,6,9), (4,6,10), and (4,6,10), respectively. It indicates that mesh refinement level of (4,6,8) is sufficient to simulate droplet coalescence with minor deformation for Figure 3.3(a), a larger mesh refinement level of (4,6,9) can delay the interface merging and result in droplet bouncing for Figure 3.3(b), and more larger mesh refinement level of (4,6,10) should be used to simulate droplet bouncing and coalescence with large droplet deformations for Figure 3.3(c) and (d). Furthermore, for simulating the bouncing and coalescence between tetradecane droplets of unequal sizes, a great larger mesh refinement level of (4,6,11) is required, as shown in Figure 3.4.

4 Non-monotonic viscous dissipation of bouncing droplets undergoing off-center collision

4.1 Background and objectives

The investigation of droplet collision could date back to the study on cloud aerosol, which was aimed to explain the mechanism of raindrop formation. Historically, studying the raindrop formation raised some arguments about which mechanism plays the dominant role, between the fragmentation of large droplets and the coalescence of minute droplets. It then spawned the early studies on the collision between two water droplets in standard atmosphere environment, resulting in the discovery of two collision outcomes, coalescence and separation. However, raindrops might have opposite charges[74] so that they tend to bounce off upon collision and their distributions of size, number density, and velocity are accordingly influenced.

In recent years, to understand the sprays of liquid fuels in combustion conditions, research efforts have been devoted to the collision between two hydrocarbon droplets[24, 25] in various gaseous environments, and most relevant studies were focused on droplet coalescence[14, 25, 43, 77] and the subsequent internal mixing[22, 23, 44, 56, 108]. Although not being sufficiently studied, interesting phenomena were also observed for droplet bouncing; for example, bouncing was found to occur to only fuel droplets[24, 25] but not water droplets in standard atmosphere environment. Furthermore, the collision outcomes can be significantly affected by the gas environment; specifically, increasing the gas pressure promotes droplet bouncing and decreasing the gas pressure promotes droplet coalescence[25, 109, 110]. Given the elevated pressure[25, 110] in real combustion chambers, droplet bouncing is a prominent collision outcome and of great significance in dense spray combustion. It has been verified both experimentally and numerically[111-113] that high pressure environment favors droplet bouncing in impinging jets.

Compared with the extensively studied droplet coalescence and separation, binary droplet bouncing has been investigated by only a few studies. AI-Dirawi and Bayly[37] experimentally studied the binary collision between identical droplets with different viscosities and proposed an improved model for the prediction of bouncing regimes in the nomogram of Weber number and impact parameter space. The dynamics of interfacial gas layer[114] and viscous effects[115] on the bouncing-to-merging transition in droplets impacting on the liquid film were studied, in which the droplet impacting on the liquid pool was a special case of binary droplet collision with infinite size ratio. Blanchette[116] proposed a model to describe droplets bouncing on an oscillated reservoir with various bouncing modes. Pan *et al.*[41] studied the evolution of energy budget for head-on bouncing between binary droplets of equal size both experimentally and numerically. Tang *et al.*[43] experimentally observed the head-on bouncing between binary droplets of unequal sizes. The present study attempts to focus on the three-dimensional (3D) off-center droplet bouncing, which is more practical and general than the axisymmetric head-on case. Chen and Yang[91] developed a thickness-based adaptive mesh refinement approach based on the Volume-of-fluid (VOF) method to simulate 3D off-center droplet bouncing. Hu *et al.*[117] used a VOF method to numerically study 3D off-center bouncing of alumina droplets. In order to emphasize the influence of off-center collision (measured by the impact parameter) on droplet bouncing, the present study limits its scope to droplets of equal size to avoid possible complexity introduced by variable size ratio, although the size ratio effects have been demonstrated to be important to droplet collision in other studies[15, 20, 22, 43, 46, 95, 108, 118].

In Lagrangian simulation of sprays, few previous works have investigated in detail the variation of the kinetic energy loss in off-center droplet bouncing. The classical O'Rourke model[38, 119] only considers droplet coalescence and grazing separation, in which droplet bouncing is treated as grazing collision with the kinetic energy dissipation factor $f_E \equiv 1 - \mathrm{KE_a}/\mathrm{KE_b} = 0$, where $\mathrm{KE_b}$ and $\mathrm{KE_a}$ respectively represent the kinetic energy of droplets before and after the collision. In lieu of O'Rourke's assumption, Zhang *et al.*[111] used an approximation of $f_E = 0.5$ suggested by Jiang *et al.*'s experiment[24]. The numerical simulation of Chen *et al.*[104] found that the normalized kinetic energy loss at the maximum droplet deformation decreases monotonically with increasing B. Zhang and Zhang[90] numerically studied the kinetic energy recovery and viscous dissipation of bouncing droplets undergoing head-on collision.

The present study attempts to promote both the physical understanding on the viscous dissipation of bouncing droplets undergoing off-center collision and the applications of the droplet bouncing modeling in Lagrangian simulations of sprays. The numerical methodology and validations are given in Section 4.2, followed by the preliminary analysis of the bouncing phenomenon and energy budget in Section 4.3. The detailed calculations and discussions of the viscous dissipation and the kinetic energy recovery are presented in Section 4.4 and Section 4.5, respectively.

4.2 Numerical methodology and validations

4.2.1 VOF method with two marker functions

As discussed in Chapter 3, for the conventional VOF method with one marker function, the mesh size resolving the interfaces between two colliding droplets must be sufficiently small in order to capture the outcome of bouncing; otherwise, the unphysical interface coalescence would occur numerically. Whereas for the modified

VOF method with two marker functions, the unphysical interface coalescence can be avoided even with the coarse mesh. Thus, to improve the computational efficiency, we use two volume fractions[92] in the present simulation, namely c_1 and c_2, to separately track the interface of each liquid droplet. The same idea of multiple marker functions was also implemented in Gerris by Hu *et al.*[117] to simulate binary droplet bouncing. Then, the density and viscosity can be constructed by the volume fraction as $\rho = (c_1 + c_2)\rho_l + (1 - c_1 - c_2)\rho_g$ and $\mu = (c_1 + c_2)\mu_l + (1 - c_1 - c_2)\mu_g$, in which the subscripts l and g denote the liquid and gas phases, respectively. The volume fraction $c_i (i = 1,2)$ satisfies the advection equation

$$\partial c_i/\partial t + \nabla \cdot (c_i \boldsymbol{u}) = 0 \tag{4.1}$$

with $c_i = 1$ for liquid phase, $c_i = 0$ for gas phase, and $0 < c_i < 1$ for gas-liquid interface.

To compare the differences between these two VOF methods, the time evolution of the droplet deformation for $We = 2.3$, $Oh = 2.80 \times 10^{-2}$, and $B = 0.0$[41] is shown in Figure 4.1(a), which involves three different cases: one marker function with fine mesh, two marker functions with fine mesh, and two marker functions with coarse mesh. The results show that droplet deformations collapse with each other for different interface mesh resolutions and marker functions.

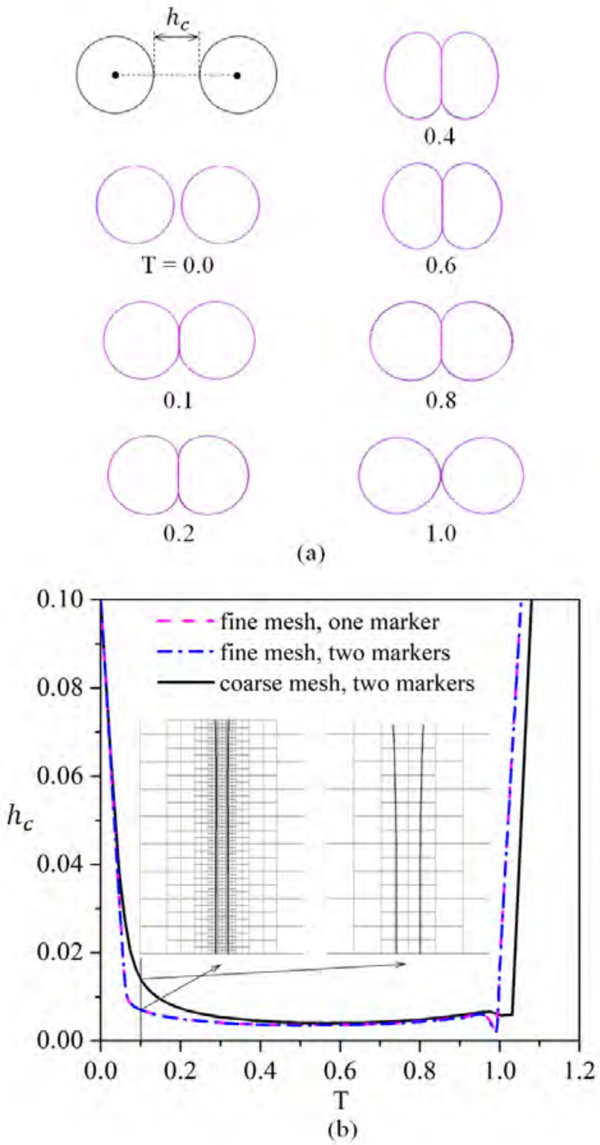

Figure 4.1 Comparison of (a) the droplet deformation and (b) the central interface distance, h_c, of colliding droplets by using different interface mesh resolution and marker functions for the case at $We = 2.3, Oh = 2.80 \times 10^{-2}$ and $B = 0.0$ [41].

Figure 4.1(b) further shows the time evolution of the central interface distance h_c for the above three cases, where h_c is defined as the minimum distance between two colliding interfaces along the mass center connection line, as illustrated in the first subfigure of Figure 4.1(a). The evolutions of h_c for the one marker function and the two marker functions, both with fine mesh, are identical, while there show some deviations from the two marker functions with coarse mesh. We argue that the VOF method by applying two marker functions with coarse mech is sufficiently accurate to simulate droplet bouncing in the present study for the following reasons. On the one hand, the minimum h_c at about T = 0.6 can be preserved; on the other hand, the deviations of h_c are in the order of $O(10^{-2})$ compared with the droplet diameter D and effectively only cause a more time offset which does not affect the droplet deformation or other physics during the process.

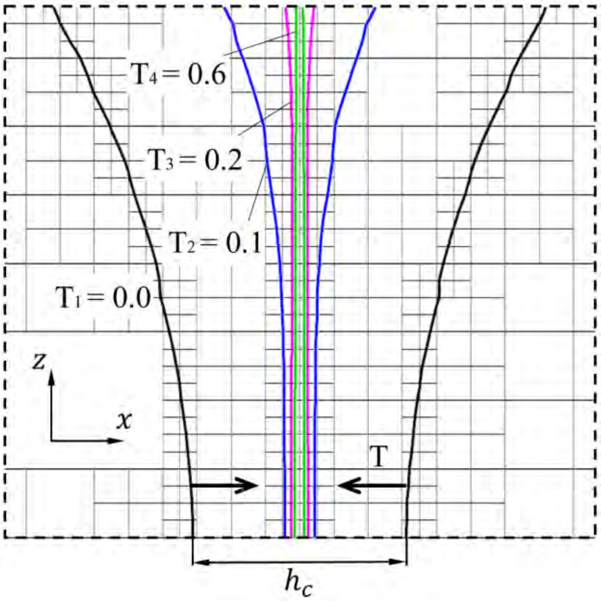

Figure 4.2 Evolution of interface positions and central interface distance h_c for the representative case shown in Figure 4.1.

Figure 4.2 shows droplet interface positions and central interface distance h_c at four chosen time instants, $\mathrm{T}_1, \mathrm{T}_2, \mathrm{T}_3$ and T_4. It indicates that droplet interfaces can be advected in the two immediately neighboring interface cells. The minimum central interface distance $h_c = 0.004$ occurs at about $\mathrm{T}_4 = 0.6$, which is nearly half of the minimum mesh size of $1/2^7 \approx 0.008$. Thus, in the present simulations, the minimum central interface distance h_c can be smaller than the minimum mesh size.

Although the two volume fractions independently describe the two droplets with no explicit conditions imposed for avoiding overlap of interfaces, we found that, at least in the present simulations with the concerned controlling parameters leading to droplet bouncing, the interfaces respectively belonging to the two droplets cannot contact and there is no overlap between the different VOF functions, which can be quantitatively verified by the measurement of the maximum excess of the combined volume fractions[92] that defined as $\max(c_1 + c_2 - 1)$. Consequently, the VOF method with two marker functions would always enforce droplet bouncing for any droplet collision process, and thus is applied in the present study for droplet bouncing cases that have been verified by experiment.

4.2.2 Numerical specifications

The 3D computational domain and numerical specifications are illustrated in Figure 4.3. The domain is $6D$ in length and $4D$ in both width and height, and all boundaries are specified with the free outflow boundary conditions. Two droplets of diameter D are specified to collide along the *x*- direction with a relative velocity, U, and zero velocities in the *y*- and *z*- directions. The *x*- velocity component for each droplet has the same magnitude of $U/2$ but opposite sign so that the linear momentum of the entire system remains zero. The *x*-*z* plane is established by the *x*-axis and the connection line denoted as OO', in which O and O' are the mass centers of the colliding droplets. The midpoint of OO' is located at the origin of the Cartesian coordinate system. It is noted that the *x*-*z* plane is always a plane of symmetry for the 3D colliding droplets. The deviation of the off-center collision from the head-on collision is qualified by χ, which is defined as the projection of OO' in the *z*-direction.

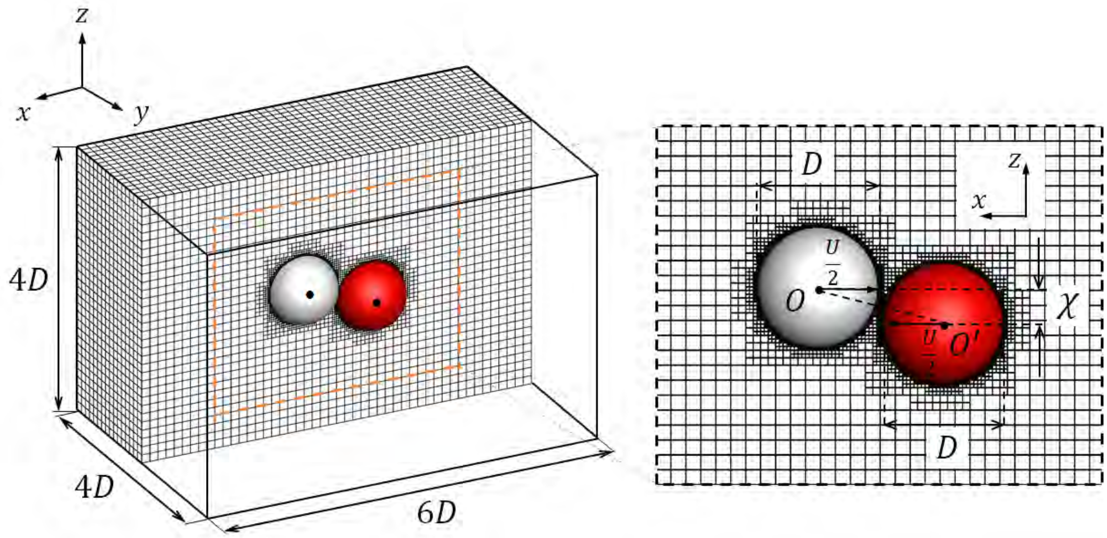

Figure 4.3 Computational domain and setup for 3D simulation of off-center droplet collision.

Choosing D, ρ_l, and σ as the basic units, we can nondimensionalize the eight relevant variables into five non-dimensional parameters, such as $We, Oh, B, \rho_g/\rho_l$, and μ_g/μ_l, which are the Weber number, $We = \rho_l D U^2/\sigma$; the impact parameter, $B = \chi/D$; and the Ohnesorge number, $Oh = \mu_l/\sqrt{\rho_l \sigma D}$. In the present study concerning the collision between droplets in standard atmosphere environment, the gas-liquid density ratio and viscosity ratio (using tetradecane as an example) are $\rho_g/\rho_l = 1.61 \times 10^{-3}$ and $\mu_g/\mu_l = 7.94 \times 10^{-3}$, which has insignificant influence on droplet deformation and energy transfer according to previous studies[15, 23]. Consequently, the present problem is completely controlled by the three parameters, We, Oh and B for a fixed set of ρ_g/ρ_l and μ_g/μ_l. The non-dimensional time is defined as $\mathrm{T} = t/t_{\mathrm{osc}}$, where t is the physical time and $t_{osc} = \sqrt{\rho_l D^3/\sigma}$ is proportional to the natural oscillation time of droplet.

In the present study, we used $6 \times 4 \times 4 = 96$ boxes with length L to constitute the entire computational domain, in which 6 boxes in *x*-direction and 4 boxes in *y*- and *z*- directions respectively. The droplet diameter is initialized as $D = L$. The computational domain is divided into three physical zones, namely the gas, the droplet, and the interface, and each zone has its own mesh refinement level denoted by N, which corresponds to a minimum mesh size of $O(2^{-N})$. Accordingly, (N_g, N_d, N_i) is used to describe the refinement level in the three zones. A typical simulation run with the mesh refinement level (3, 5, 7) results in 514204 grid points in the entire domain, which is equivalent to about 2.0×10^8 grid points if applying a uniform mesh with size of $O(2^{-7})$. The interface zone is identified by the VOF function with $0 < c_1 + c_2 < 1$. Given the maximum mesh refinement level N_i, the minimum mesh size is $L/2^{N_i}$ in the interface zone. Then the maximum numerical resolution[117] (MNR) of a droplet is defined as $\mathrm{MNR} = D/(L/(2^{N_i}+1)) = (2^{N_i}+1)\,D/L$. The maximum mesh refinement level $N = 7$ used in the present study corresponds to $\mathrm{MNR} = 129$. It takes about 100 hours of real time to run the simulation up to $\mathrm{T} = 2.0$ on an Intel Xeon(R) E5-2630 processor with 16 cores.

4.2.3 Numerical validations and grid-dependence analysis

To validate the present numerical setup, the head-on droplet bouncing at two critical transition Weber numbers, corresponding to the so-called “soft” and “hard” collisions, and an off-center droplet bouncing are simulated and compared with the experimental results from Pan *et al.*[41] and Qian and Law[25], respectively. Figure 4.4 shows the comparison between experimental images and simulation results. The presented simulation results are those having the most agreed droplet deformation with the experimental images, whereas the time discrepancies between them could serve as an indicator for the simulation performance.

Figure 4.4(a) and 4.4(b) show the experimental images and the simulation results of the head-on ($B = 0$) droplet bouncing at $We = 2.3$ and $Oh = 2.80 \times 10^{-2}$ ($t_{osc} = 1.06ms$)[41], respectively. The experimental and simulation times are nearly identical in early collision stages and begin to display slight discrepancies as time evolves in later stages. The time errors are generally less than 3% except it is about 5% at $\mathrm{T} = 1.08$.

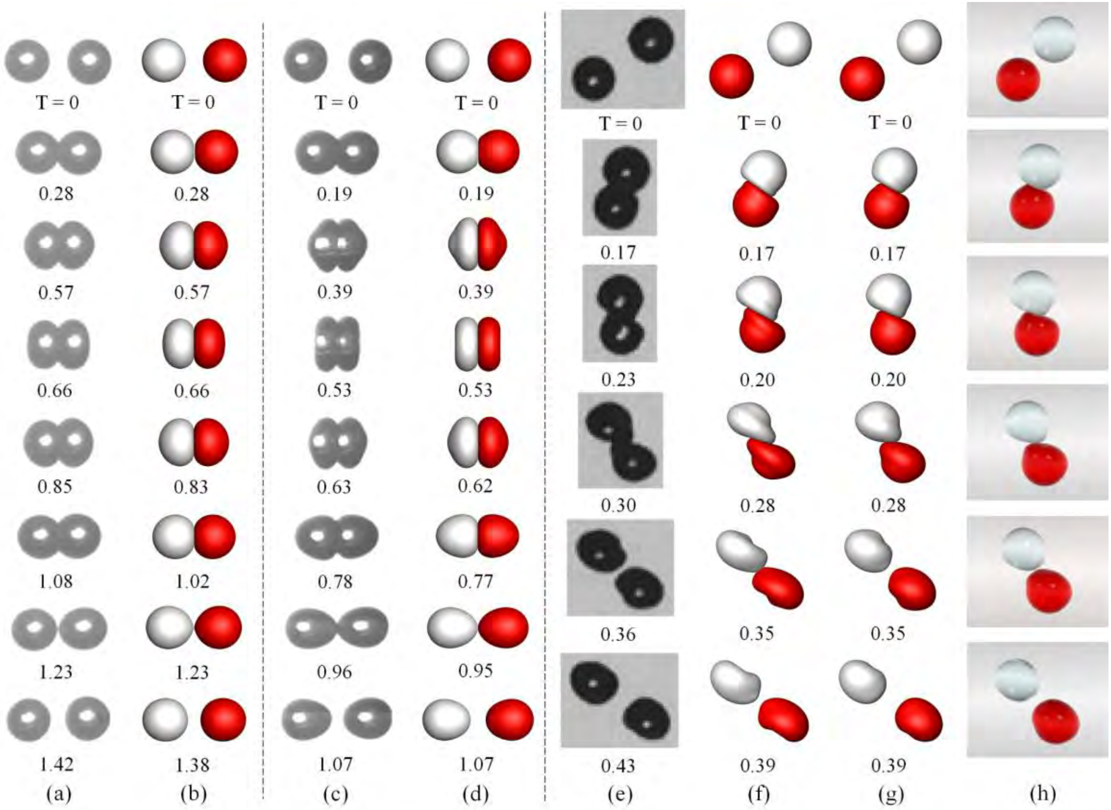

Figure 4.4 Comparison between the experimental images and the simulation results for bouncing droplets of equal size. (a) the experiment images from Figure 2 in Pan *et al.*[41] (head-on collision between tetradecane droplets in 1 atm air, $R = 170.6$ μm and $V_0 = 0.243\ \mathrm{m/s}$), (b) the simulation results at $We = 2.3, Oh = 2.80 \times 10^{-2}$ and $B = 0.0$ ($t_{osc} = 1.06ms$), (c) the experiment images from Figure 3 in Pan *et al.*[41] (head-on collision between tetradecane droplets in 1 atm air, $R = 167.6$ μm and $V_0 = 0.496\ \mathrm{m/s}$), (d) the simulation results at $We = 9.3, Oh = 2.78 \times 10^{-2}$ and $B = 0.0$ ($t_{osc} = 1.03ms$), (e) the experiment images from Figure 4(r) in Qian and Law[25] (off-center collision between tetradecane droplets in 1 atm air, $We = 14.5, Re = 149.1, R = 180$ μm and $B = 0.34$), (f)-(h) the simulation results at $We = 48.8, Oh = 2.80 \times 10^{-2}$ ($t_{osc} = 1.06ms$) and (f) $B = 0.72$, (g) $B = 0.82$, and (h) $B = 0.90$ (adapted from Figure 15 in Chen and Yang[91]). The physical time t is related to the computational time T by $T = t/t_{osc}$.

Similarly, Figure 4.4(c) and 4.4(d) show the experimental images and the simulation results of the head-on $(B = 0)$ droplet bouncing at $We = 9.3$ and $Oh = 2.78 \times 10^{-2}$ $(t_{osc} = 1.03ms)$[41], respectively. Again, the simulation agrees well the experiment and the time errors are less than 2%. The discrepancies between experiment and simulation may be attributed to the imperfect experimental conditions to be specified as follows. First, experimental images of droplet deformation show not perfectly symmetric with the small experimental error probably caused by the unavoidable disturbances of ambient gas flow to the droplets. Second, it might be caused by the experimental uncertainties in temporal resolution and the parameters measuring errors, for example, the droplets can be easily off-center in the direction perpendicular to the image plane. Furthermore, the above discussions about the imperfections of the experiments do not rule out the possible numerical errors.

Figure 4.4(e) shows the experimental images of off-center droplet bouncing adapted from Figure 4(r) in Qian and Law[25], who reported this case for $We = 14.5, Oh = 2.80 \times 10^{-2}$ and $B = 0.34$. After a careful examination of their experimental images, we found that the droplets were very likely to undergo a nearly grazing collision with the impact parameter to be within 0.7-0.9. This may be caused by the possibly misplaced captions of Figure 4(r) and Figure 4(q) in their paper[25]. To further substantiate our claim, the simulation results by using $We = 48.8, Oh =$

2.80×10^{-2} and $B = 0.72$ (used for Figure 4(q) in Qian and Law[25]), $B = 0.82$, and $B = 0.90$ (used for Figure 15 in Chen and Yang[91]) have been presented in Figure 4.4(f)-4.4(h), respectively. These simulations can be considered as a sensitivity analysis of the impact parameter. It is seen that these simulations predict very similar droplet deformation to the experiment, and that using $B = 0.82$ enables us to obtain quantitatively good agreement with the experiment. The time errors are about 10%, which is probably attributed to the experimental uncertainties in the measurement for time and collision parameters[25].

Although a more detailed analysis on the experimental uncertainty of measured impact parameter is beyond the scope of the present study, a few remarks about this issue may be of use for future numerical studies that adopt those earlier experimental images for validation purpose. In Qian and Law[25], the droplet sizes and velocity and thereby We and B were determined from the recorded images on a video recorder by using a strobelight synchronized with the droplet generator. The reported measurement errors of droplet size and impact parameter in Qian and Law[25] are about 10%. Gotaas *et al.*[120] have pointed out that such an experimental method in measuring impact parameter is generally not very accurate, and the measurement errors could be larger. Consequently, Gotaas *et al.*[120] proposed a more accurate and efficient aliasing method for continuous variation of impact parameter over its whole range from zero to unity.

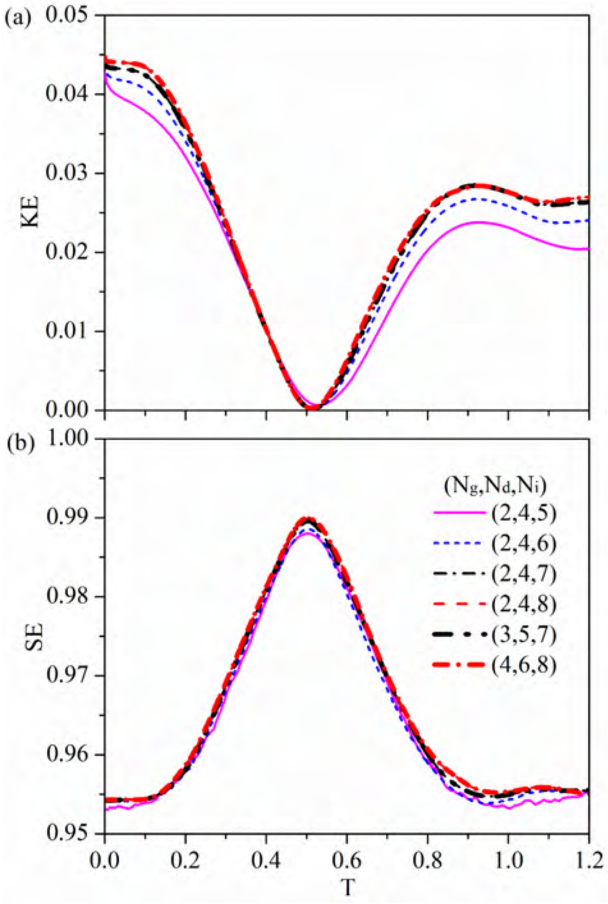

Figure 4.5 Grid-independence analysis in terms of (a) the droplet kinetic energy (KE) and (b) the surface energy (SE) of the liquid droplets, which are normalized by the initial total energy $(E_{k0} + \sigma S_0)$, for the validation case (a) shown in Figure 4.4. (N_g, N_d, N_i) is used to describe the mesh refinement levels in each zone of the gas, the liquid, and the droplet interface.

The grid-independence analysis was performed for the validation case (a) of Figure 4.4. The kinetic energy (KE) and surface energy (SE) of the liquid droplets are normalized by the initial total energy and compared for totally six different mesh refinement level sets (N_g, N_d, N_i), as shown in Figure 4.5. The initial total energy is defined as $E_{k0} + \sigma S_0$, in which $E_{k0} = \pi We/24$ is the initial kinetic energy and $S_0 = 2\pi$ is the initial surface energy, respectively. By fixing the mesh refinement level of the gas and the droplet zones at $N_g = 2$ and $N_d = 4$, respectively, we can analyze the grid dependence of the interface zone, and the results show convergence up to $\mathrm{T} = 1.2$ as increasing the mesh refinement level from $N_i = 7$ to $N_i = 8$. Similarly, the result comparison between (2, 4, 7) and (3, 5, 7) and further comparison between (2, 4, 8) and (4, 6, 8) also imply convergence of simulation with different mesh refinement levels of the gas and the liquid zones. As a balance between computational cost and accuracy, the intermediate mesh refinement level of (3, 5, 7) has been used in the validation cases and all simulations in the following sections.

4.3 Preliminary analysis

4.3.1 Phenomenological description

The representative case of $We = 9.3$ and $Oh = 2.80 \times 10^{-2}$ at four impact parameters, $B = 0.0,\ 0.3,\ 0.6$ and 0.9, has been used to phenomenologically describe the differences between the head-on and the off-center droplet bouncing, as shown in Figure 4.6. The projection of droplet deformation on the symmetry (*x-z*) plane is shown in the first row of each case, in which the mass of the colliding droplet centers, O and O', are indicated by black solid points. To analyze the flow field within the droplets, the pressure contours and streamlines on the symmetry (*x-z*) plane and on the YOO' plane where the y-axis and the line OO' lie, are shown in the second and third rows of each case in Figure 4.6.

A prominent similarity between head-on and off-center collisions is the formation of a flat interaction region as the two droplets "squeeze" against each other. Although the dimension of this region and the duration of its existence both decrease notably with increasing the impact parameter, it always results in the locally enhanced capillary pressure around the rim of the interaction region where curvature is large. Once the inertia responsible for the "squeezing" is depleted, the deformed droplets are driven by the capillary pressure difference to bounce back, meanwhile converting the surface energy back to the kinetic energy. Subsequently, the droplets experience several oscillation periods before completely recovering their original spherical shape, which happens at later times beyond those of Figure 4.6. It is noted that the pressure distributions and streamlines on YOO' plane for head-on and off-center collisions are qualitatively similar except the pressure amplitude for off-center collisions is smaller. The distinctive differences can be observed on the x-z plane for off-center collisions that the mass deviation in z-direction results in the asymmetric pressure distribution for each droplet. In addition, the shear flow is clearly seen in the vicinity of the droplet interaction region only for off-center collisions on the symmetry (x-z) plane but not on the YOO' plane nor any plane of the head-on collision.

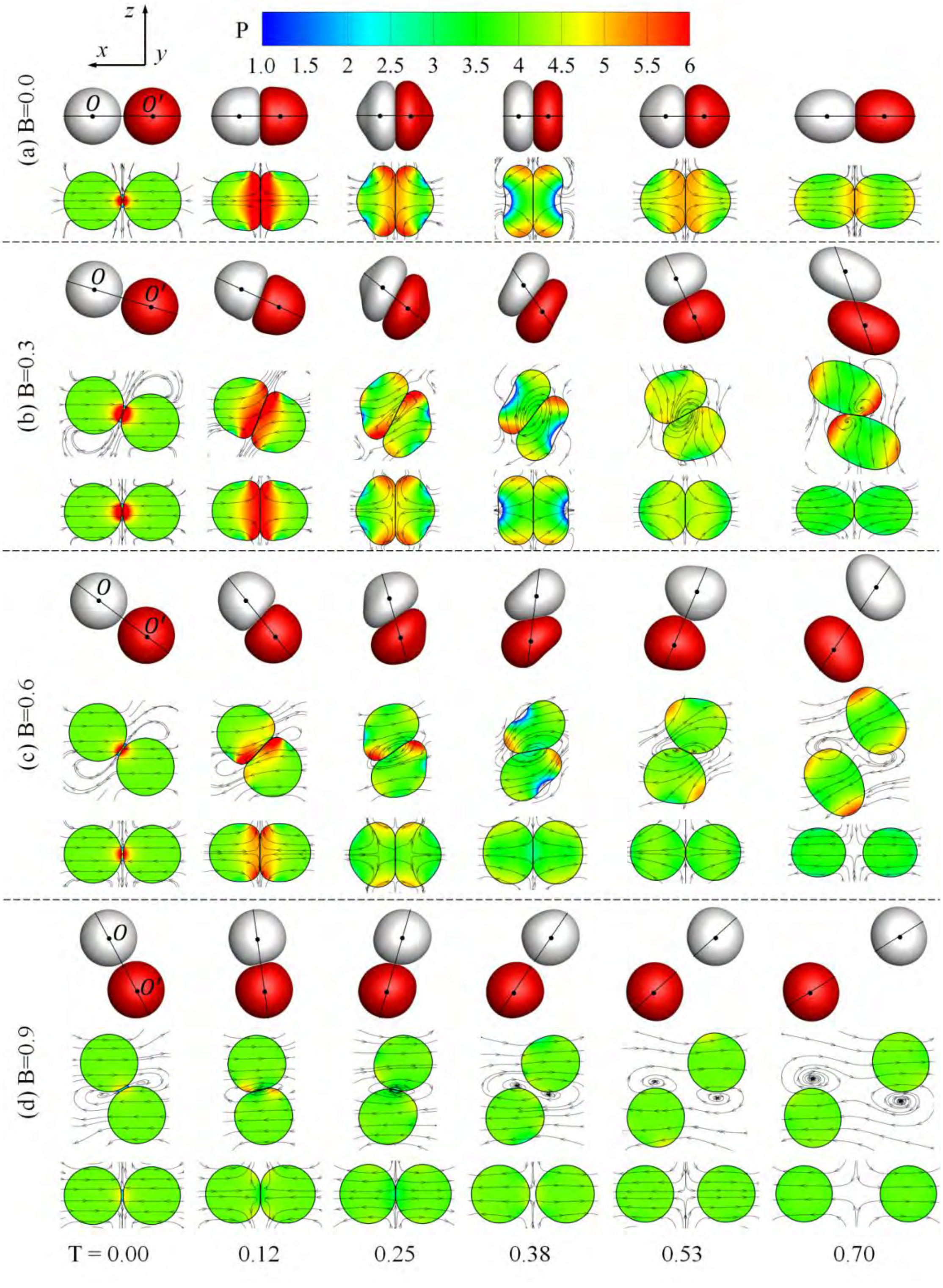

Figure 4.6 Comparison of droplet deformation, pressure profiles and streamlines between (a) head-on bounding (on the symmetry plane *x*-*z* only because it is axisymmetric) and (b-d) off-center bouncing (both on the symmetry plane *x*-*z* at first two rows and on the plane YOO' consisting of *y*-axis and mass center connection line OO' at the last row) for the representative case at $We = 9.3$ and $Oh = 2.78 \times 10^{-2}$.

4.3.2 Energy budget

Based on the preliminary phenomenological observations, the entire collision process can be divided into three stages, namely impacting, bouncing, and oscillating stages. The energy budget analysis is conducted based on liquid droplets[24, 25, 41, 43], as shown in Figure 4.7, in which the time evolution of the kinetic energy (KE) and the surface energy (SE) of the liquid droplets are normalized by their initial total energy $E_{k0} + \sigma S_0$. $\mathrm{T} = 0.0$ is defined as the time instant when $D_{OO'} = D$ for the first time as the two droplets approaching each other, where $D_{OO'}$ is the mass center distance shown in Figure 4.7. It follows that the droplet impacting stage starts from $\mathrm{T} = 0.0$ to the time instant with SE reaching its first maximum. The droplet bouncing stage then extends from the first local maximum to the first local minimum of SE, with the rest being the droplet oscillating stage. It is noted that the separation point (local maxima and minima of SE) and time duration for each stage are different between different impact parameters. The time evolution of $D_{OO'}$ shows that the increase of mass center distance for $B = 0.3$ is slowest with delayed droplet bouncing as the droplet entanglement time is prolonged for moderately off-center collisions, indicating a non-monotonic variation with increasing B.

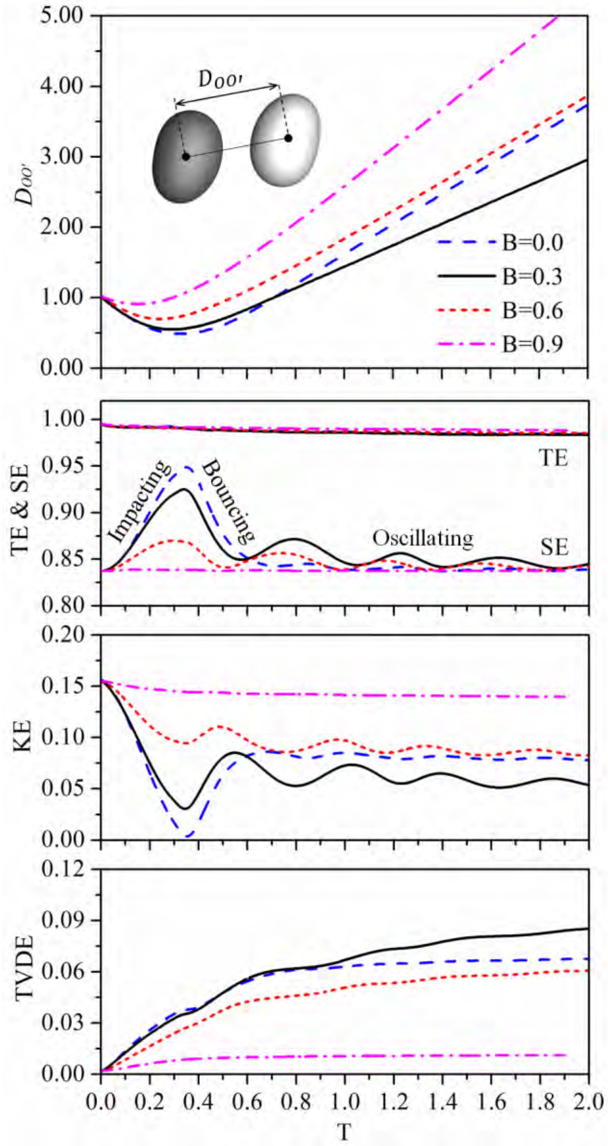

Figure 4.7 Evolution of mass center distance $D_{OO'}$ and energy budget analysis of the off-center droplet bouncing for the representative case at $We = 9.3$ and $Oh = 2.80 \times 10^{-2}$. The total energy (TE), the surface energy (SE), the kinetic energy (KE), and the total viscous dissipation energy (TVDE) of the liquid droplets are normalized by the initial total energy. The entire droplet collision process can be divided into three stages, namely impacting, bouncing, and oscillating stages, based on the phenomenological observations.

During the droplet impacting stage, both the total decrement of KE and the total increment of SE decrease monotonically with increasing B from 0.0 to 0.9. This is because increasing B tends to decrease the effective impact velocity $(U\sqrt{1-B^2}/2)$

of colliding droplets along the mass center connection line and thereby results in a smaller droplet deformation with a smaller KE loss. During the droplet bouncing stage, the droplets start to bounce back with a decrease of SE and an increase of KE. Then, during the droplet oscillating stage, several apparent oscillations of SE and KE can be observed owing to the unbalanced capillary pressure shown in Figure 4.6, particularly for the intermediate impact parameters at $B = 0.3$ and $B = 0.6$, and these oscillations are gradually attenuated by the viscous dissipation. An interesting observation throughout the entire droplet oscillating stage is that the KE for $B = 0.3$ is significantly lower than the other cases.

We note that KE and SE show the same variation trend accompanied by the deforming interface during droplet oscillation stages. The oscillation frequency of KE and SE increases with the impact parameter from $B = 0.0$ to $B = 0.6$, as the local maxima of SE shown in Figure 4.7. However, the non-dimensional oscillation period is not unity, indicating the droplet oscillation time is not the natural oscillation time.

To further explain this observation, the total viscous dissipation energy (TVDE) of the liquid droplets normalized by the initial total energy is shown in Figure 4.7. The TVDE is defined by

$$\mathrm{TVDE(T)} = \int_0^{\mathrm{T}} \left(\int_{V_l} \phi \, dV \right) d\mathrm{T}' \tag{4.2}$$

where V_l is the volume of liquid droplets and ϕ is the local viscous dissipation rate (VDR) given by[121]

$$\phi = 2\mu\left[\left(\frac{\partial u}{\partial x}\right)^2 + \left(\frac{\partial v}{\partial y}\right)^2 + \left(\frac{\partial w}{\partial z}\right)^2\right] + \mu\left[\left(\frac{\partial u}{\partial y} + \frac{\partial v}{\partial x}\right)^2 + \left(\frac{\partial v}{\partial z} + \frac{\partial w}{\partial y}\right)^2 + \left(\frac{\partial w}{\partial x} + \frac{\partial u}{\partial z}\right)^2\right] \tag{4.3}$$

As shown in Figure 4.7, the TVDE of $B = 0.3$ during droplet bouncing and oscillating stages is the largest among all Bs, indicating that the non-monotonic kinetic energy recovery is caused by the non-monotonic TVDE. To further understand the viscous dissipation of bouncing droplets in different stages, the temporal total viscous dissipation rate will be discussed in Section IV.

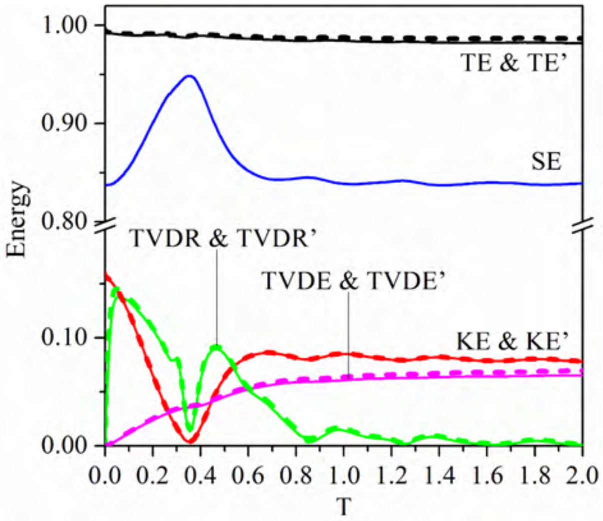

Figure 4.8 Comparison of the evolution of the total energy (TE for the liquid droplets and TE' for the total flow field), the surface energy (SE), the kinetic energy (KE and KE'), the total viscous dissipation rate (TVDR and TVDR') and the total viscous dissipation energy (TVDE and TVDE') by respectively considering liquid phase only (solid lines) and both liquid and gas phases (dashed lines) for the representative case at $We = 9.3, Oh = 2.78 \times 10^{-2}$ and $B = 0.0$.

Furthermore, it is seen that the normalized total energy of droplets (TE=KE+SE+TVDE) is slightly lower than 1 and decreases with time, which can be explained as follows. First, the total energy (TE) is not exactly the total flow energy (TE'=KE'+SE+TVDE' where the superscript prime denotes liquid and gas phases) because the contribution from the gas flow is neglected. Second, as shown in Figure 4.8, TE' including the kinetic energy and viscous dissipation of both liquid and gas phases is slightly larger than that (TE) of liquid phase only. This verifies that the energy budget of the gas flow is insignificant compared with that of the liquid droplets. Third, the normalized TE' being still slightly lower than 1 might be due to the numerical dissipation. It is noted that the above is a posteriori examination of energy conservation, because the energy conservation equation is not solved in the present simulation framework.

4.4 Viscous dissipation for off-center collisions

4.4.1 Enhanced viscous dissipation for moderately off-center collisions

The total viscous dissipation rate (TVDR), defined as a volume integral $\int_{V_l} \phi \, dV$, and the contours of local VDR are illustrated in Figure 4.9(a) and 4.9(b-d), respectively, to explain the enhanced viscous dissipation at $B = 0.3$. It is seen that in all cases both the droplet impacting stage and the droplet bouncing stage contain a single peak of TVDR, whereas the droplet oscillating stage has several local maxima.

The time instants corresponding to the first three local maxima of TVDR are denoted $\mathrm{T}_1, \mathrm{T}_2$ and T_3.

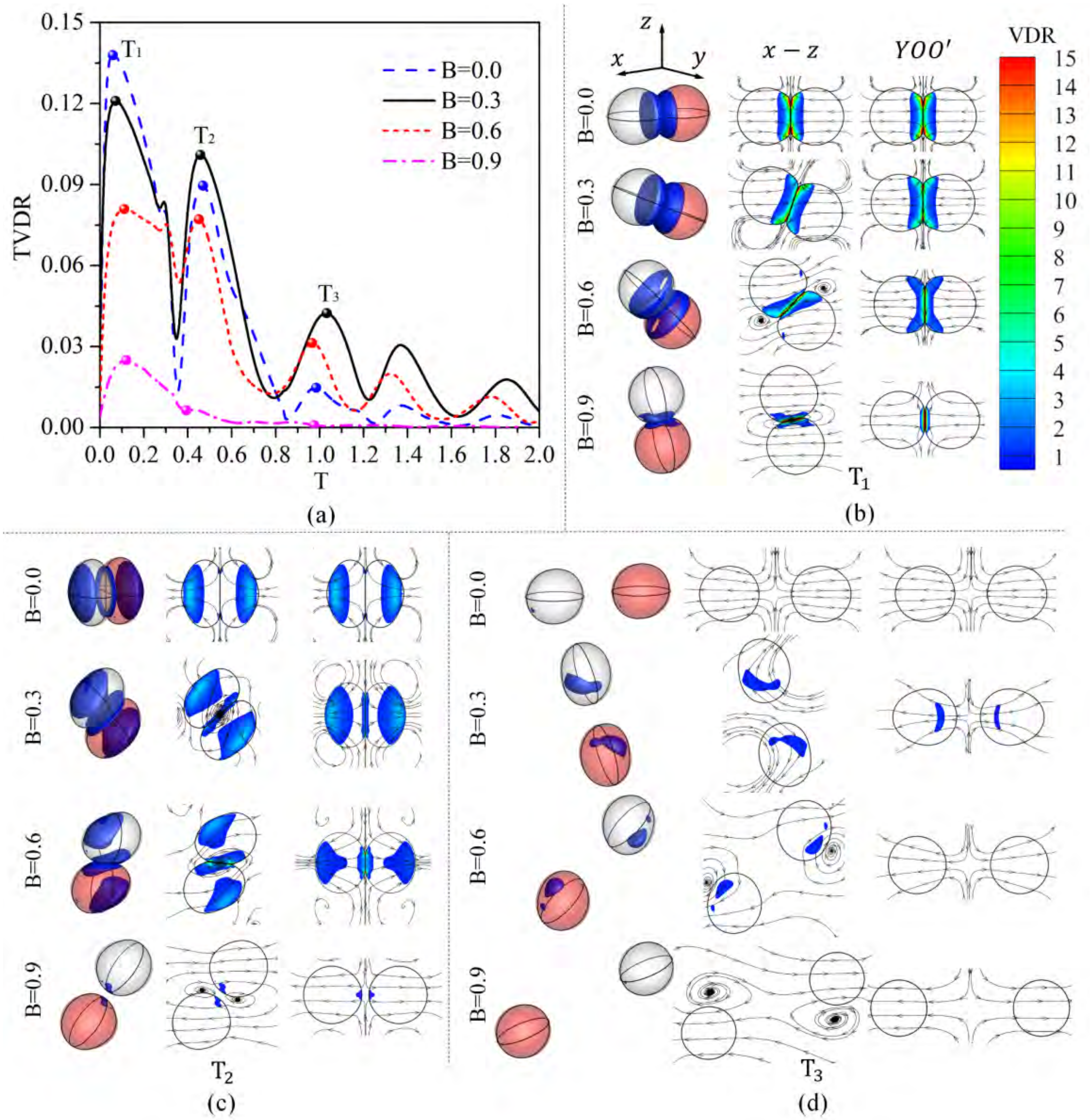

Figure 4.9 Comparison of the (a) total viscous dissipation rate (TVDR) and (b-d) the contour of local viscous dissipation rate (VDR) at three chosen time instants, $\mathrm{T}_1, \mathrm{T}_2$ and T_3, for the representative case at $We = 9.3$ and $Oh = 2.80 \times 10^{-2}$. The contours have been blanked with a low threshold value of 0.5 for clear comparison of the VDR concentration that shown both in three-dimensional and on symmetry (*x*-*z*) and YOO' plane that defined in Figure 4.6.

A common feature during the droplet impacting stage is that it has the highest peak of TVDR and contributes to the majority of the overall viscous dissipation. As shown by the VDR contours at T_1 in Figure 4.9(b), the local VDR is mainly distributed around the droplets interaction region where the liquid is both compressed along the OO' direction and expanded radially, displaying a boundary-layer-like internal flow that was also observed in previous theoretical analysis[17] and numerical simulation[90]. Furthermore, comparing the cases of different Bs, it is seen that the TVDR decreases monotonically with increasing B during the droplet impacting stage. As the droplet deformation in this stage is inertia-dominant, this observation can be understood by an approximate estimation of the TVDE, previously proposed by Jiang *et al.*[24] and Tang *et al.*[43], as $\alpha E_k(B) = \alpha(1 - B^2)E_k(B = 0)$ where α is the viscous dissipation coefficient and $E_k(B)$ is the effective impact KE of the colliding droplets along the mass center connection line.

During the droplet bouncing stage, the droplets bounce back under the capillary pressure difference with the SE transferring into the KE. Figure 4.9(c) shows that at T_2 the VDR in the droplet interior being away from the interaction region decreases from maximum at $B = 0.0$ to nearly vanishing at $B = 0.9$. In this case, the TVDR can be estimated as $2\mu_l(\Delta\mathrm{SE})V_l/mD^2$, where $\Delta\mathrm{SE}$ is the change of SE, the characteristic velocity is $u \sim \sqrt{2\Delta\mathrm{SE}/m}$, and the characteristic length is D. Since

$\Delta\mathrm{SE}$ is closely related to the deformation of the droplets, the formula indicates that a larger droplet deformation in the droplet impacting stage would cause a larger TVDR in the droplet bouncing stage, which is consistent with the above observation. On the other hand, it is interesting to note that the local VDR emerges in the vicinity of the droplet interaction region only for off-center collisions but not for the head-on collision. This part of VDR is caused by the shear flow of off-center collisions as it becomes more prominent with increasing B. Apparently, the two parts of VDR, respectively corresponding to the droplet deformation and the shear effect between the droplets, together form a competition mechanism which is responsible for the non-monotonic variation of TVDR as a function of B.

As shown in Figure 4.9(a), the fluctuations of TVDR during the droplet impacting stage emerge at small and intermediate impact parameters but not large impact parameters. Thereby, Figure 4.10 shows the closeup of the fluctuation region and the corresponding contours of local viscous dissipation rate (VDR) for $B = 0.0, 0.3$ and 0.6. The locally enhanced TVDR is mainly located at the droplet interior being away from the interaction region with the convex interface tends to be flatten. That is consistent with the first peak of TVDR induced by the droplet impacting at initial stages, which can be understood as that the large viscous dissipation is generally accompanied by the intensive interface deformation with large curvature gradient change on the interface.

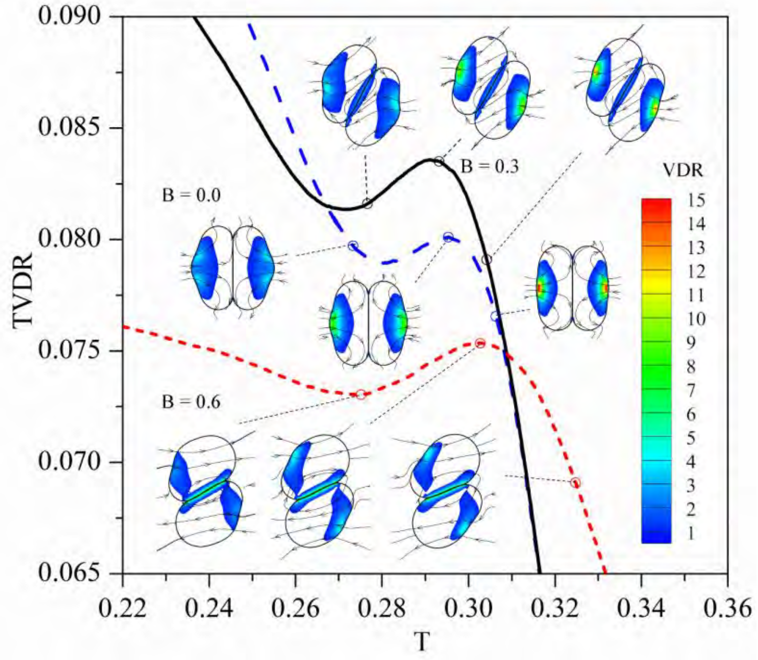

Figure 4.10 The local fluctuations of total viscous dissipation rate (TVDR) and the contour of local viscous dissipation rate (VDR) (embedded subfigures) at three different time instants during the droplet impacting stage for the representative case at $We = 9.3$ and $Oh = 2.80 \times 10^{-2}$.

4.4.2 Quantitative explanation of the competition mechanism of VDRs

To further understand the competition mechanism between the VDR related to the droplet deformation and the VDR owing to the shear effects of off-center collisions, it is natural to separate the VDR terms in Equation 4.3 into two parts, namely the TVDR(N) related to the normal strains (the first three terms) and the TVDR(S) related to the shear strains (the last three terms). The shaded area in Figure 4.11(a) and 4.11(b) respectively shows the TVDR(N) and TVDR(S) in the droplet impacting and bouncing stages. The two representative time instants, $\mathrm{T_n}$ and $\mathrm{T_s}$, respectively correspond to the local maximum of TVDR(N) in the impacting stage and the local maximum of TVDR(S) in the bouncing stage. As a reference, the TVDR(N)+TVDR(S) is plotted in the droplet oscillating stage. The case of $B = 0.9$ has been excluded from this discussion because it does not have a notable bouncing stage owing to the dominance of the shear effect, as indicated by Figure 4.11(a) and 4.11(b).

It can be observed that for the small impact parameter at $B = 0.0$ the TVDR(N) is generally larger than the TVDR(S), whereas for the moderate impact parameters at $B = 0.3$ and 0.6 the TVDR(N) and TVDR(S) become equally significant to the TVDR. Specifically, during the droplet impacting stage and droplet bouncing stage, the TVDR(N) decreases monotonically as increasing B as shown in Figure 4.11(a) and visualized by the local VDR contours at time $\mathrm{T_n}$ in Figure 4.11(c), whereas the TVDR(S) increase monotonically from $B = 0.0$ to 0.6 as seen in Figure 4.11(b) and the local VDR contours of Figure 4.11(c) at time $\mathrm{T_s}$. Therefore, we have demonstrated the competition mechanism through the different variation trends of TVDR(N) and TVDR(S) with increasing B, which accounts for the non-monotonicity of TVDR being the largest around $B = 0.3$.

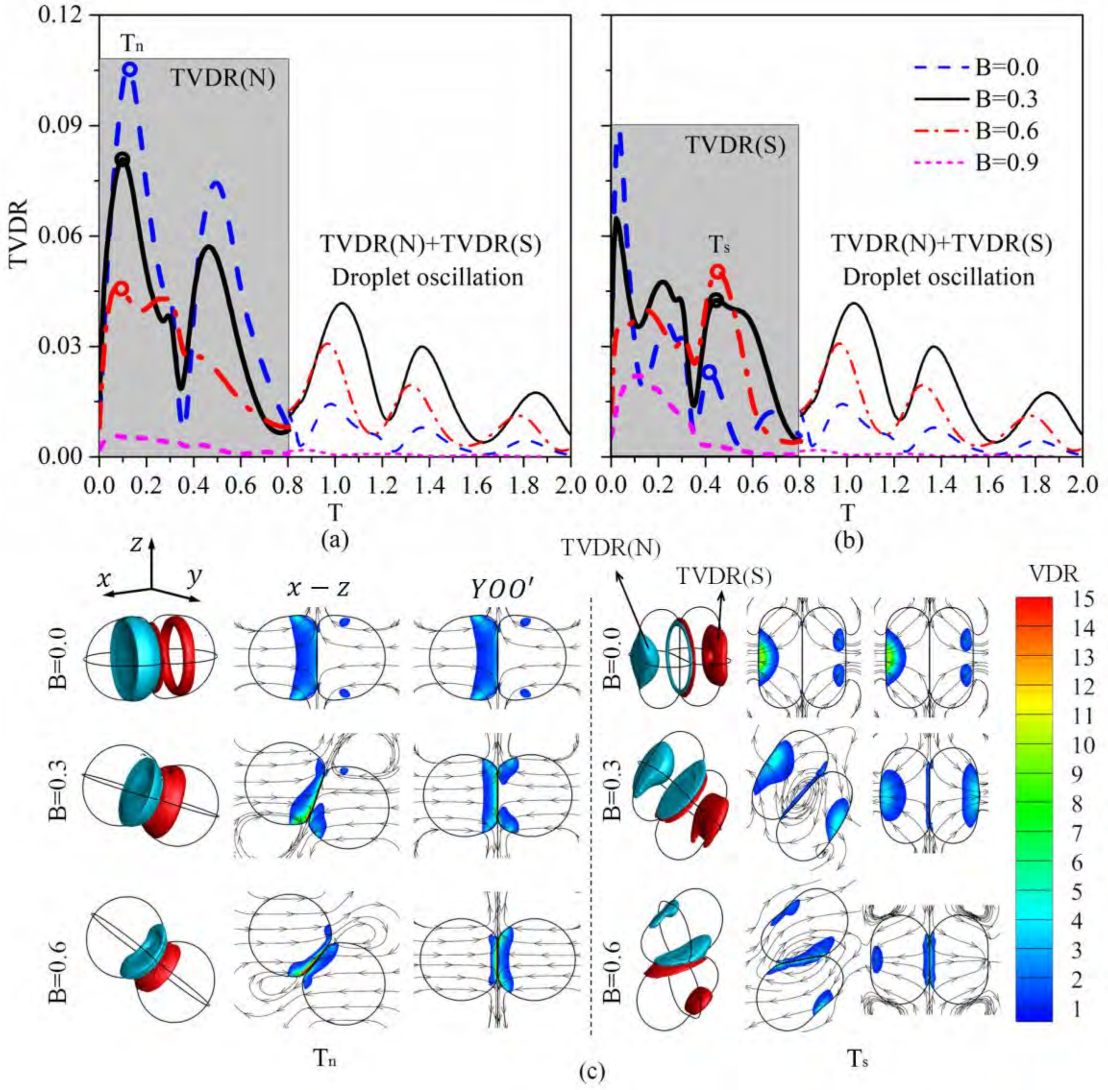

Figure 4.11 Comparison of the total viscous dissipation rate (TVDR) induced by (a) the normal strains [TVDR (N)] and (b) the shear strains [TVDR (S)], and (c) the contour of local VDR at time instants of $\mathrm{T_n}$ and $\mathrm{T_s}$, for the representative case at $We = 9.3$ and $Oh = 2.80 \times 10^{-2}$.

4.5 Non-monotonic kinetic energy dissipation

4.5.1 The dependence of kinetic energy dissipation on We and Oh

In Lagrangian simulation of sprays[27, 30, 38, 122, 123] where the binary droplet collision is simplified as the collision between two mass points, the post-collision velocity of each droplet has to be determined from secondary models to serve as input. Since the mass center trajectories always lie on the symmetry (*x*-*z*) plane, only four unknown velocities in the *x*- and *z*- directions are needed for a pair of colliding droplets. Given the conservations of the momentum in the *x*- and *z*- directions and the angular momentum in the *x*-*z* plane, one requires the kinetic energy dissipation factor f_E to close the equation system for the terminal velocity calculation. In the present study, we can compute f_E numerically with $\mathrm{KE_b}$ determined from the initial conditions and $\mathrm{KE_a}$ evaluated at the time instant when $D_{OO'} = 3D$, after which the $\mathrm{KE_a}$ is effectively unchanged for all cases. Accordingly, the kinetic energy recovery factor is calculated as $1 - f_E$.

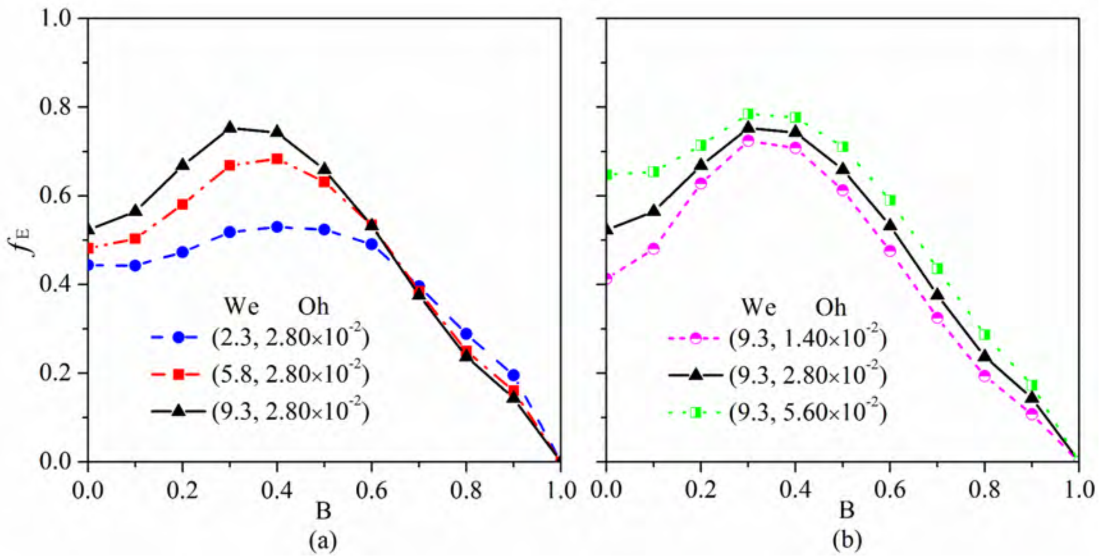

Figure 4.12 Variation of the kinetic energy dissipation factor f_E with impact parameters B at different We and Oh.

Figure 4.12(a) shows f_E with varying B for different We. For small and intermediate B in the range of 0.0 ~ 0.7, f_E increases with We and the deviations of f_E among different We are enlarged at intermediate B. This is because the viscous dissipation induced by the droplet deformation is inertial-controlled and enhanced as increasing We. However, it is interesting to find that, f_E is not sensitive with varying We for B in the range of 0.7 ~ 1.0. This indicates that We is a secondary factor to the viscous dissipation for near grazing collisions, which is likely the outcome of the shear effects dominating over the droplet deformation. Furthermore, the critical impact parameter B_{cr}, which is defined as the B corresponding to the local maximum of f_E (for fixed We and Oh), decreases slightly as increasing We. This is again attributed to the competition between the inertia and shear effects that increasing We causes greater relative importance of the droplet deformation on viscous dissipation so that the maximum f_E occurs at a smaller B_{cr}.

Figure 4.12(b) shows the variation of f_E as a function of B for different Oh. It is seen that f_E increases monotonically with Oh for all B, which is clearly attributed to the increased viscosity. However, the gaps among f_E of different Oh appear to be the largest at $B = 0.0$. The effect of Oh is further studied in Figure 4.13, which shows that the increase of f_E is approximately linearly proportional to the increase of Oh/Oh_{ref} (or equivalently the ratio of the viscous coefficient μ_l) where Oh is normalized by a reference $Oh_{\mathrm{ref}} = 1.4 \times 10^{-2}$. However, the slop for different impact parameters is not unity. This can be understood by the VDR estimation in Equation 4.3 that the viscous dissipation is a synergistic effect that is influenced not only by the viscous coefficient but also by the velocity gradients related to the internal flow and the integral droplet interaction time. Furthermore, the slops for different impact parameters seem to be consistent except the cases of $B = 0.0$. This is likely to reflect the additional dissipation effect associated with the distinct droplet deformation, which occurs as a byproduct of changing viscosity when the impact inertia is large at small B.

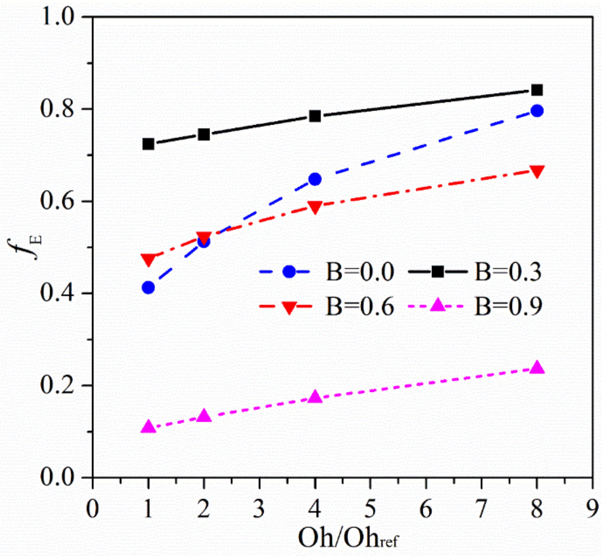

Figure 4.13 Variation of the kinetic energy dissipation factor f_E with Oh for the representative $We = 9.3$.

4.5.2 An approximate fitting formula

The above results have demonstrated an overall general trend of the non-monotonic kinetic energy recovery and viscous dissipation for different We and Oh. Here, we propose an approximate fitting formula of f_E/f_{E0} to serve for Lagrangian spray simulations based on the following considerations. First, this formula reflects the most important finding of the present study that the kinetic energy dissipation factor varies non-monotonically with the impact parameter. Second, the functional dependence of the factor on We and Oh for head-on collisions, namely, $f_{E0}(We, Oh) = f_E(We, Oh, B = 0)$, has been comprehensively studied by Zhang and Zhang[90]. The normalized f_E by f_{E0} for different We and Oh is shown in Figure 4.14(a) with scattering points. Thus, following their conclusions, we incorporate the additional impact parameter effect to attain a simple fitting formula

$$f_E/f_{E0} = a(B - B_{cr})^2 + b \tag{4.4}$$

to describe the non-monotonic variation of f_E/f_{E0} as increasing B. The parabola on the $f_E/f_{E0} - B$ plane must cross the point of (0, 1) by definition, yielding $a = (1 - b)/{B_{cr}}^2 < 0$, and the point of (B_{cr}, b) to reflect the existence of a maximum value on the parabola. We found that the proposed approximate formula with $B_{cr} = 0.5 - 0.2(We/10)$ and $b = 0.83 + 0.3(We/10) + 0.9(Oh/10^{-2})^{-1}$ can satisfactorily fit our numerical data for the concerned parameter space of $We = 2.3 \sim 9.3$ and $Oh = 1.4 \times 10^{-2} \sim 5.6 \times 10^{-2}$, as the lines shown in Figure 4.14(a).

Figure 4.14(b) shows the comparison between numerical and fitting results, indicating that they are in good agreement at small and intermediate B in the range of 0.0 ~ 0.6 although they deviate at large B where the small f_E/f_{E0} is insignificant to the practical purpose. The more accurate high-order fitting formula merits future investigations, given more numerical or experimental data, but is beyond the scope of the present study.

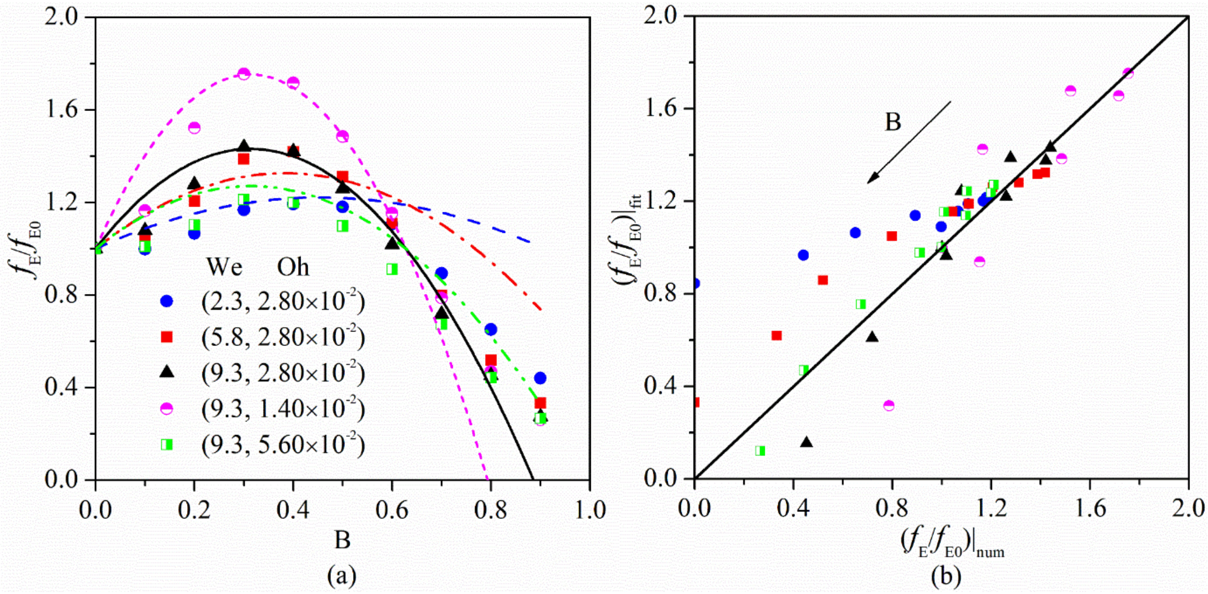

Figure 4.14 Comparison of (a) the kinetic energy dissipation factor f_E normalized by f_{E0} that obtained from previous study[90] (scattering points of numerical results and lines of fitting formula) and (b) deviation of f_E/f_{E0} between numerical (horizontal) and fitting (vertical) results.

4.6 Concluding remarks

Two droplets bouncing undergoing off-center collisions were simulated in the present study by using a modified VOF approach with two marker functions and validated against experiments of both head-on and off-center collisions. The implementation of multiple marker functions helped to avoid the unphysical numerical coalescence under relatively coarse mesh, so that it allows us to study the 3D off-center droplet bouncing with substantially increased computational efficiency.

The analysis of mass center trajectory demonstrates that the droplet entanglement time is prolonged for moderately off-center collisions. A non-monotonic kinetic energy recovery with varying impact parameter was observed, which is attributed to the enhanced viscous dissipation of moderately off-center collisions.

The present study has strived to unveil and interpret the non-monotonicity. Specifically, as increasing B from 0 to 1, the VDR in the droplet interior being away from the interaction region decreases because of the reduced droplet deformation, whereas the VDR in the vicinity of the droplet interaction region increases owing to the enhanced droplet shear flow. The competition mechanism between these two parts of VDR accounts for the enhanced viscous dissipation at intermediate B in the early stages of droplet collision; while the enhanced droplet oscillation owing to the unbalanced capillary pressure distributions results in the further increase of viscous dissipation at intermediate B in the late periods of droplet oscillation. This mechanism can also be understood as the competition between VDR induced by normal strains and shear strains, which quantitively verifies our discussions and helps us understand the viscous dissipation for off-center droplet collisions.

The non-monotonic kinetic energy recovery has been quantitatively verified to be a general phenomenon for various We and Oh. The total viscous dissipation is understood as a concerted work by the liquid viscosity, internal-flow-induced droplet deformation, and droplet interaction time. A correlation formula, $f_E/f_{E0} = a(B - B_{cr})^2 + b$, has been proposed for $We = 2.3 \sim 9.3$ and $Oh = 1.4 \times 10^{-2} \sim 5.6 \times 10^{-2}$. This formula could be useful for the droplet collision modeling in the Lagrangian simulation of sprays, particularly under the elevated gas pressure in the real combustion engines.

5 Helicity analysis of binary collision between initially spinning droplets

5.1 Background and objectives

For the modelling of binary droplet collision in Lagrangian simulation of sprays, the general 3D collision is simplified as the collision between two rigid bodies without self-rotations. In classical mechanics, the arbitrary 3D collision between two rotation free rigid bodies in laboratory coordinate can be always equivalent to a 2D collision in the mass center coordinate, in which the 2D plane consists of the mass center connection line and the direction line of relative velocity. Consequently, the system has four freedoms corresponding to four post-collision velocities for each rigid body in 2D (*x*-*z*) plane, in which the velocities are uniquely determined by the conservations of the linear momentum in the *x*- and *z*- directions, the angular momentum perpendicular to the *x*-*z* plane, and the kinetic energy dissipation factor f_E[21, 90].

The binary droplet collision in real situations is however more complicated than the simplified collision between two rigid bodies without self-rotation, because the real inelastic collision involves the droplet stretching and rotations. The spinning motion can be created either from the droplet injectors or after off-center collisions. Bradley and Stow[10] showed the experimental images of droplet spin after coalescence and measured the angle of rotation as a function of time and impact parameter. Ashgriz and Poo[14] proposed the schematic of reflexive separation for the off-center droplet collision by considering the droplet spin after coalescence. Rotational energy[24, 30] has been considered in various models for predicting outcomes of off-center droplet collisions. The fact that spinning motion of a droplet can take part of energy from its translational motion and has not been considered in the previous models. It is apparent that the spinning droplets can collide with each other because subsequent collisions are probable in practical dense sprays[38, 111, 123]. However, the collision dynamics between spinning droplets has not been reported in the literature.

The single spinning droplet have only been investigated by a few studies. The shape of a weightless spinning liquid droplet is governed by the balance between the surface tension and centrifugal forces[124]. The spinning droplet shows axisymmetric shape with slow rotations and becomes unstable to various shapes with specific range of critical angular velocity. Brown and Scriven[125] used finite-element method to trace the equilibrium state of axisymmetric, two-, three- and four-lobed drop shape for rotating droplets with increasing the angular momentum, and analyzed the critical transition between different drop shapes. The droplet distortion and spinning can also be induced by the rotating environmental flows[126]. Kitahata *et al.*[127] proposed a simple mechanical model to measure the liquid surface tension by the relation of oscillation frequency varying with the rotational speed and oscillation amplitude of a levitated rotating droplet. The phenomena of droplet spinning can be further enriched by considering the influence of external fields. Janiaud *et al.*[128] experimentally investigated the behavior of microscopic ferrofluid droplets under the rotating external magnetic field, and presented the fascinating drop shapes such as starfish, rod-like or pancake shape, co-rotating, creeping snakes, swirling loops and rings, in a phase diagram. Bernando *et al.*[129] experimentally investigated the shape of rotating superfluid helium nanodroplets and confirmed the existence of oblate metastable superfluid droplets with large angular momenta beyond the classical bifurcation threshold. The binary collision between spinning droplets has however not been reported in the literature.

It is noted that, owing to the existence of symmetry (*x*-*z*) plane, the off-center droplet collision can be separately described as the translational movement of droplets' mass centers on the *x*-*z* plane and the rotation motion of each droplet based on their rotation axes parallel to *y*-axis. Thus, the total angular momentum in *y*-direction can be divided into two parts of orbital and spin angular momentum. The orbital angular momentum loss in the droplet collision modeling can be considered by introducing a factor of f_P (Page 99 of[38]) that describes the angular momentum that goes into rotational motion of the droplet after collisions. The droplet rotations after collisions can take a part of energy from the translational kinetic energy, and thereby the kinetic energy dissipation factor in the simplified modeling is generally underestimated if not considering the droplet rotation effects. In practical dense sprays involving large amount of binary droplet collisions, the post-collision droplet is very likely spinning rapidly to participate in another binary collision process, in which the droplet deformation and internal flow can be influenced significantly accordingly.

Vortex dynamics has been demonstrated to be of unique significance in understanding the physics of droplet collision, for example, vortex ring formation[130] in the coalescence of a droplet into a liquid pool[131] and vortex-induced internal mixing[23] upon the coalescence of two droplets. It is expected that the collision between spinning droplets accompanied with initially nonzero vorticity would enrich the understanding of droplet collision substantially. The vortex-dynamical interpretation of the spinning effects on the droplet deformation and energy transfer can be obtained by the viscous dissipation, helicity, and enstrophy analysis.

Generally, the arbitrary binary collision between two identical droplets free of rotations is “point reflection” based on the original point in the mass center coordinate. Regardless of the size disparity of droplets, the spinning effects of droplets before collisions can break such symmetry in complex manners. Specially, the collision dynamics between two spinning droplets are influenced by the direction of rotation, the amplitude of spinning, and the droplet shape upon the initial contact for both droplets undergoing head-on or off-center collisions. Consequently, the interactions between binary droplets become more significant and it is worthy to study each droplet separately during the collision process. In order to emphasize the spinning effects of droplets before collisions, the present study limits its scope to the head-on collision of bouncing between droplets of equal size only, so that to void possible complexity introduced by the geometrical asymmetry of varying impact parameters and droplet size disparity, although the off-center collision[21, 70, 91, 132] and size ratio effects[15, 20, 22, 23, 43, 46, 108, 118] have been demonstrated to be important to droplet collision in other studies. The study starts from the head-on collision between one spinning droplet and another rotation-free droplet, and then extends to the collision between droplets with same or opposite spinning direction and amplitude.

The present work seeks to numerically investigate the collision of two spinning droplets of equal size, and particularly focuses on the vortex-dynamical interpretation of the spinning effects on the viscous dissipation energy and vortex interactions. The numerical specifications are presented in Section 5.2, followed by the results and discussions in Section 5.3.

5.2 Evaluation of collision-induced droplet rotation

It has not been seen in the literature on the experimental measurement of the rotational speed of droplets after collisions, which is probably attributed to the difficulty of experimentally resolving the droplet spinning motion under the sub-mini scales of length and time. To setup the present computations of spinning droplet collision, we must first estimate what is the physically realistic range of the rotational speed for a droplet that is made to spin as the result of a preceding collision. Thus, it is worthy to analyze the previous numerical results of off-center bouncing droplets[21] in order to quantify the collision-induced droplet rotation.

We choose two representative cases of off-center droplet bouncing at $B = 0.4$ and $Oh = 2.8 \times 10^{-2}$ and at $We = 9.3$ and $We = 20$, respectively, as shown in Figure 5.1, to characterize the rotational deformation and angular velocity ω of droplets. In the figure, the solid point and line are the center of mass and initial intersecting plane, which change with the droplet deformation and rotational motion. It is seen that the bouncing droplets revolve about 90 degrees for each image during a period of nondimensional time T from 0.4 to 1.6, as shown in Figure 5.1. Consequently, the angular velocity of bouncing droplets can be estimated as

$$\omega = \frac{N}{\mathrm{T} * t_{osc}} = \frac{0.25}{0.4 \times 1.06 \times 10^{-3}\ \mathrm{s}} \approx 3700\,\mathrm{rad/s} \qquad (5.1)$$

where the characteristic oscillation time is $t_{osc} = 1.06\,\mathrm{ms}$. The non-dimensional time is defined as $\mathrm{T} = t/t_{\mathrm{osc}}$, where t is the physical time and $t_{osc} = \sqrt{\rho_l {D_l}^3/\sigma_l}$ is proportional to the natural oscillation time of droplet, in which ρ_l, D_l and σ_l are density, diameter and surface tension of liquid droplet, respectively.

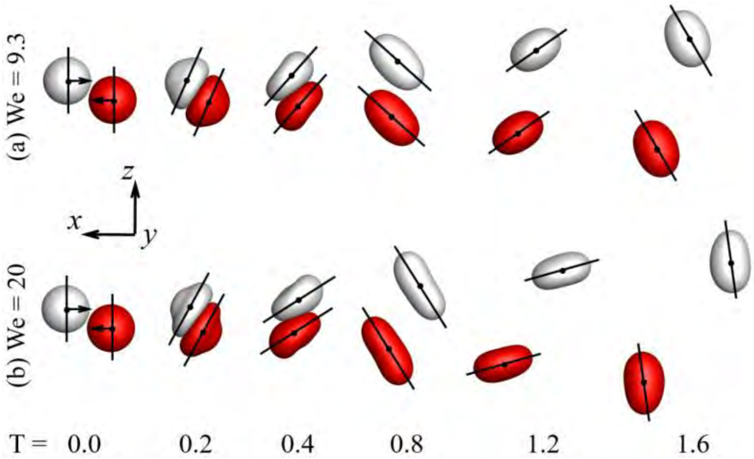

Figure 5.1 Evolution of droplet deformation and rotational motion for bouncing droplets undergoing off-center collisions at $B = 0.4$ and $Oh = 2.8 \times 10^{-2}$ for different $We = 9.3$ and $We = 20$. The characteristic oscillation time is $t_{osc} = 1.06\,\mathrm{ms}$.

We note that the angular velocity can also be determined by $\omega = \omega_c \frac{M_s}{I}$, where M_s is the dimensionless spinning angular momentum, I is the dimensionless inertia of moment for an approximately spherical droplet, and ω_c is the characteristic angular velocity given as

$$\omega_c = \frac{2V_l}{D_l} = 2\sqrt{\sigma_l/\rho_l {D_l}^3} = 1886\ \mathrm{s}^{-1}. \tag{5.2}$$

Thereby, as shown in Figure 5.2(a), ω increases rapidly at early stage from T=0.0 to about 0.5 and then remains unchanged during late stages. Droplet rotation after off-center collisions favors larger We, with approximate $3768\ \mathrm{s}^{-1}$ and $2512\ \mathrm{s}^{-1}$

for $We = 20$ and $We = 9.3$, respectively, which is consistent with the approximate estimation in Figure 5.1.

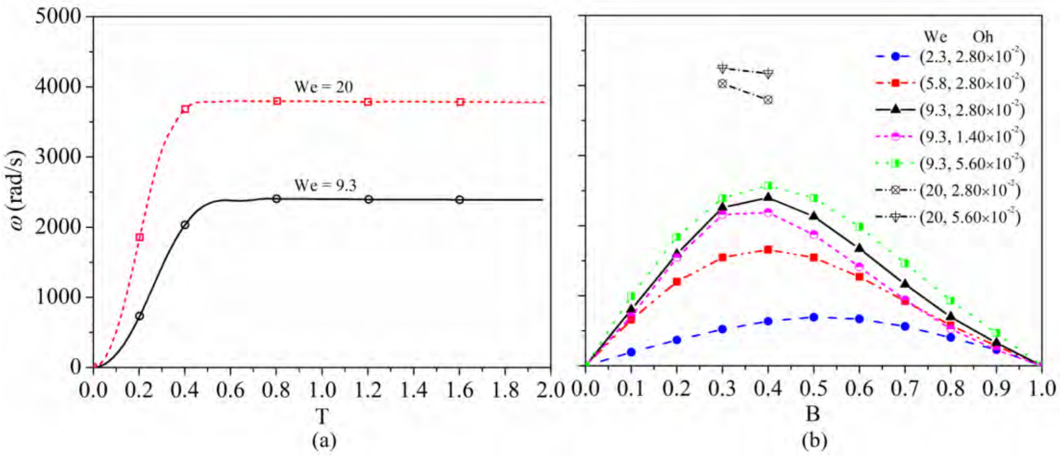

Figure 5.2 Evolution of (a) angular velocity ω at $B = 0.4$ and $Oh = 2.8 \times 10^{-2}$ for different $We = 9.3$ and $We = 20$, and (b) comparison of ω with impact parameter for bouncing droplets undergoing off-center collisions.

For arbitrary two-body problem of binary droplet collision that specified in Chapter 4, owing to the existence of symmetry plane, the initial angular momentum has only one component in *y*-direction. With the reduced mass $\mu = \frac{1}{2}m$, the inertia of moment $I = \mu D^2$, and the angular velocity upon droplet contact is UB/D, the dimensionless total angular momentum (TAM) can be calculated as $M = \frac{1}{2}mDUB = \frac{1}{12}\pi\rho D^4\sqrt{We\sigma/\rho D}\,B = \frac{1}{12}\pi\sqrt{We}B$. We noted that the TAM in *y*-direction (perpendicular to *x*-*z* plane) for the off-center droplet collision consists of two parts: namely the orbital angular momentum (OAM) of liquid droplets on the *x*-*z* plane and the spinning angular momentum (SAM) with respect to the rotation axis that across the mass center and being perpendicular to *x*-*z* plane. Both the TAM, OAM and SAM are vanishing for the head-on droplet collision. Whereas for the off-center collision, the initial TAM (OAM) can be partially transferred to SAM, which is normally ignored in the simplified modelling of binary droplet collision, but can be included in a more complete modelling involving droplet rotation by introducing an OAM loss factor of f_{M} (Page 99 of[38]).

Figure 5.2(b) shows the angular velocity ω of bouncing droplets after off-center collisions at different We and Oh. It is seen that ω increases with We but is slightly influenced by Oh, and varies non-monotonically with B. This can be understood as a synergistic consequence by the shear effects increasing with B and the interaction time (or droplet deformation) decreasing with B to rotate the bouncing droplets.

Considering that the critical We of bouncing-coalescence transition can be increased for the droplet collision at elevated pressure environment[133, 134], or for example, the critical We of bouncing-coalescence transition for off-center collisions between tetradecane droplets in gaseous environment is about 25 at $B = 0.4$[134], which implies the increased We would induce a larger droplet rotation speed that as high as $6000\ \mathrm{s}^{-1}$. The approximate angular velocity of spinning droplets after the off-center collision, at least in the present study, is in the rage of $500{\sim}6000\ \mathrm{s}^{-1}$.

5.3 Problem description and numerical specifications

The 3D schematic of the head-on collision between a spinning droplet and a non-spinning droplet is illustrated in Figure 5.3. The similar 3D computational domain in the previous work[21] was applied in the present study, which is $6D$ in length and $4D$ in both width and height with all boundaries specified with the free outflow boundary conditions. Two droplets of diameter D are specified to collide along the *x*- direction with a relative velocity, U, and zero velocities in the *y*- and *z*-

directions. The x- velocity component for each droplet has the same magnitude of $U/2$ but opposite sign so that the linear momentum of the entire system remains zero. The x-y plane is established by the mass center connection line denoted as O_1O_2 (or equivalent to the relative velocity direction for the head-on droplet collision) of x-axis and the arbitrary primary spinning axis of l_{O_1}, in which O_1 and O_2 are the mass centers of the colliding droplets. he midpoint of O_1O_2 is located at the origin of the Cartesian coordinate system. The droplet spinning direction is defaulted as clockwise from positive of x-direction, and thereby $0° \leq \theta \leq 90°$ represents all collision possibilities owing to the intrinsic axial symmetry of the head-on collision between two identical droplets.

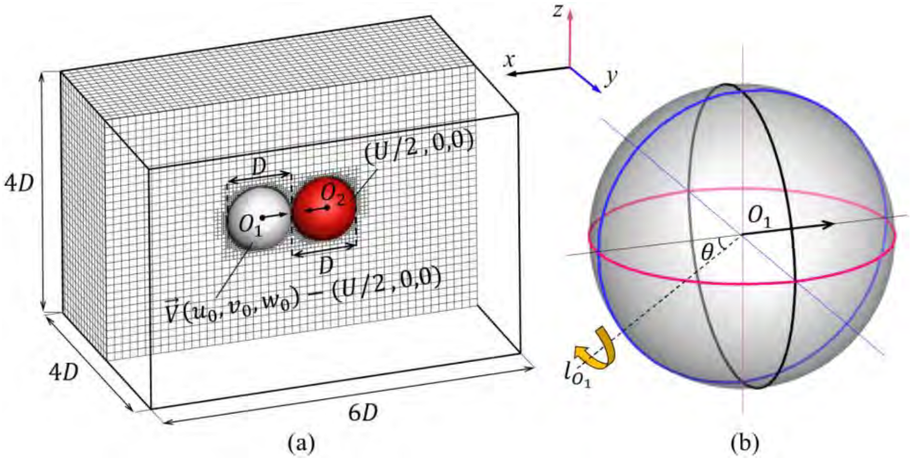

Figure 5.3 Schematic of (a) three-dimensional computational domain and (b) setup of rotation axis for the head-on collision between a spinning droplet O_1 and a non-spinning droplet O_2.

In the present study concerning the head-on collision between identical spinning droplets, the non-dimensional parameters discussed in previous work[21] can be reduced to only We and Oh, which are the Weber number, $We = \rho_l DU^2/\sigma$ and the Ohnesorge number, $Oh = \mu_l/\sqrt{\rho_l \sigma D}$. To avoid the unnecessary complexity of phenomenological description and to facilitate the comparison of varying spinning effects, the present numerical study focuses on the representative situation at fixed $We = 9.3$, $Oh = 2.8 \times 10^{-2}$, and $\omega_0 = \sqrt{We} = 5800\mathrm{s}^{-1}$ with $We = 9.3$ because ω_0 is in the reasonable range of angular velocity evaluated in Section 5.2. The initial velocity vector of spinning droplet O_1 is the sum of $\vec{V}(u_0, v_0, w_0) - (U/2, 0,0)$, where the components of $\vec{V}$ in *x*-, *y*-, and *z*- directions, respectively, varies in space and can be initialized as

$$\begin{bmatrix} u_0 \\ v_0 \\ w_0 \end{bmatrix} = \begin{bmatrix} \dfrac{\sqrt{We}}{2} - z\omega_0 \sin\theta \\ z\omega_0 \cos\theta \\ \omega_0(x\sin\theta - y\cos\theta) \end{bmatrix} (0 \leq \theta \leq 90^{\circ}) \qquad (5.3).$$

Whereas, the initial velocity vector of non-spinning droplet O_2 is a constant of $(U/2, 0,0)$. The numerical validations and grid-independence analysis have been performed in the previous study[21]. Consequently, as a balance between computational cost and accuracy, the intermediate mesh refinement level of (3, 5, 7) has been used for all simulations in the following sections.

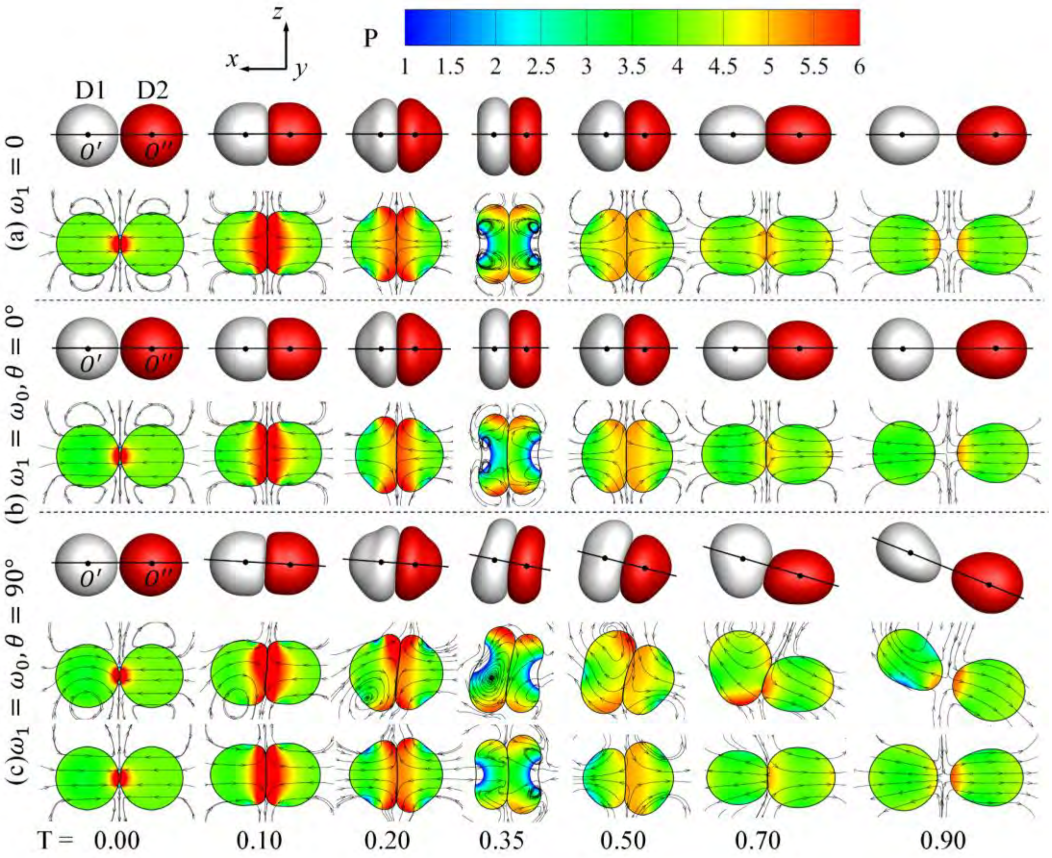

Figure 5.4 Comparison of droplet deformation, pressure profiles, and streamlines for the head-on collision between identical droplets of (a) rotation free with $\omega_0 = 0$, (b) spinning with $\omega = \omega_0$ and $\theta = 0^{\circ}$, and (c) spinning with $\omega = \omega_0$ and $\theta = 90^{\circ}$. The results are shown on the *x*-*z* plane only for (a) and (b) because they are axisymmetric, but both on the *x*-*z* plane at first two rows and on the plane YO_1O_2 consisting of *y*-axis and O_1O_2 at the last row. The initially spinning droplet is denoted as “D1” while the other droplet with no rotation is denoted as “D2”。

5.4 Preliminary analysis

5.4.1 Phenomenological description

Figure 5.4 phenomenologically describes the deformation of the head-on collision between a spinning droplet and a non-spinning droplet with different rotation axis, by the representative case with fixed $We = 9.3$, $Oh = 2.8 \times 10^{-2}$, and $\omega = \omega_0$. Two rotation axes of $\theta = 0^{\circ}$ and $\theta = 90^{\circ}$ are chosen and shown in Figure 5.4(b) and 5.4(c), respectively, and compared with the collision between two non-spinning droplets shown in Figure 5.4(a). It is noted that only droplet “D1” is specified as spinning while droplet “D2” is non-spinning for case (b) and (c) so that to clearly show the interactions between spinning and non-spinning droplets by breaking the symmetry between two identical droplets. The results on the symmetry (*x*-*z*) plane are only shown for case (a) and (b) whereas both on the symmetry (*x*-*z*) plane and on the YO_1O_2 plane, where the y-axis and the line O_1O_2 lie, are shown for case (c).

A prominent similarity of axisymmetric deformation is observed for case (a) and (b). The “squeeze” of two droplets results in the locally enhanced capillary pressure around the rim of the formed interaction region where curvature is large. As shown in Figure 5.4(b), the spinning effect of droplet “D1” breaks the minor symmetry to that of droplet “D2”, in which “D1” shows a larger radial expansion than “D2”. This is because the centrifugal force induced by spinning effects based on *x*-axis ($\theta = 0^{\circ}$) is also in radial direction and thereby promote the droplet deformation. Once the inertia responsible for the “squeezing” is depleted, the deformed droplets are driven by the capillary pressure difference to bounce back, meanwhile converting the surface energy back to the kinetic energy. Subsequently, the droplets experience several oscillation periods before completely recovering their original spherical shape, which happens at later times beyond those of Figure 5.4. It is seemingly that "D1" with spinning is earlier in recovering to the spherical shape than "D2".

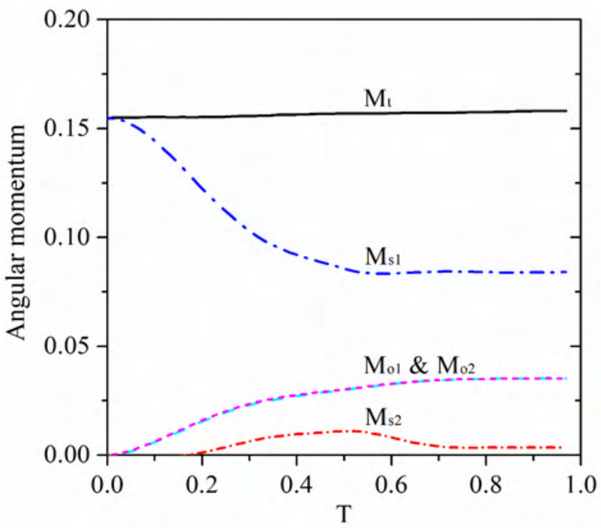

Figure 5.5 Interchange between orbital angular momentum (OAM), M_o, and spin angular momentum (SAM), M_s, for the head-on collision between a spinning droplet "D1" and a non-spinning droplet "D2" at $\omega = \omega_0$ and $\theta = 90^{\circ}$ as shown in Figure 5.4(c), in which TAM, M_t, refers to the total angular momentum and subscript "1" and "2" refer to droplet "D1" and "D2", respectively.

For case (c) with spinning droplet "D1" based on *y*-axis ($\theta = 90^{\circ}$), the axisymmetric deformation has been broken with the mass center connection line O_1O_2 deviated from *x*-axis, in which "D1" is stretched on the *x*-*z* plane, as shown in Figure 5.4(c). It is seen that the initial head-on collision between two spinning droplets can appear of the similar phenomena of the off-center droplet collision[21]. This is because the interchange between OAM and SAM, as shown in Figure 5.5. Specifically, the initial M_{s1} decreases and would be converted to a small amount of M_{s2} and prominent M_{o1} and M_{o2}. It indicates that the spinning droplet "D1" could slightly rotate the non-spinning droplet “D2” even by means of the head-on collision. The obtained M_{o1} and M_{o2} are equal because the zero linear momentum as specified should be maintained in the mass center coordinate system. Furthermore, the M_t during the entire process equals to the initial M_{s1}, which indicates the calculation of angular momentum in the present study is correct, where the slight increase of M_t is probably attributed to the numerical errors.

5.4.2 Energy budget

The entire collision process can be divided into three stages, namely impacting, bouncing, and oscillating stages, which has been defined in great details in[21]. In this section, the impacting and bouncing stages are mainly concerned because both cases show no apparent oscillating stage. The energy budget analysis is conduced based on each liquid droplet separately, denoted as “D1” and “D2”, as shown in Figure 5.6, in which the effects of ambient gas is insignificant to the droplet collision that has been studied in[21]. The initial total energy (TE) is defined as $E_{k0}^{\mathrm{trans}} + E_{k0}^{\mathrm{rot}} + \sigma S_0$, in which $E_{k0}^{\mathrm{trans}} = \pi We/24$ is the initial translational kinetic energy, $E_{k0}^{\mathrm{rot}} = 0.4E_{k0}^{\mathrm{trans}}$ is the initial rotational energy because $\omega = \omega_0$ in the present case, and $S_0 = 2\pi$ is the initial surface energy.

To facilitate the comparison of spinning effects on droplet collision, the head-on collision between two droplets without rotations that shown in Figure 5.6(a) has been included. However, the total energy (TE) and kinetic energy (KE) for D1 with $\omega = 0$ have been added a value of the initial rotational energy of $0.4E_{k0}^{\text{trans}}$ so that to let the TE lines for all cases collapse together. Furthermore, additional three cases with $\omega = \omega_0$ for three principle axes of $\theta = 30^{\circ}$, $\theta = 45^{\circ}$, and $\theta = 60^{\circ}$ are used to analyze the transition between the specific cases shown in Figure 5.6.

During droplet impacting stage, as shown in Figure 5.6(a), both the total increment of SE_1 and total decrement of KE_1 decrease monotonically whereas the total increment of TVDE_1 shows an increase, with increasing θ from 0 to 90 degree. It is seemingly contradicted to the previous understanding that the larger droplet deformation with more KE transferred to SE should invoke larger TVDE owing to the enhanced intensity of internal flow. This can be understood as that, for the droplet spinning with a small value of angle between the principle axis and the mass center connection line, the radial centrifugal force acts as a “spring effect” that promotes the interaction between KE and SE but would not cause larger velocity gradient accounting for the viscous dissipation. As shown in Figure 5.6(b), the total increment of SE_2 and total increment of TVDE_2 are consistently increase monotonically, whereas the KE_2 is however nearly uninfluenced, with increasing θ from 0 to 90 degree. During droplet bouncing stage, the droplets start to bounce back with a decrease in SE and an increase in KE. As shown in Figure 5.6(a), the evolution tendency has been reversed that SE₁ and KE₁ for $\theta = 90^{\circ}$ become maximum and minimum, respectively, among all cases, which is different from that in droplet impacting stage. As shown in Figure 5.6(b), the KE₂ for $\theta = 90^{\circ}$ is minimum while the SE₂ is uninfluenced, with increasing θ from 0 to 90 degree.

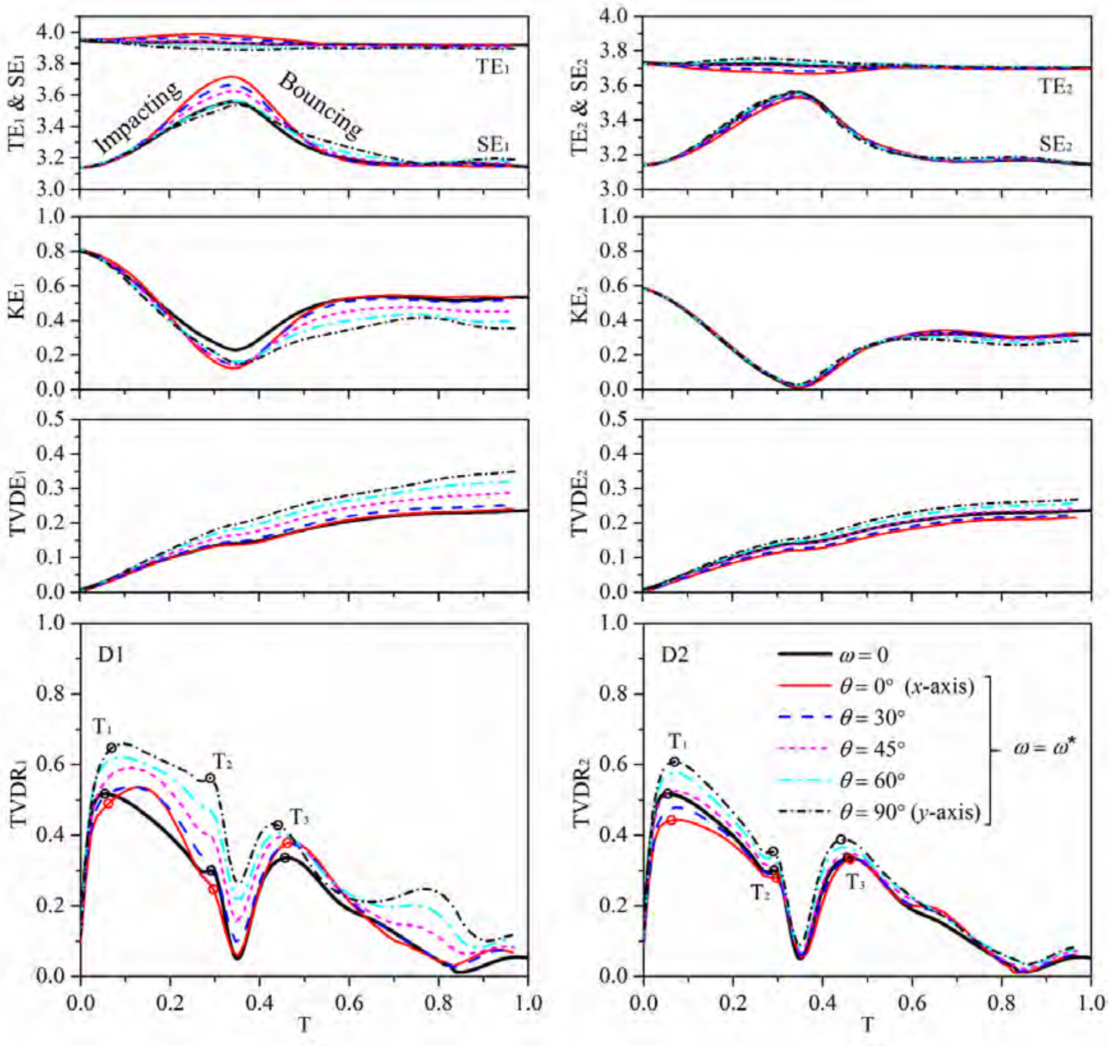

(a) (b)

Figure 5.6 Evolution of energy budget analysis for a spinning droplet of "D1" and a non-spinning droplet of "D2" for the representative case at $We = 9.3$ and $Oh = 2.8 \times 10^{-2}$. The total energy (TE), the surface energy (SE), the kinetic energy (KE), and the total viscous dissipation energy (TVDE) of the liquid droplets have been nondimensionalized, in which the subscripts "1" and "2" are for D1 and D2 respectively.

It is interesting to find that for the case with $\theta = 0^{\circ}$, the line of TVDE_1 is approximately collapsed on that line for D1 without rotations, whereas the line TVDE_2 is below that line for D2 without rotation. Consequently, the total TVDE = TVDE_1 + TVDE_2 for $\omega = \omega_0$ and $\theta = 0^{\circ}$ is smaller than that of $\omega = 0$, which indicates that the spinning effects of D1 do not always invoke the enhanced intensity of internal flow and thereby the enhanced viscous dissipation. Furthermore, although the total TE = TE_1 + TE_2 is conserved during the entire collision process, the separated TE_1 or TE_2 show that the energy is transferred from D2 to D1 with θ less than 45° while be reversed with θ larger than 45°. The total kinetic energy recovery for the head-on collision between spinning droplets shows a monotonically decrease with increasing θ from 0 to 90 degree, which can be explained by the monotonic increase of the viscous dissipation energy and the enhanced viscous dissipation rate (TVDR), as shown in Figure 5.6.

5.4.3 Total and local viscous dissipation rate

To further understand the viscous dissipation of the head-on collision between spinning droplets, the total viscous dissipation rate (TVDR) and the contours of local VDR at three chosen time instants corresponding to the three local maxima of TVDR are denoted as T_1, T_2, and T_3, are illustrated in Figure 5.6 and Figure 5.7.

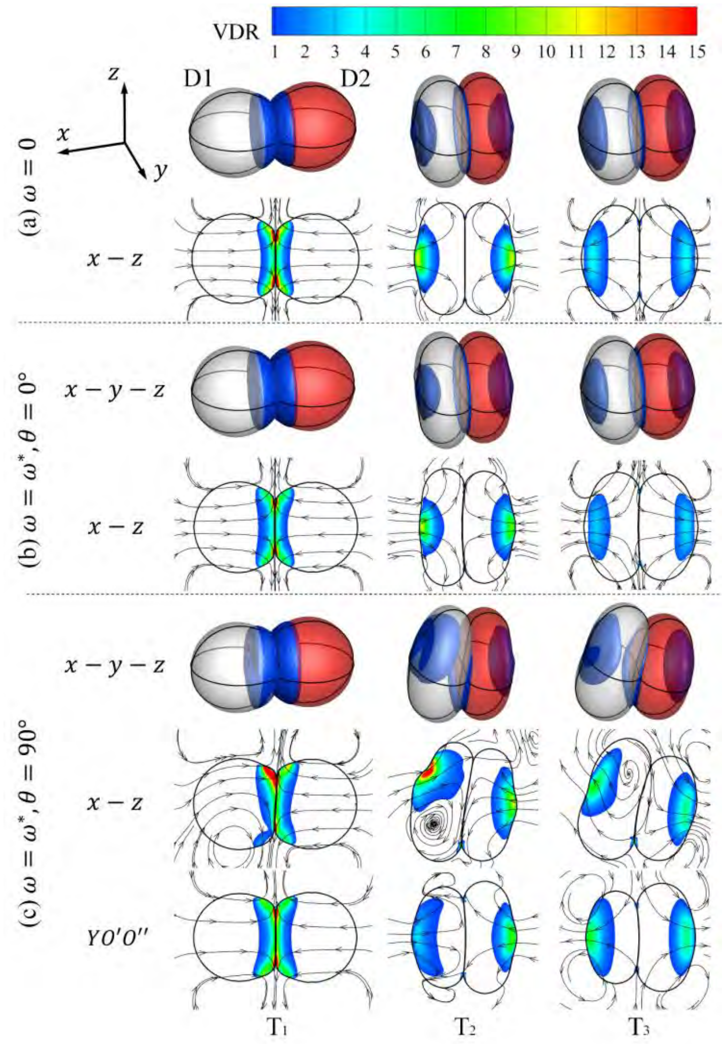

Figure 5.7 Comparison of the contour for the local viscous dissipation rate (VDR) at three chosen time instants, T_1, T_2, and T_3, shown in Figure 5.6. The contours have been blanked with a low threshold value of 0.5 for clear comparison of the VDR concentration.

Similar to the head-on collision between two identical droplets without initial spinning that discussed in previous work[21], as shown by the VDR contours at T_1 in Figure 5.7, the local VDR is mainly distributed around the droplet interaction region where the liquid is both expanded radially by the compression along the O_1O_2 direction and the rotating flow owing to droplet spinning, displaying a boundary layer-like internal flow. Although the local VDR for $\omega = 0$ in Figure 5.7(a) and

$\omega = \omega_0$ with $\theta = 0^{\circ}$ in Figure 5.7(b) show quite similar distributions, the counterintuitively reduced VDR for the collision between spinning droplets can be manifested by the relatively small area of VDR concentration. This can be further understood as that, the centrifugal force attributed by the spinning effects can overcome the viscous force to drive the boundary layer-like internal flow expanding radially during the droplet impacting stage, and thereby reduce the viscous dissipation because the TVDE in droplet impact stage contributes to the majority of the overall viscous dissipation. As shown in Figure 5.7(c), the either area or the concentration of local VDR for $\omega = \omega_0$ and $\theta = 90^{\circ}$ is enlarged by spinning effects during the entire collision process, which is attributed to the rotating flow interacting with the radical expansion flow.

In the present section of preliminary results, it focuses on the influences of the angle between the principle axis and mass center connection line on the collision between spinning droplets. Besides, the influences of the intensity of angular velocity and the initial shape upon the droplet collision. i.e. phase difference, are significant in the practical sprays involving large amount of binary collision between spinning droplets are attempted to be studied in the future work.

5.5 Helicity and vortex line

For the collision between two droplets, as discussed in the Background, the total angular momentum $\vec{J}$ is the sum of an orbital angular momentum $\vec{L}$ and a spinning angular momentum $\vec{S}$ by the self-rotation, in which

$$\vec{L} = \vec{r} \times \vec{p} \tag{5.4}$$

where $\vec{p}$ is the linear momentum along the translational movement of mass center and $\vec{r}$ is position vector of mass center. Thus, in particle physics[135], $\vec{S}$ can be described by the helicity that defined as the projection of the spin onto the direction of linear momentum $\vec{p}$.

Motivated by the helicity characterizing the spinning effects of particles, the definition of helicity in fluid mechanics can be introduced and defined as

$$H = \int \vec{u} \cdot \vec{\omega} dV \tag{5.5}$$

to describe the "non-orthogonality" of the velocity and vorticity vectors for droplet translational movement and spinning effects, respectively, where $\vec{u} = (u, v, w)$ is the velocity vector and $\vec{\omega}$ is the vorticity vector given by

$$\vec{\omega} = \nabla \times \vec{u} = \left(\frac{\partial w}{\partial y} - \frac{\partial v}{\partial z}, \frac{\partial u}{\partial z} - \frac{\partial w}{\partial x}, \frac{\partial v}{\partial x} - \frac{\partial u}{\partial y} \right). \tag{5.6}$$

Evidently, for the head-on collision between two dropelts without rotations, $\vec{u} \cdot \vec{\omega}$ remains zero everywhere in the flow field because the axisymmetric flow has only one vorticity component normal to the velocity plane.

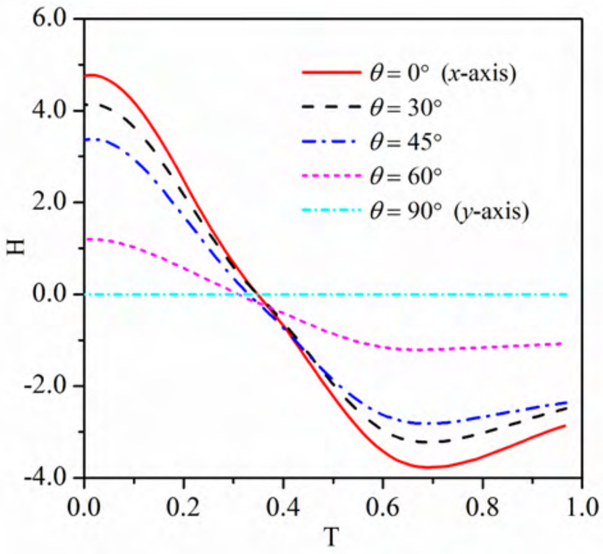

Figure 5.8 Evolution of helicity for the head-on collision between initially spinning droplets.

While for the head-on collision between two spinning dropelts concerned in the present study, the "non-orthogonality" of the velocity and vorticity vectors has been broken, as the helicity shown in Figure 5.8. With increasing θ, the amplitude of helicity decreases monotonically and finally vanish at $\theta = 90^{\circ}$. The zero integral helicity denotes the droplet spin is always perpendicular to the plane that the droplets mass center trajectory lies, in which the plane must be a symmetry (*x*-*z*) plane[21]. That is because the velocity components and the velocity derivatives are reversed on the both sides of the *x*-*z* plane, expressed as $v_+ = -(v_-)$ and $(\partial/\partial y)_+ = -(\partial/\partial y)_-$ where the positive and negative symbol denote two sides of *x*-*z* plane, respectively. Thus, we have

$$(\vec{u}_- \cdot \vec{\omega}_-) = (u, -v, w) \cdot \left(-\frac{\partial w}{\partial y} + \frac{\partial v}{\partial z}, \frac{\partial u}{\partial z} - \frac{\partial w}{\partial x}, -\frac{\partial v}{\partial x} + \frac{\partial u}{\partial y}\right) = -(\vec{u}_+ \cdot \vec{\omega}_+) \quad (5.7)$$

and $H = H_+ + H_- = 0$ for the entire droplets. The integral helicity describing droplet spinning can be either positive or negative, which is attributed to the change of velocity vectors during droplet impacting and bouncing stage but not the significant change of droplet spinning direction.

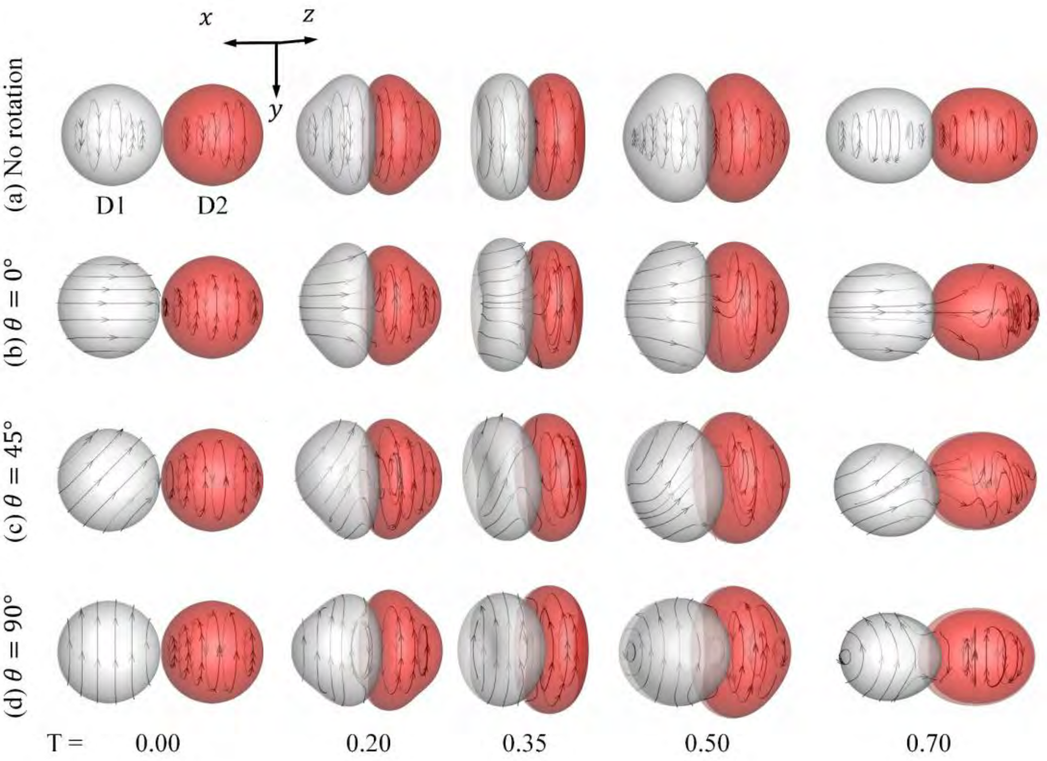

Figure 5.9 Evolution of vortex lines for the head-on collision between initially spinning droplets.

Figure 5.9 shows a qualitative comparison of vortex lines of the head-on collision between droplets with or without spinning effects. It is seen that the vortex lines for the head-on collision between two rotation-free droplets are a series of concentric circles, as shown in Figure 5.9(a), which are centered along the line connecting the mass centers of the droplets, indicating that the flow is purely axisymmetric, and the vortices are in the ring shape. These ring-shaped vortices should be attributed to the shear flow formed by compression in the axial direction and expansion in the radial direction. While for the head-on collision between one spinning droplet and one rotation-free droplet, it presents the interaction between “line-shaped” vortex lines and “ring-shaped” vortex lines. The axisymmetric flow is influenced by the initial droplet rotation, except for a specific case of the “line-shaped” vortex lines are perpendicular to “ring-shaped” vortex lines, as shown in Figure 5.9(b). The internal flow in Figure 5.9(c) becomes chaos and the symmetry plane in Figure 5.9(d) can be still observed. Their interactions are reflected by the strong linkage or knotedness of the vortical strucutres, which translates into strong helicity in the current context. We can further observe that both ends of a “line-shaped” vortex line stem from the droplet surface. This can be explained by that, in a finite vorticity field, a vortex filament must either form a closed vortex ring or terminate on the fluid boundaries where the flux of vorticity is not zero[136].

Regardless of the specific cases of the head-on collision considered in the present study, it is noted that the helicity can also be conserved to zero for the previous work[21] of off-center collision with a symmetry plane. It indicates that the lines for the relative velocity direction before and after droplet collision, and the mass center connection line are always located on a same plane with the presence of symmetry flow, which is important to the modelling simplification of binary droplet collision into the collision between two mass points by ignoring the droplet spinning effects.

5.6 Concluding remarks

The head-on collision between one spinning droplet and one rotation free droplet is numerically investigated in the present study. The numerical method has been validated by the previous work[21], and the simulation of droplet deformation and instability analysis of a single spinning droplet in the present study, which successfully traces the two-lobed and four-lobed shapes with increasing the spinning angular velocity.

The phenomenological description and energy budget present the viscous dissipation and energy transfer for each droplet, showing that the total kinetic energy recovery for the head-on collision between spinning droplets decrease monotonically with increasing θ from 0 to 90 degree, which can be explained by the monotonic increase of the viscous dissipation energy and the enhanced viscous dissipation rate (TVDR).

In the modelling of binary droplet collision, the orbital angular momentum $\vec{L}$ and the spinning angular momentum $\vec{S}$ are under mutual transformation during the droplet collision although the total angular momentum is conserved. The zero helicity indicates that the translational and spinning movement of droplets are always orthogonal before and after droplet collision, which is the key assumption of the modeling simplification of binary droplet collision into the collision between two mass points by ignoring the droplet spinning effects.

Furthermore, the influences of other parameters such as the size disparity, impact parameter, chirality of colliding droplets, the initial droplet shape relevant to the phase difference before the collision, and the intensity of spinning are excluded deliberately from the preliminary study, however they are of significance in the real sprays and merited the further investigations.

6 Mass intermínglement and hypergolic ignition of TMEDA and WFNA droplets by off-center collision

6.1 Background and objectives

Hypergolic propellants have received lasting attentions in the past decades for their applications in rocket propulsion, in which the spontaneous ignition occurs upon their contact without an external source of energy[80, 132, 137, 138]. Unlike the auto-ignition of a homogeneous gaseous mixture of non-hypergolic reactants, hypergolic ignition is intrinsically heterogeneous as it involves mixing and reaction of initially separated propellants in both liquid phase and gas phase[138-140].

The previous studies have observed that the ignition delay time (IDT) is closely related to the initial contact and subsequent liquid-phase mass intermínglement between hypergolic fuel and oxidizer droplets. Recently, Zhang *et al.*[80] experimentally studied the head-on collision between binary droplets of N,N,N',N'-tetramethylethylenediamine (referred to as TMEDA hereinafter) and white fuming nitric acid (referred to as WFNA hereinafter) in atmospheric environment. The most notable experimental discovery in the study is the non-monotonic variation of hypergolic IDT with increasing We. The underlying physics is the non-monotonic emergence of a "jet-like" internal mixing within the coalesced droplet with increasing

We, a fluid dynamical phenomenon that was recently identified by Tang *et al.*[15] in unequal-size droplet collision. The "jet-like" internal mixing facilitates the exothermic liquid-phase reaction, TMEDA + $2HNO_3$ → TMEDADN, whose heat release is crucial to the subsequent droplet heating and vaporization, the decomposition of the propellants, and eventually the gas-phase ignition[139].

In spite of the above findings about the hypergolic ignition by the head-on collision of TMEDA and WFNA droplets, it should be recognized that the head-on collision is a rare event and that the off-center collision occurs frequently in reality. However, hypergolic ignition by off-center droplet collisions has not been sufficiently studied, probably because the characterization and quantification of its intrinsically three-dimensional nature is challenging for both experiment and simulation.

In the early experimental study of Ashgriz and Poo[14], the inter-droplet mass exchange was observed after the stretching separation of off-center collisions. Inamuro *et al.*[141] used the lattice Boltzmann method (LBM) to numerically find the non-monotonical internal mixing with B for the off-center collision between droplets of equal size, in which the mixing rate was defined as the percentage of the number of particles of a color in the total number of particles in a droplet, and the maximum mixing rate is about 30% at about $B = 0.2$. Sun *et al.*[142] numerically studied the off-center collision of two identical droplets by using the moving particle semi-implicit method. Although their results show significant discrepancies compared with the previous experiments on collision outcomes, the non-monotonic variation of the mixing rate with B was observed at $We = 1.5$. A similar result was also obtained in the Volume-of-Fluid (VOF) simulation of Chen *et al.*[104] on the energy and mass transfer between two equal-size droplets with We being up to 70. Particularly, they found that the maximum mass transfer rate appears at about $B = 0.3 \sim 0.4$, being consistent with Inamuro *et al.*'s[141] results.

Motivated by the previous understanding of non-monotonic droplet mixing with varying B and its correlation with the hypergolic IDT, in the present work, we attempt to verify the internal-mixing-induced non-monotonical hypergolic IDT with varying B for the off-center collision between TMEDA and WFNA droplets of unequal sizes by conducting both experimental and numerical studies. The experimental part was conducted by my cooperator, Dr. Zhang, to whom I am very grateful, and the details can be find in[132]. The numerical simulation based on VOF method was mainly focused on the off-center collision of non-reacting droplets, with emphasis on investigating the influence of B on droplet mixing.

Based on the above considerations, we present the present study as follows. The numerical methods and experimental validations are described in Section 6.2, followed by the numerical interpretation on the mixing enhancement by slightly off-center droplet collision in Section 6.3. Finally, the correlation between the quantitative mixing index and the IDT is presented in Section 6.4.

6.2 Numerical methods and experimental validations

6.2.1 Problem definition and simplification

It should be noted that we had no an ambition to simulate the extremely complex and tangled physicochemical processes of hypergolic ignition of TMEDA and WFNA droplets, including the fluid-dynamical processes of droplet collision and mixing, the transport processes of mass diffusion and droplet heating, the phase change process of droplet vaporization, and the chemical processes in liquid and gas phases. The present VOF simulation, which has been sufficiently validated against available experiments in literature, is able to provide useful information about the early stage of droplet interaction, when the physical transport, phase change and chemical reactions have not fully emerged yet.

Table 6.1 Physical properties of various liquids

Liquids	Surface tension, σ (10^{-2} N·m^{-1})	Viscosity, μ (10^{-3} N·s·m^{-2})	Density, ρ (10^{3} kg·m^{-3})
TMEDA	2.65	0.90	0.78
WFNA	5.86	0.89	1.50
Water	7.29	1.00	1.00

The physical properties of the liquid propellants are given in Table 6.1 in comparison with those of water. Several assumptions and simplifications were made in the simulation and are expatiated as follows.

First, the liquid-phase and gas-phase reactions, the droplet heating, and the droplet vaporization are negligible in the early stage. This is because the early stage lasts for about a few milliseconds and is significantly shorter than the hypergolic IDT, which is typical of some tens of milliseconds. As a result, the present simulation problem can be first simplified as the off-center collision of two unlike droplets, where the flows in both liquid- and gas-phases are incompressible, non-reactive, and isothermal. The flow incompressibility for liquid-phase droplets is self-evident. The gas-phase flow due to vaporization (Stefan's flow), the heat and mass transport, and the flame propagation are sufficiently slow so that the compressibility effect is negligible. Dimension analysis indicates that a physical quantity of interest, denoted by $\tilde{Q}$, depends on nine non-dimensional parameters as

$$\tilde{Q} = f\left(We, B, \Delta, Oh, \frac{\rho_S}{\rho_L}, \frac{\mu_S}{\mu_L}, \frac{\sigma_S}{\sigma_L}, \frac{\rho_g}{\rho_L}, \frac{\mu_g}{\mu_L}\right) \tag{6.1}$$

Second, the effects of the density difference and the viscosity difference between the droplets can be neglected. Because the Peclet number, $Pe = UD_L/\alpha$, is as large as $O(10^6)$ in the present problem, the droplet mixing in the early stage is dominated by collision-induced flow convection in lieu of the liquid-phase mass diffusion. It is also noted that TMEDA and WFNA has very similar viscosity so that $\mu_S/\mu_L \approx 1$.

Third, the droplet mixing induced by the surface tension variation, also known as the Marangoni effect, can be neglected. This is because the capillary pressure driven by the surface tension difference, $|\sigma_S - \sigma_L|/D_L$, is substantially smaller than the droplet dynamic pressure, $\rho_L U^2$. The ratio of these two pressures yields

$$\frac{|\sigma_S - \sigma_L|/D_L}{\rho_L U^2} \sim \frac{|\sigma_S/\sigma_L - 1|}{We} \sim O(10^{-2}) \tag{6.2}$$

Finally, $\rho_g/\rho_L \sim O(10^{-3})$, $\mu_g/\mu_L \sim O(10^{-2})$, and $Oh = 2.5 \times 10^{-3}$ are fixed in the present problem because we considered the collisions between TMEDA droplets of varying diameters with WFNA droplets of a fixed diameter of 1.45mm in atmospheric air. Previous studies[15, 20, 22, 23, 104] have proved that the small gas-liquid density and viscosity ratios have negligible influence on the droplet internal flow.

With the above simplifications and assumptions, the present simulation problem is further simplified as the off-center collision of two droplets of the same liquid, leading to only three controlling non-dimensional parameters, namely, We, Δ and B. The simulation results are the same for any fluids as long as their physicochemical properties satisfy the above approximations and they have the same set of the non-dimensional parameters. As will be proved in the following section, the simulation can produce qualitative description to the droplet deformation and mass intermingglement, which helps understand the experimental observations.

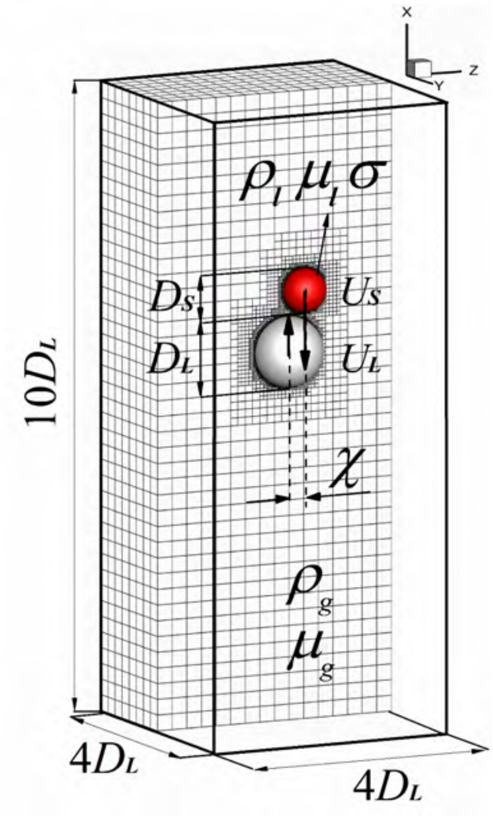

Figure 6.1 Schematic of the three-dimensional computational domain and the adaptive mesh for the VOF simulation.

6.2.2 Numerical specifications

The schematic of the three-dimensional computational domain and the adaptive mesh for the present VOF simulation are shown in Figure 6.1. The domain is $10D_L$ in height and $4D_L$ in both width and depth. The density and viscosity are ρ_l and μ_l for the liquid, and ρ_g and μ_g for the gas, respectively. The surface tension coefficient of the gas-liquid surface is denoted by σ. The two droplets colliding along the x-direction have zero velocity components in the y- and z-directions. Their velocity components in the x-direction are $U_S = -\Delta^3 U/(1+\Delta^3)$ and $U_L = U/(1+\Delta^3)$ so that the relative velocity is U and the momentum of the entire collision system remains zero. The natural oscillation time of the large droplet is $t_{\mathrm{osc}} = \sqrt{\rho_L D_L^3/\sigma_L}$, by which the non-dimensional time can be defined as $\mathrm{T} = t/t_{\mathrm{osc}}$. The outflow boundary conditions are specified on all the boundaries.

The conventional VOF method with one marker function[18, 19] was applied in the present study, which has been discussed in great detail in Chapter 3. To resolve both the droplet interface and the droplet internal flow, the computational domain is divided into three physical zones, such as the gas, the droplet interior, and the droplet interface. Each zone has its own mesh refinement level R, and the minimum mesh size in each zone is of $O(2^{-N})$. Accordingly, we can use (N_g, N_d, N_i) to describe the refinement levels in corresponding physical zones. A typical simulation run with the mesh refinement (5, 6, 7) results in maximally 5957272 grid points, which is equivalent to about 3.35×10^8 grid points on a uniform mesh and takes about 86 hours of real time for a computational time of $\mathrm{T} = 2.0$ on two Intel Xeon E5-2692 processors with 48 cores on Tianhe-2 supercomputer.

6.2.3 Experimental validations

To validate the present numerical methods for head-on collision ($B = 0$), the coalescence and reflexive separation of two water droplets of unequal sizes were simulated and compared with Ashgriz and Poo's experiment[14], as shown in Figure 6.2. It is noted that the Weber number and Ohnesorge number reported in the experiment are defined based on the smaller droplet and have been converted to on the present definitions as $We = 112$ and $\Delta = 2.0$. Tanguy and Berlemont[84] simulated the experiment by using the Level-set method and based on an estimated $D_S = 400\ \mu m$, leading to $Oh = 4.15 \times 10^{-3}$. However, we could not reproduce the experimental images by using their parameters. After reanalyzing the experimental images, as shown in Figure 6.2(a), we found that the exact size ratio is $\Delta = 1.82$ and using $We = 102$ and $Oh = 5.10 \times 10^{-3}$ enabled us to quantitatively reproduce all the collision characteristics. More details about the analysis of the experimental images are given in Supplementary Material of [132].

To examine the grid-dependence of the present simulation, we used three sets of mesh refinement levels, such as (5, 6, 7), (5, 6, 8) and (5, 7, 8), which result in maximally 5719053, 6712558 and 6874396 grid points, respectively. As shown in Figure 6.2, these meshes produce almost the same results compared with the experimental images in terms of droplet deformation, internal mixing pattern, and stretching separation. As a balance of computational cost and accuracy, the intermediate level of (5, 6, 8) were used to reproduce all the simulation results in the following sections.

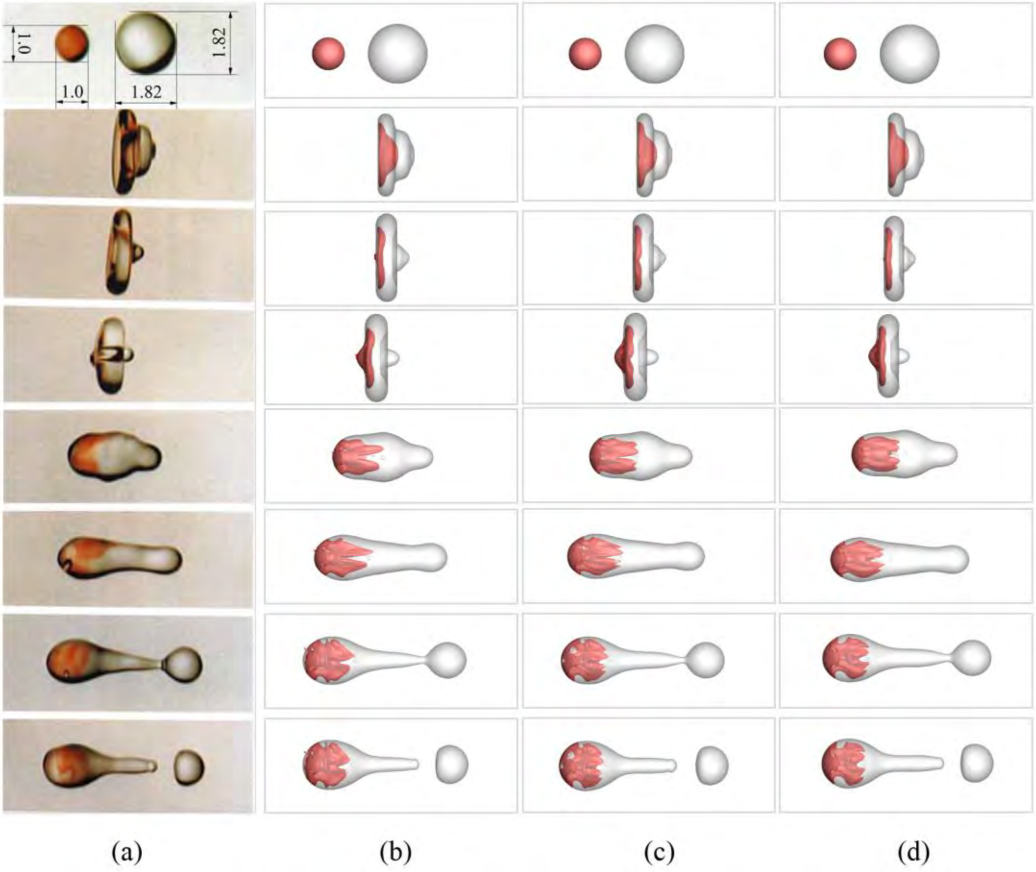

Figure 6.2 Experimental validation and grid independence analysis of the head-on collision ($B = 0$) of unequal-size water droplets at $We = 102, \varDelta = 1.82$ and $Oh = 5.10 \times 10^{-3}$[14]. (a) Ashgriz and Poo’s experiment[14], and three sets of mesh refinement levels with (b) (5, 6, 7), (c) (5, 6, 8) and (d) (5, 7, 8), respectively。

To further validate the present numerical methods for off-center collisions, the coalescence and stretching separation of two identical water droplets[14] with $We = 90, \varDelta = 1.0$ and $Oh = 6.89 \times 10^{-3}$ were simulated and shown in Figure 6.3. Again, the simulation satisfactorily reproduces the complex three-dimensional droplet deformation and accurately predicts the number of satellite droplets after stretching separation. It is noted that we could not reproduce the experimental results by using $We = 83$ reported in Ref.[14], which might not be accurate due to the uncertainty of droplet sizes in the early experimental measurement. The uncertainty of the Weber numbers is 8%, which is about the same as that of the measured size ratio.

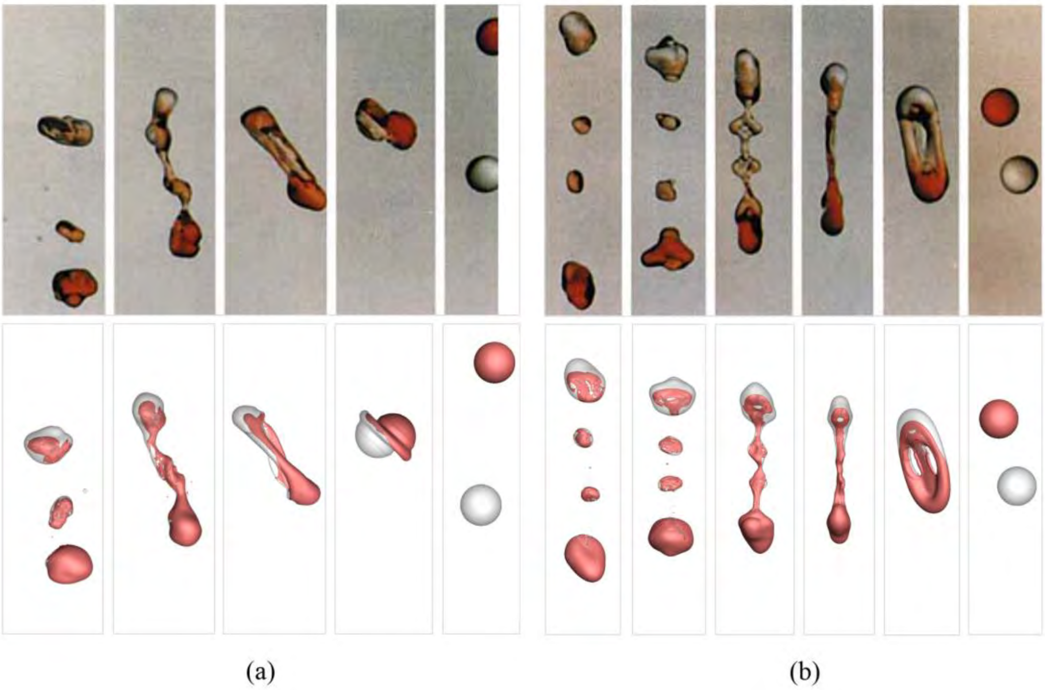

Figure 6.3 Experimental validation of the off-center collision of identical water droplets with (a) one satellite droplet at $We = 90$ and $B = 0.34$ and (b) two satellite droplets at $We = 90$ and $B = 0.43$[14].

6.3 Interpretation on the mixing enhancement by slightly off-center droplet collision

Phenomenological description and quantitative grayscale levels analysis on the experimental shadowgraph images of the hypergolic ignition for a representative case of $We = 60.9, \Delta = 1.6$ at $B = 0.0$ and $B = 0.3$ have been presented in [80, 132]. Based on the shadowgraph images, the entire collision process can be divided into five distinct stages, namely Stage I: droplet coalescence and deformation; Stage II: droplet heating and vaporization; Stage III: rapid vaporization and reactions; Stage IV: ignition in gas phase and flame propagation; Stage V: combustion and flame extinction. As expatiated in the previous study[80, 132], the analysis of the grayscale levels of the shadowgraph images can be used to systematically determine the IDT with reduced uncertainty. Overall, compared with the head-on collision, the slightly off-center collision results in faster droplet heating and vaporization, and thereby leading to a shorter IDT. It was hypothesized that this is caused by the enhanced internal mixing by droplet stretching.

Figure 6.4 shows three sets of experimental shadowgraph images and simulation results that were selected and compared at three representative moments, indicated by "R" for $B = 0.3$ and "S" for $B = 0.0$. The column (a) is the experimental images amplified for a clearer illustration, in which the droplet surface contours (on the *x-z* plane) are delineated in red. The columns (b)-(d) are the corresponding simulation results viewed from three different directions, where the red denotes the fluid mass from the TMEDA droplet and the gray the WFNA droplet. The column (e) shows pressure contours and streamlines on the slices cut by the *x-z* plane. It is reemphasized that the impact velocity is along the *x*-direction and the droplets deviate from head-on situation in the *z*-direction, thus the *x*-*z* plane is the symmetric plane of the collision system.

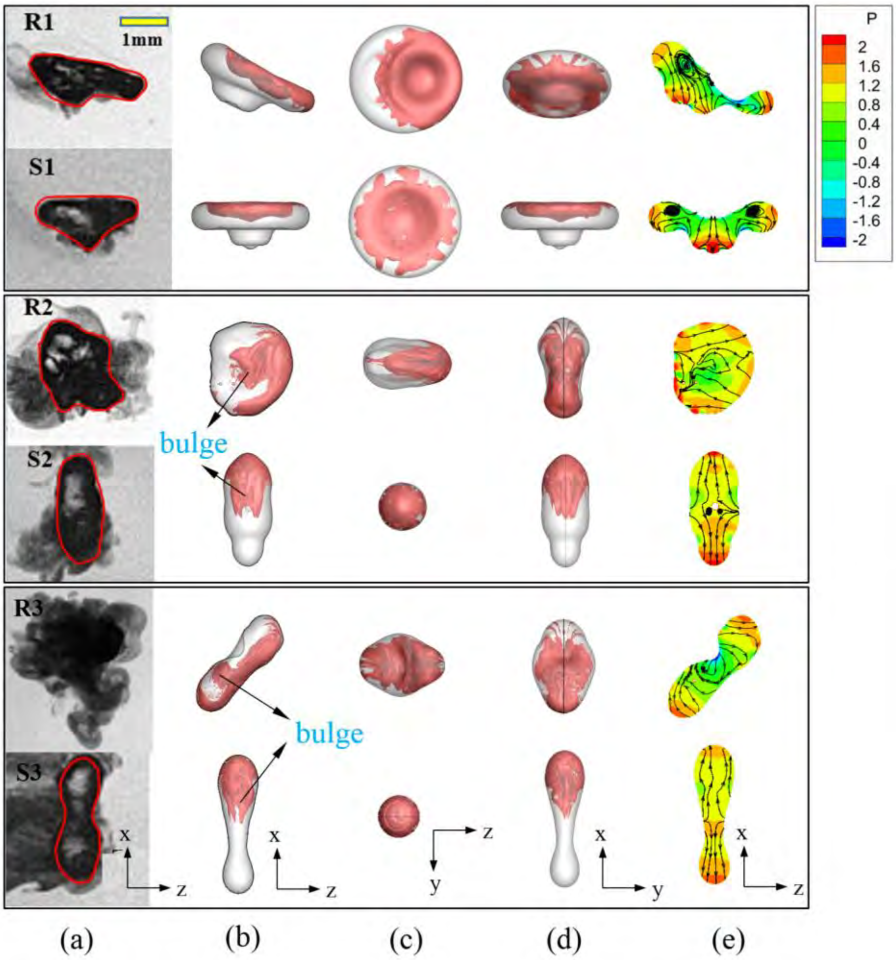

Figure 6.4 Comparison between $B = 0.3$ (denoted by "R") and $B = 0.0$ (denoted by "S") for three representative moments: (a) the experimental shadowgraph images, (b)-(d) the simulation results viewed from three different directions, and (e) the pressure contours and streamlines. The experimental times are 2.4ms, 7.0ms, and 13ms, respectively; the computational time T are 0.25, 0.57, and 0.84, respectively, corresponding to the physical times ($t = \mathrm{T} * t_{\mathrm{osc}}$) that are 2.2ms, 5.0ms, and 7.4ms, respectively. $t_{\mathrm{osc}} = 8.83$ ms.

The first representative instant, indicated as “R1” for $B = 0.3$ and “S1” for $B = 0.0$, was selected from their corresponding Stage I. The agreement between the experimental time (2.4 ms) and the computational time (2.2 ms) are very good, substantiating the quantitative prediction of the present simulation on droplet collision dynamics. The slightly off-center collision causes the merged droplet to rotate and stretch so that the droplet resembles an asymmetric “spoon”, while the head-on collision results in an axisymmetric saucer-like droplet shape. The enhanced stretching effects around the contact surface of two droplets can be further verified by the streamline in Figure 6.4(e).

The second representative instant, indicated as “R2” for $B = 0.3$ and “S2” for $B = 0.0$, was selected from their corresponding Stage II. There is a slight discrepancy between the experimental time (7.0 ms) and the computational time (5.0 ms). This is because Stage II involves droplet heating and slight vaporization, the increased droplet surface temperature reduces the surface tension and hence prolongs the droplet oscillation time, $t_{\mathrm{osc}} = \sqrt{\rho_L D_L^3/\sigma_L}$, which is fixed in the present simulation. The direct observation indicates that the mass interminglement at “R2” seems stronger than that at “S2”, because mass is spread out close to the droplet surface in addition to the bulge-like internal mixing pattern emerged in both cases.

The third representative instant “R3” for $B = 0.3$ was selected form Stage III, while “S3” for $B = 0.0$ was still in Stage II. There is a moderate discrepancy between the experimental time (13.0 ms) and the computational time (7.4 ms) because the droplet is affected by rapid liquid-phase reactions and vaporizations. Considering the mass interminglement during Stage I and Stage II is the controlling mechanism responsible for the non-monotonic ignition delays, the discrepancy does not affect the present conclusions. It is noted that the merged droplet has been completely concealed by the opaque vapor at “R3” while it can be seen at “S3”. The bulge-like internal mixing pattern can still be seen clearly in both cases. For the slightly off-center collision at $B = 0.3$, the evidently intense interminglement of the liquid mass within the merged droplet could lead to a more uniform droplet vaporization. For the head-on collision at $B = 0.0$, as indicated by the streamlines shown in Figure 6.4(e), the separation tendency could suppress the mass interminglement between two droplets.

To facilitate the recognition in the first place of the correlation between the mass interminglement and the hypergolic ignition, we calculated the temporal area changes of the colored contact surface of the droplets. The contact surface area $A(t)$ of the droplets is normalized by the initial surface area A_0 of the droplets. Because the mesh resolutions on the gas-liquid interface and inside the droplet are the same in the present simulation setup, the normalized colored contact surface area $A(t)/A_0$ can be approximately calculated by

$$\frac{A(t)}{A_0} = \frac{N[0 < \phi(t) < 1]H[f(t) - 1]}{N[0 < f(0) < 1]} \tag{6.3}$$

where N is the number of the meshes in which the VOF function $f(t)$ or the mass dye (color) function $\phi(t)$ take certain values, and thus it can be treated as functionals of $f(t)$ or $\phi(t)$. The VOF function $f(t) = 1$ denotes the droplet interior, $0 < f(t) < 1$ the gas-liquid interface, and $f(t) = 0$ the gas; the color function $\phi(t) = 1$ denotes the smaller droplet interior, $0 < \phi(t) < 1$ the contact surface of the droplets, and $\phi(t) = 0$ the larger droplet interior. In the above expression, the Heaviside step function ensures only those meshes within the droplet interior to be counted for calculating the colored contact surface. The results show that the evolutions of $A(t)/A_0$ for $B = 0.3$ is faster than that of $B = 0.0$, indicating the mass interminglement for slightly off-center droplet collision is indeed enhanced and critical to the hypergolic ignition.

6.4 Correlation between mass interminglement and ignition delay time

Based on the experimental observation of a non-monotonic variation of IDT with varying impact parameter[132] and the numerical interpretation of the mixing enhancement by slightly off-center collision in Section 6.3, a qualitative correlation can be obtained between the varying degree of mass interminglement and the IDT. As can be further seen in Figure 6.5(a), the VOF simulations for five cases at fixed $We = 60.9$ and $\Delta = 1.6$ but varying B from 0.0 to 0.9, supplement the experimental shadowgraph images by providing useful information about the internal flow and mass interminglement of droplet. It is clearly seen that, the droplet mass is increasingly intermingled with increasing B from 0.0 to 0.3, where the droplet remains coalesced. This enhanced mass interminglement can be attributed to the better droplet mixing and the shorter IDT at $B = 0.3$. Further increasing B to 0.6 and higher values, the droplet stretching deformation becomes more intense but the coalesced droplet eventually separates into two major masses with a certain number of satellite droplets. Although the enhanced mass interminglement facilitate droplet mixing and hence liquid-phase reactions, the amount of mass participating in the reactions is however reduced due to the droplet separation. This explains the elongation of IDT at $B = 0.6$ compared with that at $B = 0.3$, and the non-ignitability of the system at $B = 0.9$.

For a quantitative correlation between the IDTs and the mass intermingl ement, a time-dependent “mixing index”[15, 143], $M \in [0,1]$, whose variants have been proposed and used in previous studies[15, 23], was adopted by the present study. The index can be defined by

$$M = 1 - \frac{\int_V |C - C_\infty| \, H(f - 1) \mathrm{d}V}{\int_V |C_0 - C_\infty| \, H(f - 1) \mathrm{d}V} \tag{6.4}$$

where f is the spatially and temporally VOF function with $f = 1$ in droplet interior, $f = 0$ in gas, and $0 < f < 1$ on the droplet interface; $H(f-1)$ is the Heaviside step function restraining the volumetric integrations within the droplets. C is the spatially and temporally varying "concentration" function measuring the degree of "mixing", or more rigorously, mass interminglement. C_0 and C_∞ are the "concentrations" defined in the initially unmixed droplets and for an ideal situation of "well-mixing", respectively. These "concentration" functions are defined by

$$C_0 = \begin{cases} 0, & \phi = 0 \\ 1, & \phi > 0 \end{cases}, C_\infty = 1/(1+\Delta^3), C = \frac{|\phi - 0.5|}{0.5} C_0 \tag{6.5}$$

where ϕ is the mass dye function with $\phi = 1$ in the smaller droplet, as seen by the red dye in Figure 6.5(a), and $\phi = 0$ otherwise.

The "mixing indices" for the five cases of Figure 6.5(a) are shown in Figure 6.5(b) for comparison. It is seen that M for $B = 0.3$ is larger than that for $B = 0.0$ during almost the entire collision process except in the early stage between "R1" (or "S1") and "R2" (or "S2"), when the coalesced droplet has reached the maximum deformation and starts to contract under surface tension. This demonstrates that the mass interminglement and therefore the "droplet mixing" and liquid-phase reactions are indeed enhanced by slightly off-center collision at $B = 0.3$.

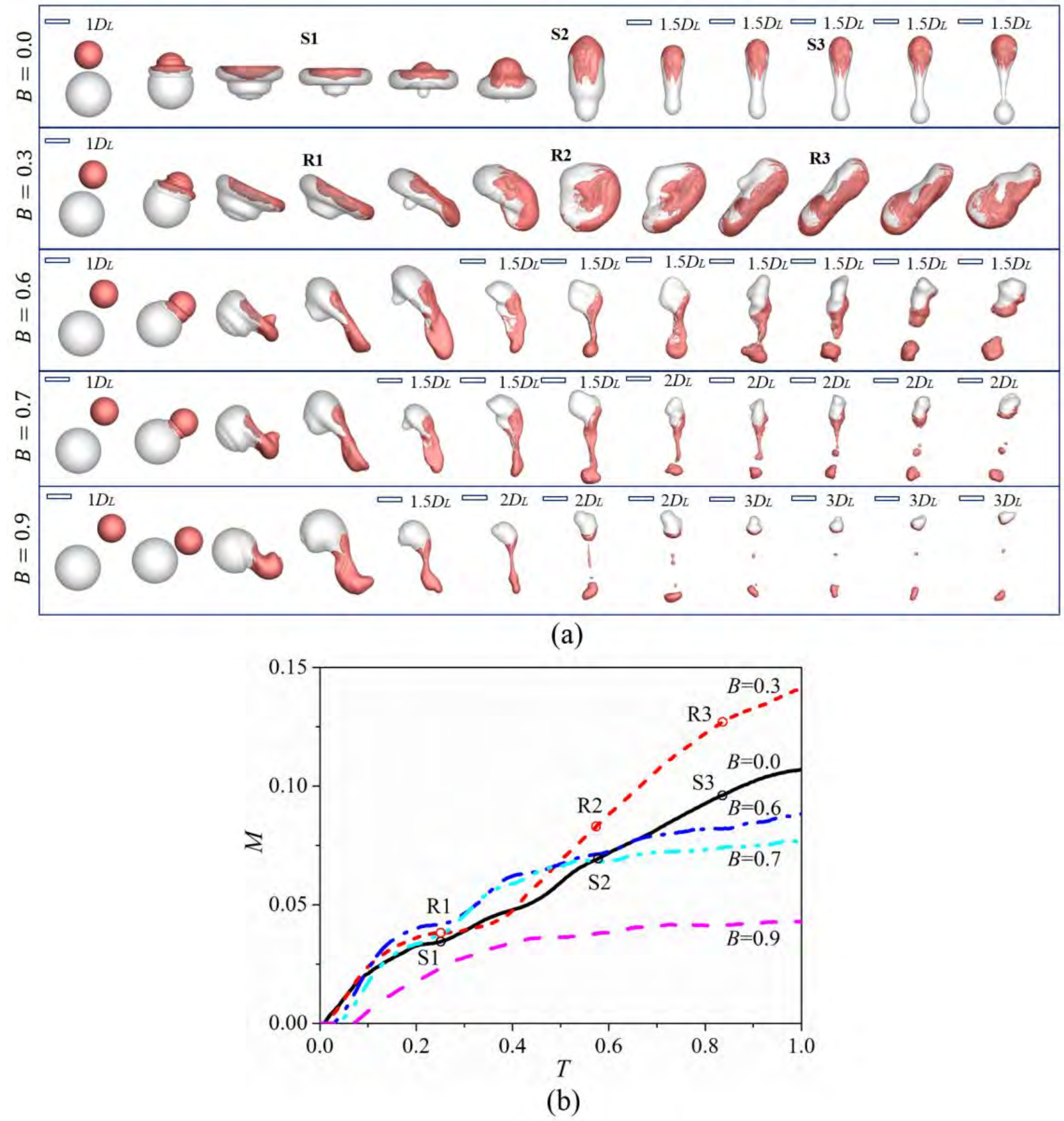

Figure 6.5 Variation of (a) droplet collision outcomes and (b) "mixing index" for various impact parameters with $B = 0.0, 0.3, 0.6, 0.7$ and 0.9 at $We = 60.9$ and $\varDelta = 1.6$.

For the moderately off-center droplet collision at $B = 0.6$, the rapid increase of M during the early stages attributes to the formed filament and satellite droplets, where mass interminglement is enhanced. However, the increase of M becomes slower in the later stages because of the occurrence of stretching separation suppresses the further mass interminglement, as seen in Figure 6.5(a) the large portion of the larger droplet remaining intact. Consequently, the IDT for $B = 0.6$ becomes larger than that for $B = 0.3$ because a smaller amount of liquid mass participates in the exothermic liquid-phase reactions and thereby the droplet requires a longer time to produce sufficient gas-phase species for ignition.

The additional case at $B = 0.7$ was added to show the transition to the nearly grazing droplet collision at $B = 0.9$. The “mixing index” for the case at $B = 0.7$ is almost the same with that for the case at $B = 0.6$ in the early stages, but it only slightly increases in the late stages, resulting evidently smaller M. As discussed above, the stretching separation occurs increasingly earlier with increasing B, and a decreasing amount of mass participates in the following interminglement and mixing. This trend is more notable for the case at $B = 0.9$, where M remains almost a small constant after the initial increase for a short period of time.

Although Figure 6.5 shows the correlation between the non-monotonic variations of M and IDT with increasing impact parameters, we noted some discrepancies between the experimental and simulation results about the droplet deformation, especially for the moderately off-center collisions at $B = 0.6$ and 0.7 involving filament separation. The underlying reason is that the local physical properties of the locally formed filament, such as viscosity and surface tension, might have been changed because of the chemical heat release from the liquid-phase reactions.

Although such a local variation of physical properties would not be significant for the whole droplet, but it can substantially change the subsequent fluid dynamics of the thin filament, particularly its separation tendency. Regardless of the deficiency of the present simulation in predicting the filament separation and the number of resulting satellite droplets, which is a challenging task even for non-reacting, isothermal droplet collision, the controlling physics of the mass interminglement is correctly captured by the simulation.

6.5 Concluding remarks

In the previous study on the hypergolic ignition of the head-on collision between a smaller TMEDA and a larger WFNA droplet at various Wes and Δs[80], the ignitability and IDT critically rely on the heat release from the liquid-phase reactions, which in turn is determined by the effective droplet internal mixing during earlier stages. The present study has extended our understanding from the rare event of head-on collision to more frequently seen off-center collision, as summarized in the following.

The impact parameter effects on IDT were first studied for a representative case at $We = 60.9, \Delta = 1.6$ and $Oh = 2.5 \times 10^{-3}$. Compared with the head-on collision, the IDT for the slightly off-center collision is shorter because of the promoted mass interminglement owing to the enhanced droplet stretching deformation, which is characterized by the formation of thin liquid filament. However, the filament tends to break up with increasing B, resulting in a smaller amount of liquid mass participating in the liquid-phase reactions, less vaporized gas-phase species, and prolonged ignition delay (for moderately off-center collision) or even non-ignitability (for nearly grazing collision).

The non-monotonic influences of B on the hypergolic ignition can be correlated with the non-monotonic effects of B on the mass interminglement of colliding droplets. Specifically, for slightly off-center collision, the droplet stretching leads to the more intense interminglement of the liquid mass within the merged droplet, which is computationally verified by evident mass spreading out close to the droplet surface in addition to the bulge-like internal mixing pattern. To further increase B, the substantial stretching effect results in stretching separation, which suppresses the mass interminglement between the droplets. Consequently, only portions of TMEDA and WFNA mass participate in the liquid-phase reactions, rendering less heat release and gas-phase species for ignition. The correlation between the mass interminglement and IDT has been quantitatively verified by examining the defined “mixing index”.

Although the present simulation captured the important physics of droplet mass interminglement that is crucial to the subsequent droplet behaviors, the simulation cannot capture the entire hypergolic ignition process due to the lack in heating and reactions. These absent physical effects should be accounted for in our future studies, including the transport phenomena and chemical reactions in the present VOF simulation.

7 Vortex-ring-induced internal mixing upon the coalescence of initially stationary droplets

7.1 Background and objectives

Droplet coalescence is a frequent event in many natural and industrial processes involving dispersed two-phase system[11, 12, 77]. The “internal mixing” after droplet coalescence has been paid increasingly attentions to understand its significance of fuel-oxidizer mixing in rocket engine systems and reactants mixing based on micro-droplet reactors in bioengineering[4, 5]. It is noted that the referred “internal mixing” hereinafter is not the physically mixing involving mass diffusion, but more accurately is the mass interminglement that represents the degree of contact between the liquid mass from initially small or large droplets.

Among previous droplet coalescence studies, a majority of the effort has been dedicated to the theoretical and experimental investigations of the evolution of the neck or bridge between two identical merging droplets, which is significant to the subsequent development of internal mixing. Because the internal mixing after coalescence is minimal for two identical droplets due to the intrinsic symmetry, it can be enhanced only by breaking the symmetry. Regardless of the symmetry breaking by such as the difference of surface tension[56] and viscosity, the most common method is the size disparity. Anilkumar *et al.*[44] experimentally observed a jet-like mixing after the coalescence between two initially stationary water–glycerin solution droplets of unequal sizes. For the highly viscous droplets, noticeable mixing was however not observed in their experiments, and instead, the smaller droplet simply lodges onto the larger droplet after coalescence.

To understand the internal mixing associated with the jet-like structure, Nobari and Tryggvason[144] employed the front-tracking method to simulate the coalescence between two stationary droplets. Their results suggest that the penetration depth of the fluid from the small drop monotonically changes with the size ratio in a very viscous drop where no internal jet forms, and that this monotonicity however does not hold for small viscosity drops where internal jet could appear. Later, Liu *et al.*[22] simulated the mixing of unequal-size droplets with emphasis on elucidating the important role of the surface energy of the merged interface in forming the jet-like mixing. They found that increasing the droplet viscosity suppresses the mixing and increasing the size disparity promotes the mixing. Recently, Tang *et al.*[15] experimentally investigated the coalescence between two unequal-sized droplets with nonzero Weber numbers and observed the non-monotonic emergence of the jet-like mixing with increasing We. The jet-like internal mixing was also reported in several other numerical studies employing the volume of fluid (VOF) method and the lattice

Boltzmann method[72, 73, 141]. Nevertheless, physical interpretation of the internal jet and its effect on mixing have not been adequately addressed in these studies.

Similar internal-mixing phenomenon has also been observed in the coalescence of a droplet into a liquid pool[130, 131]. A mechanism based on the generation of vorticity by accelerated flows at curved liquid free surfaces was proposed to explain the formation of the vortex ring. Specifically, in a homogeneous fluid without body force (or with conservative body force), which is the fluid in either the droplets or the ambient gas, the rate of change of vorticity, $\boldsymbol{\omega}$, associated with a fluid element is given by the vorticity transport equation (also known as the Helmholtz vorticity equation)[145],

$$\boldsymbol{D\omega}/\boldsymbol{D}t = \boldsymbol{\omega} \cdot \boldsymbol{\nabla u} + \nu \boldsymbol{\nabla}^2 \boldsymbol{\omega} \tag{7.1}$$

where $\boldsymbol{u}$ is the velocity and ν is the kinematic viscosity. The first term on the right-hand side of Equation (7.1) represents the stretching and tilting effect of the vortex-line, which is balanced by the change of vortex strength caused by the changes in the area and direction of the fluid element surface (p. 268-269 of Ref.[145]); the second term is the vorticity diffusion term, which by nature only causes the redistribution of vorticity in the presence of vorticity gradient. Equation (7.1) mathematically dictates that vorticity is only a transport quantity, meaning no vorticity can be created inside a homogeneous fluid. This interpretation, although elucidatetd by Batchelor[145] and Cresswell and Morton[130], has not been sufficiently recognized probably because of its non-intuitive differential form. Similar conclusion can also be deduced from an integral form of Equation (7.1), known as the Kelvin's circulation theorem[136] (or equivalently the Helmholtz's theorems[136]). Although the Kelvin's circulation theorem was originally derived for inviscid flows, Batchelor[145] extended it to viscous flows by deriving the total change of the circulation (Γ) around an arbitrary material contour in the form (Eq. 5.2.7 of Ref.[145]),

$$\frac{\mathrm{d}\Gamma}{\mathrm{d}t} = -\nu \oint (\boldsymbol{\nabla} \times \boldsymbol{\omega}) \cdot \mathrm{d}\boldsymbol{l} \tag{7.2}$$

where $\mathrm{d}\boldsymbol{l}$ is a material line element along the integration contour. Equation (7.2) can be viewed as the equivalent form of the Kelvin's circulation theorem for viscous flows. It clearly indicates that the vortex strength of any material volume does not change unless vorticity diffusion happens at the boundary by means of viscosity. Since diffusion is a transport phenomenon which does not introduce new quantity into the global system, vorticity must be generated at the boundaries where the homogeneous condition breaks or special boundary condition is in force. For inertialess drop coalescence with no initial vorticity and in the absence of rigid boundaries, the only source of vorticity must be the liquid–gas interface[130]. As the liquid–gas interface can be approximated by a free surface of a viscous fluid, the vanishing shear stress requires a nonzero jump in velocity gradients and therefore generates a finite vorticity[130, 146]. The vortex ring formation after coalescence is a synergic consequence of the vorticity generation on the liquid-gas interface, the vorticity transport (including accumulation and advection) to the droplet interior, and the vorticity diffusion within the droplet. To the knowledge of the authors, no attempts have been made to describe such a vorticity evolution for binary droplet coalescence.

In the present study, we aim to numerically investigate the coalescence of initially stationary droplets of unequal sizes. The first focus of the study is the jet-like internal mixing upon the droplet coalescence and its parametric dependence on liquid viscosity, surface tension and size differential. The second is to analyze the evolution of concomitant vorticity and its interrelation with the internal mixing. Regardless of the fact that droplet collision with increasing We may enhance the internal mixing, only initially stationary droplets (i.e. with a zero Weber number) was considered in the study based on the following considerations. First, the coalescence of initially stationary droplets can be treated as a leading order approximation to that with small We. More importantly, the coalescence of initially stationary droplets occurs at the contact point of two spherical droplets, which do not deform prior to coalescence[17]. At non-zero We, the complicated phenomena of draining the intervening gas film out of the gap between two colliding droplets[17] and the succeeding interface merging at the length scales of the van der Waals force pose great challenges to numerical simulation. The additional difficulty of dealing with droplet coalescence at non-zero Weber numbers will be avoided in the present study although it merits future studies.

The structure of the paper is organized as follows: the numerical specifications and validations are presented in Section 7.2, followed by the phenomenological description of the jet-like mixing for three representative liquids such as water, n-decane and n-tetradecane are discussed in Section 7.3. An analysis of vorticity evolution is presented in Section 7.4 to substantiate that the internal jet formation correlates with the vortex ring generated after droplet coalescence. The essential mechanism for internal jet formation is further elucidated through the quantitative analysis of the vorticity generation at the gas–liquid interface, and the subsequent formation, growth, and detachment of the main vortex ring. In Section 7.5, a vortex-ring-based Reynolds number, characterizing the strength of the detached main vortex ring relative to the viscosity, is proposed as the criterion for the internal jet formation. Finally, the internal mixing is quantified in Section 7.6 by using a mixing index, and the resultant mixing rates are compared among different cases to demonstrate the crucial impact of the internal jet on the mixing performance of the merged droplet.

7.2 Numerical specifications and validations

We consider two initially stationary droplets, i.e. $We = 0$ and $B = 0$, which are made to coalesce with each other at the point of contact at time $t = 0$, as illustrated in Figure 7.1. For the concerned problem that is intrinsic axisymmetric, a cylindrical coordinate is established so that the line connecting the mass centers of the two spherical droplets forms the axial (z-) direction. The computational domain is an axisymmetric cylinder of $7D_S$ in length and $3D_S$ in radius. Further extension of the domain has negligible influence on the results. The axisymmetric boundary condition ($\partial u/\partial r = 0, v = 0$) is enforced at the z-axis. At all the other boundaries, the flow is assumed to approach the condition in the far field, so the outflow boundary condition ($\partial \boldsymbol{u}/\partial n = 0, p = 0$) is specified. The diameters of the smaller and the larger droplets are D_S and D_L, respectively. The flows in both gas and liquid droplets are viscous and incompressible. The density and viscosity are ρ_l and μ_l for the liquid, and ρ_g and μ_g for the gas, respectively. The surface tension coefficient of the gas–liquid surface is σ. The tangential and normal directions in a local coordinate system established on the droplet interface are denoted by $\hat{t}$ and $\hat{n}$, respectively.

Under the conditions that concern the present study, the gas–liquid density ratio ρ_g/ρ_l is of $O(10^{-3})$ and gas-liquid viscosity ratio μ_g/μ_l is of $O(10^{-2})$ so that they are assumed to have insignificant influence on the problem, as substantiated in the previous studies[15, 20, 22, 104]. Consequently, only Oh and $\varDelta$ are considered in the present study, in which Oh is in the range of 8.3×10^{-3}~3.6×10^{-2} and $\varDelta$ varies from 1.0 to 3.2, which are similar to those considered in the experiments of Zhang *et al.*[46]. The characteristic time is $t_c = \sqrt{\rho_l D_S^3/\sigma}$, which is slightly larger than the natural oscillation time of the smaller droplet, $(\pi/4)\sqrt{\rho_l D_S^3/\sigma}$. Based on these characteristic physical quantities, the Reynolds number can be defined as $Re = \sqrt{\rho_l \sigma D_S}/\mu_l$, which is the reciprocal of Oh. Thus, Re is of the order between $O(10^1)$ and $O(10^2)$, indicating that the droplet coalescence cases of the current study belong to the inertial-dominant and the inertial-viscous regimes.

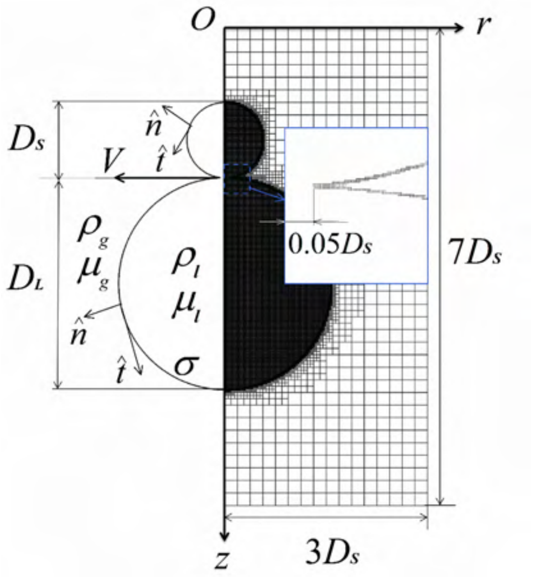

Figure 7.1 Computational domain and adaptive mesh for the current droplet coalescence study. The symmetry boundary condition is specified on the axis of symmetry and free outflow boundary conditions are specified on the other three boundaries. The zoomed-in window shows the grid configuration of the interface at the initial time of contact。

In order to resolve the droplet interface and the internal flow within the droplet, the computational domain is divided into three zones, namely the gas, the droplet interior and the interface zone. The mesh for each zone can be adaptively refined to a prescribed level, denoted by an integer N, at which the minimum cell size in the zone is of $O(2^{-N})$ of the zone dimension. Accordingly, we can use (N_g, N_d, N_i) to describe the refinement levels in all the three zones. As an example, Figure 7.1 shows an initial mesh at the refinement levels (5, 6, 7), in which the number of grid points is 13,851, equivalent to about 50,000 grid points in a uniform mesh system.

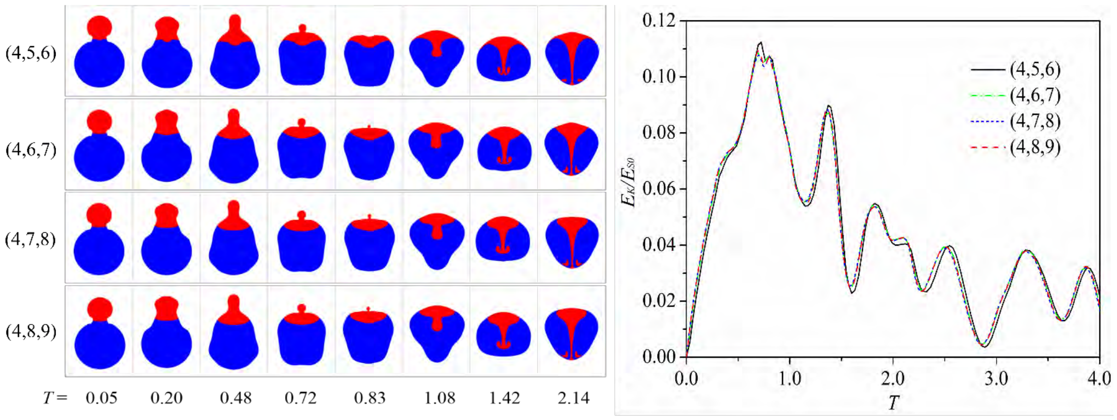

(a) (b)

Figure 7.2 Grid independence study for the simulation. (a) Comparison of droplet deformation and internal mixing pattern among different mesh levels, (4, 5, 6), (4, 6, 7), (4, 7, 8), and (4, 8, 9), where the three numbers in parenthesis are the mesh levels for the gas zone, the fluid zone, and the interface zone, respectively; (b) Comparison of the total kinetic energy, E_K, normalized by the initial surface energy, E_{S0}, for the different meshes presented in (a).

The grid independence of the computational results was examined in Figure 7.2. Figure 7.2(a) shows the comparison of droplet deformation and internal mixing pattern for the coalescence of water droplets with $Oh = 8.28 \times 10^{-3}$ and $\Delta = 2.0$. Four different mesh refinement levels, (4, 5, 6), (4, 6, 7), (4, 7, 8), and (4, 8, 9), were employed, which correspond to 5,351, 12,878, 40,180, and 142,897 grid points, respectively. The maximal grid points on equivalent uniform meshes are 86,016, 344,064, 1,376,256, 5,505,024, respectively. It is seen that all results in Figure 7.2(a) are qualitatively similar to each other, although the mesh (4, 5, 6) seems to render a slightly different internal jet pattern than the rest three finer meshes. For quantitative justification, Figure 7.2(b) further compares the evolution of the total kinetic energy (E_K) of the droplet, normalized by its initial surface energy (E_{S0}), for the same four meshes. The results are consistent with Figure 7.2(a) that the latter three meshes tend to share an identical curve, which slightly deviates from the first mesh (4, 5, 6). The above discussions suggest that the mesh (4, 6, 7) is sufficient for the current study. For a balance between accuracy and computational cost, the refinement level (4, 6, 8) were used in all the following computations. A typical simulation run up to $\mathrm{T} = 4.0$ takes approximately five hours of real time on two Intel Xeon E5-2630 processors with 12 cores.

The initial condition of the simulation set-up is illustrated in the zoomed-in plot of Figure 7.1. Because the interface constructed by the VOF method intrinsically has a finite thickness, the initial merging between the front surfaces of two drops inevitably causes a finite radius of the neck region as shown in the figure. This initial neck can be slightly adjusted by changing the local grid resolution around the initial contact point. To study the impact of the initial neck, three different initial radii, $0.035D_S$, $0.048D_S$, and $0.060D_S$, are simulated. Similar analysis to the grid independence study were performed, and no notable difference was observed among the different cases. The results are not presented here because they are almost identical to Figure 7.2. Thus, the initial neck radius has negligible effect on the long-term process of drop coalescence. In practice, the initial neck radius of $0.048D_S$ was applied for all the following simulations.

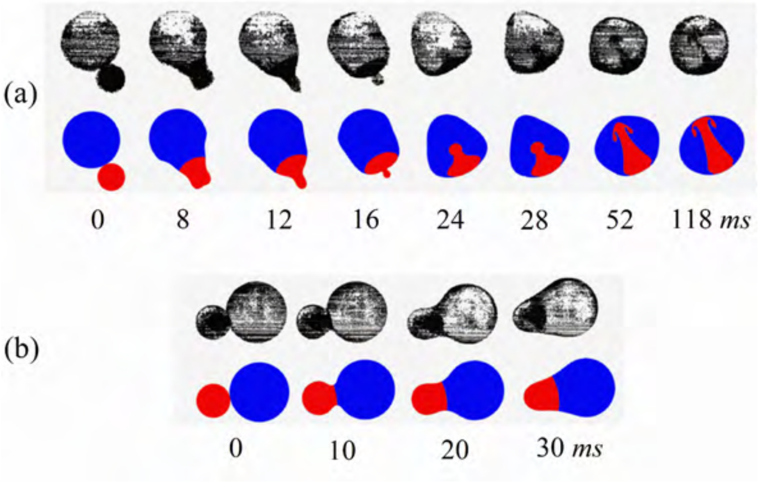

Figure 7.3 Comparison of the droplet mixing patterns between experiment[44] and simulation. (a) jet forming for a mixture of silicone oil and bromobenzene (3.3 CP measured viscosity), $We = 0.0, Oh = 0.012, \varDelta = 2.08$ and $t_c = 20.2$ms, (b) no jet for a high viscous silicone oil (99.0CP measured viscosity), $We = 0.0, Oh = 0.203, \varDelta = 1.75$ and $t_c = 57.5$ms.

To validate the present numerical methods, the coalescence of two initially stationary droplets made of a mixture of silicon oil and bromobenzene in the environment of water was first simulated and compared with the experiment of Anilkumar *et al.*[44], as shown in Figure 7.3(a). It is seen that the simulation results are in good agreement with the experimental images in terms of the evolution of droplet deformation and that of the jet-like internal mixing. Furthermore, as shown in Figure 7.3(b), the jet-like mixing is absent because of the significantly increased droplet viscosity. The simulation results also reproduce the experimental observation in that the smaller droplet lodges on the larger one to form a dome shape.

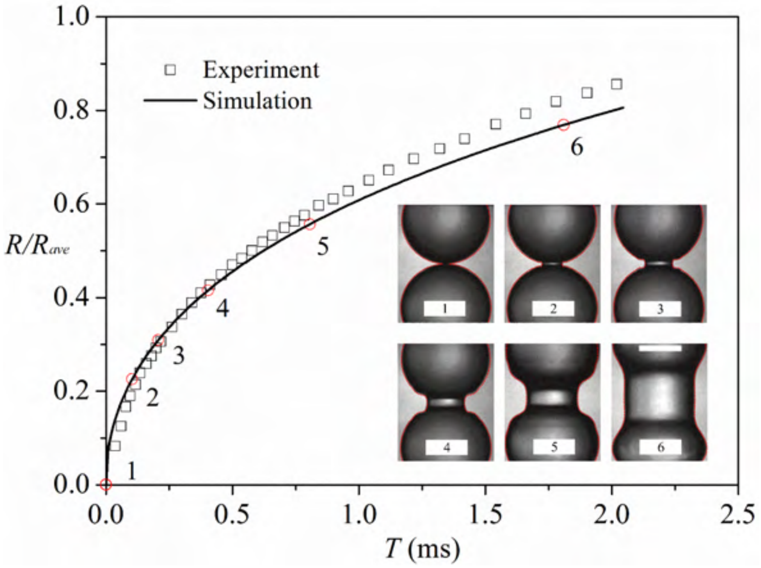

Figure 7.4 Comparison of the droplet coalescence speed between experiment[147] and simulation. The controlling parameters are $Oh = 2.5 \times 10^{-3}$ and $\Delta = 1.06$. The red-dotted lines in the sub-images are droplet interfaces obtained from the present simulation. Note that although $\Delta = 1.06$ was reported in the original work, $\Delta = 1.02$ was measured from the experimental images and therefore adopted in the simulation.

Figure 7.4 compares the present simulation with the experiment by Thoroddsen *et al.*[147] for coalescence between two water droplets in atmospheric air with $Oh = 2.5 \times 10^{-3}, \Delta = 1.06, \rho_g/\rho_l = 1.23 \times 10^{-3},$ and $\mu_g/\mu_l = 1.83 \times 10^{-2}$. The six sub-images illustrate the experimental evolution of the droplet interface, which is compared with the simulated interface in red dotted lines. It is seen that the simulation results well predict the coalescence process. Quantitative comparison of the coalescence speed is shown in the main plot of Figure 7.4, where R is the radius of the expanding neck (or bridge) between the two droplets and R_{ave} is the average radius of the two droplets. Again, the simulation results are in good agreement with the experiment data. The slight deviation could be attributed to the original experimental setup, where each droplet was either pendent or sessile in gravitational environment, with their far ends being attached to a tube, so that the two droplets are not strictly spherical. Before we proceed, it is noted that Figure 7.4 displays a scaling dependence of $R \sim \sqrt{t}$, with the scaling coefficient being approximately $1.1(\sigma R_{avg}/\rho_l)^{1/4}$. This is consistent with the scaling law for droplet coalescence dominated by inertia, which was proposed by Eggers *et al.*[148] and experimentally validated by Wu *et al.*[149] and Aarts *et al.*[150]. Thus, it justifies that the current droplet coalescence study belongs to the inertial regime.

7.3 Phenomenological description of internal jet-like mixing

7.3.1 Representative case study

As a representative case, the coalescence of n-decane droplets was first investigated for a fixed Ohnesorge number of $Oh = 1.56 \times 10^{-2}$ and various size ratios. To show the long-time behavior of the internal mixing, the simulation lasts until $T = 4.0$. To facilitate our presentation, only three size ratios, namely, $\Delta =$ 1.8, 2.2 and 2.8 are shown in Figure 7.5(a). The mixing process is illustrated in the right half of each simulation image and the variation of local pressure, normalized by $3\sigma/D_S$, is shown in the left half image.

Phenomenologically, the entire process from the commencement of droplet coalescence to $T = 4.0$ can be divided into four stages according to the characteristics of droplet deformation and jet formation.

1) **Stage I** (about $T = 0.00 \sim 0.20$): upon the droplet coalescence at the contact point, an interfacial ring cusp is formed in the vicinity of the point and tends to be smoothed out under the high capillary pressure. This causes a rapid, radially outward movement of the ring interface at the beginning stage of droplet coalescence. In the meantime, most of the mass in the droplets do not have noticeable movement along the axial direction. As a result, away from the vicinity of the ring cusp, the droplets remain almost spherical and the local pressures do not vary significantly.

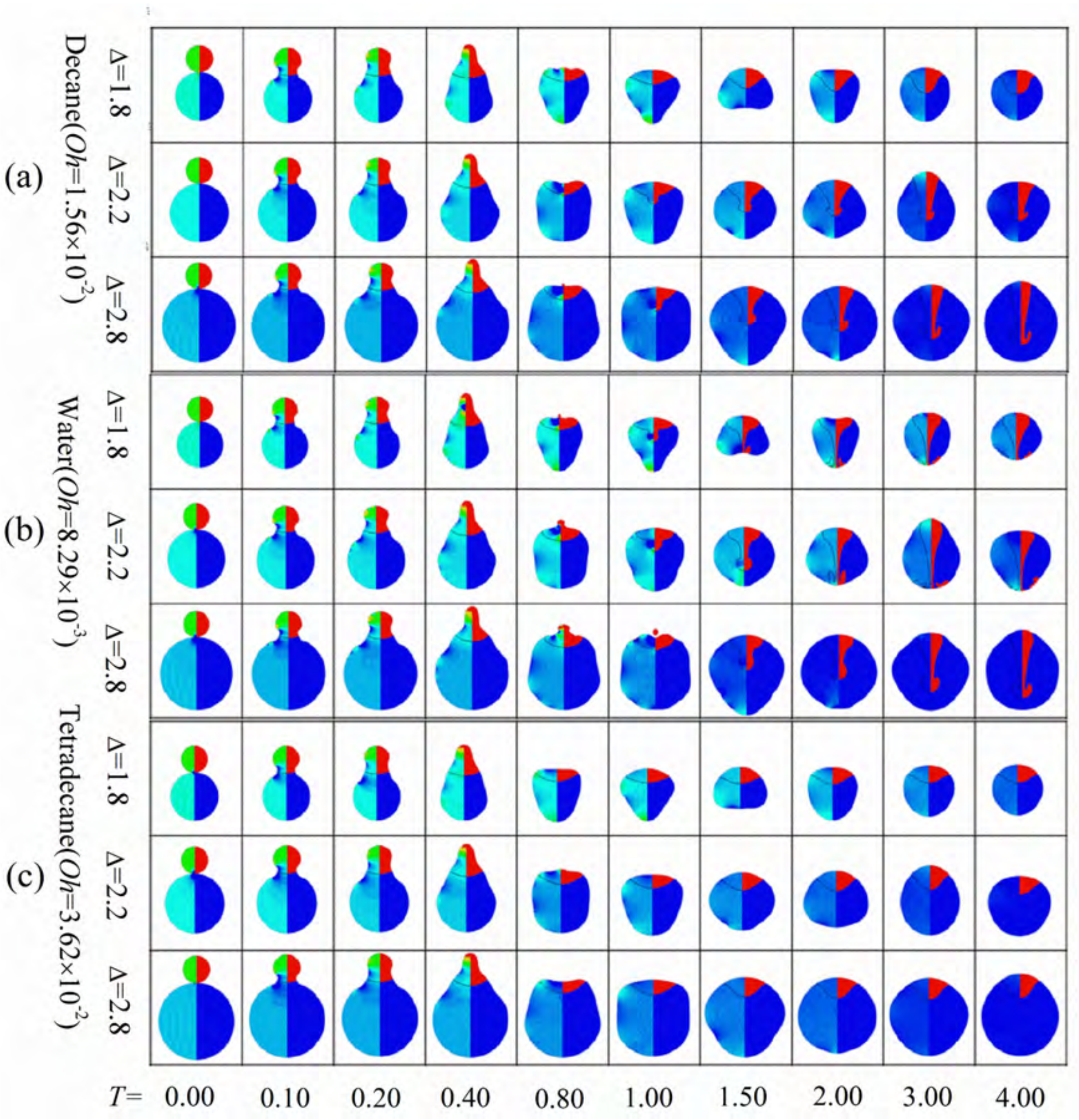

Figure 7.5 Deformation and mixing upon the coalescence of initially stationary droplets of (a) n-decane with $t_c = 0.50\text{ms}$, (b) water with $t_c = 0.33\text{ms}$, and (c) n-tetradecane with $t_c = 0.48\text{ms}$, and for different Δ. The left contour shows the static pressure, with the magnitude ranging from 0.0 of blue to 2.0 of red. The right contour plots the tracer variable, with red and blue tracking the fluid initially from the small and large droplets, respectively.

2) **Stage II** (about $T = 0.20\sim0.40$): the mass in the smaller droplet is driven into the larger one under the capillary pressure difference of about $4\sigma(D_S^{-1} - D_L^{-1})$. A finger-like bulge with a round head is consequently formed on the far side of the smaller droplet, as clearly seen at $T = 0.40$. The radius of the round head of the

bulge, denoted by D_B, is smaller than that of the initial droplet, and thereby results in larger capillary pressure (shown in red) in the bulge than that in the large droplet.

3) **Stage III** (about $T = 0.40 \sim 0.80$): the bulge merges into the droplet under the capillary pressure difference of about $4\sigma(D_B^{-1} - D_L^{-1})$. The mass of the bulge obtains an axial momentum in the vicinity of the axis as the result of the conversion of the surface energy of the bulge to its kinetic energy. After the bulge completely merges into the droplet, the pressure inside the droplet becomes almost uniform regardless of the slight local pressure variation due to the droplet oscillation.

4) **Stage IV** (about $T = 0.80 \sim 4.00$): the final stage is characterized by the long-time behavior of the jet-like mixing, which is affected by the viscous dissipation of the internal flow motion and the droplet oscillation. It is seen that all the cases show jet-like mixing patterns except the case of $\Delta = 1.8$, in which the merged smaller droplet lodges on the larger one to form a dome shape during the entire stage.

7.3.2 Influence of Oh and Δ

For a comparative study of the phenomena, the above simulations were repeated for water and n-tetradecane, which provide experimentally realizable comparison with n-decane for studying the influences of surface tension and viscosity. Specifically, the viscosity of water $(8.9 \times 10^{-4} Pa \cdot s)$ at room temperature is very close to that of n-decane $(8.5 \times 10^{-4} Pa \cdot s)$, but the surface tension of water $(7.29 \times 10^{-2}\, N/m)$

is almost three times larger than that of n-decane $(2.38 \times 10^{-2}\, N/m)$. The surface tension of n-tetradecane $(2.65 \times 10^{-2}\, N/m)$ is similar to that of n-decane, but its viscosity $(2.03 \times 10^{-3} Pa \cdot s)$ is substantially larger than that of n-decane. The simulation results for the coalescence of water droplets at various size ratios and with $Oh = 8.29 \times 10^{-3}$, $\rho_g/\rho_l = 1.22 \times 10^{-3}$ and $\mu_g/\mu_l = 1.80 \times 10^{-2}$, are shown in Figure7.5(b). The results for the coalescence of n-tetradecane droplets with $Oh = 3.62 \times 10^{-2}$, $\rho_g/\rho_l = 1.61 \times 10^{-3}$ and $\mu_g/\mu_l = 7.94 \times 10^{-3}$ are shown in Figure 7.5(c). Several observations can be made by comparing the results shown in Figure 7.5, as follows.

First, owing to the smaller Oh and thereby decreased viscous dissipation of water droplets, the mushroom-like jet emerges at $\Delta = 1.8$, as shown in Figure 7.5(b), but it is absent for either n-decane or n-tetradecane droplets at the same size ratio, as shown in Figure 7.5(a) and Figure 7.5(c), respectively. It is also noted that the jet-like mixing pattern is absent for n-tetradecane droplets at all the size ratios. These results accord with and extend the earlier experimental observation of Anikumar *et al.*[44] that the formation of “mushroom-like” jet is suppressed by increasing the droplet viscosity.

Second, for the cases with the emergence of the distinct jet-like mixing, water droplets display enhanced and faster mixing compared with n-decane droplets, as shown in Figure 7.5(b) compared with Figure 7.5(a) for $\Delta = 2.2$. It is seen that the jet penetrates the whole droplet and hits the bottom surface at $T = 2.0$ for the water droplet, but the jet penetration is about a half of the droplet size for the n-decane droplet at the same time. In view of the characteristic time t_c of the water droplet is smaller than that of the n-decane droplet of the same size, the evolution of the jet-like mixing in the former is even faster and more substantial.

Third, an interesting albeit incidental phenomenon was observed for the water droplets of $\Delta = 2.8$, as shown in Figure 7.5(b). A thin neck forms on the bulge and pinches off the bulge to generate a satellite droplet, which subsequently re-merges into the "father" droplet, as shown at $T = 1.00$. Although the jet-like mixing pattern still emerges, it is not as prominent as the case without the pinch-off. In the experimental study of the pinch-off phenomenon during the coalescence of unequal-size droplets, Zhang *et al.*[46] found that there exists a critical Δ_{cr} for the emergence of pinch-off and that Δ_{cr} increases monotonically with Oh. For $Oh = 8.29 \times 10^{-3}$, the predicted Δ_{cr} is about 2.6, which slightly overshoots 2.3 observed in Zhang *et al.*'s experiments[46]. The overshooting is caused by that the increasingly attenuated liquid neck is not sufficiently resolved in the present study. Physically, pinch-off occurs when two interfaces become sufficiently close to one another, being of $O(10)\,\mathrm{nm}$, so that the van der Waals force triggers the interface collapse. Quantitatively predicting the pinch-off requires the numerical resolution of an extremely thin liquid neck, which is computationally challenging and therefore bypassed in the present study by limiting out scope to the size ratios below the critical ones determined by Zhang *et al.*'s experiment[46].

7.3.3 Regime nomogram of jet-like mixing

The above comparative study has suggested that Oh and Δ are crucial to the appearance of the internal mixing. In order to further quantify the influences of Oh and Δ on the formation of the jet-like mixing pattern, we extended the simulations to wider ranges of these two parameters. The resulting $\Delta - Oh$ regime nomogram of the parametric study is shown in Figure 7.6.

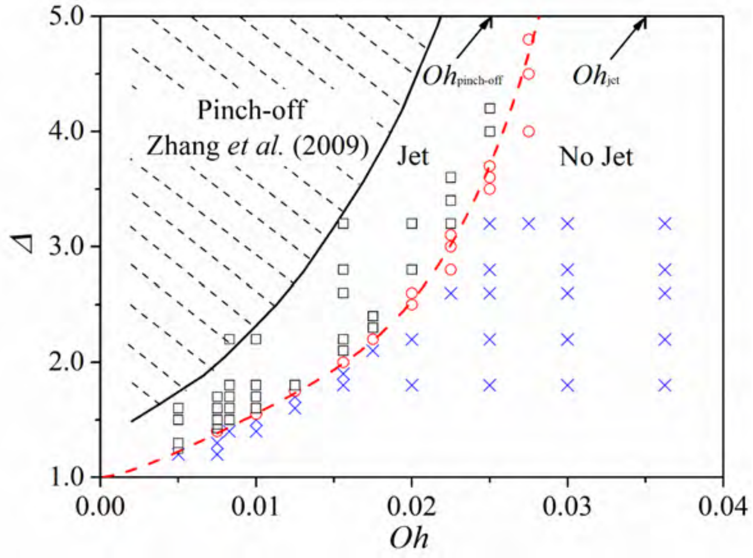

Figure 7.6 Regime nomogram of initially stationary droplet coalescence in the $\Delta - Oh$ parametric space. The jet-like mixing is denoted by the square, the no-jet regime by the cross, and the transition by the circlet. The red-dashed fitting line is given by the fourth-order polynomial, $\Delta = 1.3691 \times 10^7 Oh^4 - 4.6129 \times 10^5 Oh^3 + 6.4108 \times 10^3 Oh^2 + 25.0344 Oh + 1$. The dashed area corresponds to the ranges of Δ and Oh effecting droplet pinch-off, experimentally given by Zhang *et al.*[46].

For a given Oh, the jet-like mixing occurs as Δ is increased above a critical value indicated by the dashed line. Phenomenologically, the non-dimensional capillary pressure difference, $4(1-\Delta^{-1})$, between the small and large droplets, increases with Δ and could be a driving force for the jet formation. Furthermore, Figure 7.5 also shows that as increasing Δ the coalescence-induced internal flow tends to be concentrated around the symmetry axis, which could serve as an additional source promoting the jet formation. It can be also observed that the critical Δ for the emergence of the internal jet increases with Oh, which again verifies the observations from Figure 7.5 that larger Oh tends to suppress the jet formation. At this point, considering the trend of the red-dashed curve in Figure 7.6, one might be curious if there exists a threshold Oh beyond which jet formation is completely suppressed. Theoretically, this is highly possible since any jet is a convective phenomenonthat could be suppressed with sufficiently large viscosity. Realizing that such a threshold can be determined numerically by simulating the case with near-infinity size ratio, which is computational challenging, we instead simulate the limiting problem: an inertialess droplet merged into a liquid pool. The result is marked by Oh_{jet} in Figure 7.6, which shows that the mushroom-like jet does not appear when Oh is increased above 0.035. The details about this simulation are not provided here for brevity.

For a complete phenomenological description of the problem, Zhang *et al.*'s experimental data on the emergence of droplet pinch-off are also plotted in Figure 7.6 as a shadow regime. It is noted that pinch-off does not occur for $Oh > 0.025$ in their experiment.

7.4 Main vortex ring and its role in internal jet-like mixing

7.4.1 Identification of main vortex ring synchronized with internal jet-like mixing

We have demonstrated the dependence of the emergence of the internal jet on Oh and Δ, however the basic mechanism of the jet formation still requires further investigation. As has been discussed in the Background, the generation of the jet-like mixing pattern should not be fundamentally different from other similar jetting phenomena, for example a starting vortex jet[151, 152] formed due to the self-induced motion of a single vortex ring. This conjecture is partly substantiated in Figure 7.7 by the similar appearance of the jet-like structure and the vortex ring inside the merged droplet, characterized by normalized vorticity, $\omega^* = \omega t_c$. From previous studies[151, 152], the formation of a starting jet can be boiled down to two essential problems: what is the source of vorticity forming the vortex ring? and how does the vortex ring detach from its source to form the jet? Similarly, we can illustrate the two important processes, namely, the generation of vorticity and the detachment of the main vortex ring, for the distinct internal jet subsequent to the droplet coalescence.

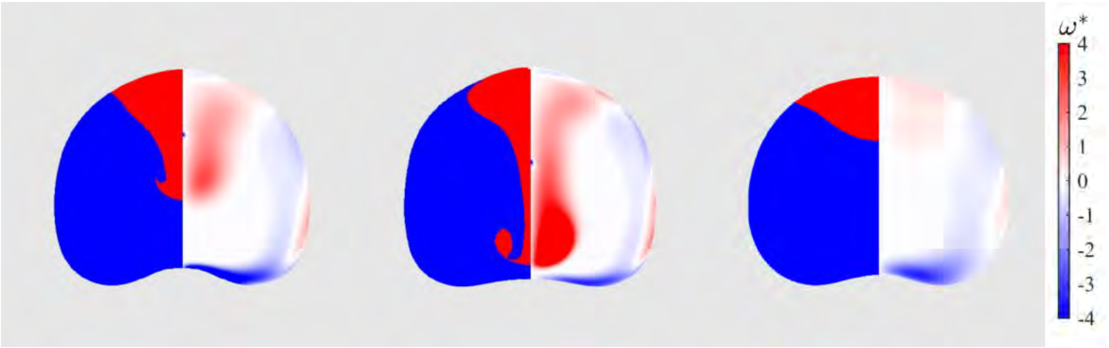

(a) (b) (c)

Figure 7.7 Comparison between the tracer variable distribution (left) and vorticity contour (right) at $T = 1.70$ for the cases of (a) n-decane, (b) water, and (c) n-tetradecane with $\Delta = 2.2$. The color bar applies to the vorticity contours throughout the paper.

In order to study the generation and evolution of the main vortex ring that is responsible for the formation of the internal jet, one needs to first identify and track the region of the vortex. For the present problem having axisymmetry, we employ a simple vorticity-contour approach and consider the vorticity contour, $\omega = \omega_v$, encircling the main vortex as the vortex boundary, where ω_v is a small threshold vorticity. The results for a representative case (n-decane droplets with $\Delta = 2.2$) are presented in Figure 7.8, where the green contour on the left side of the droplet represents the identified boundary of the main vortex. By comparing the green contour with the vorticity contour on the right side of the droplet, we indeed verify the vorticity-contour approach to be effective in capturing the main vortex among other vortices emerging at different stages of droplet coalescence.

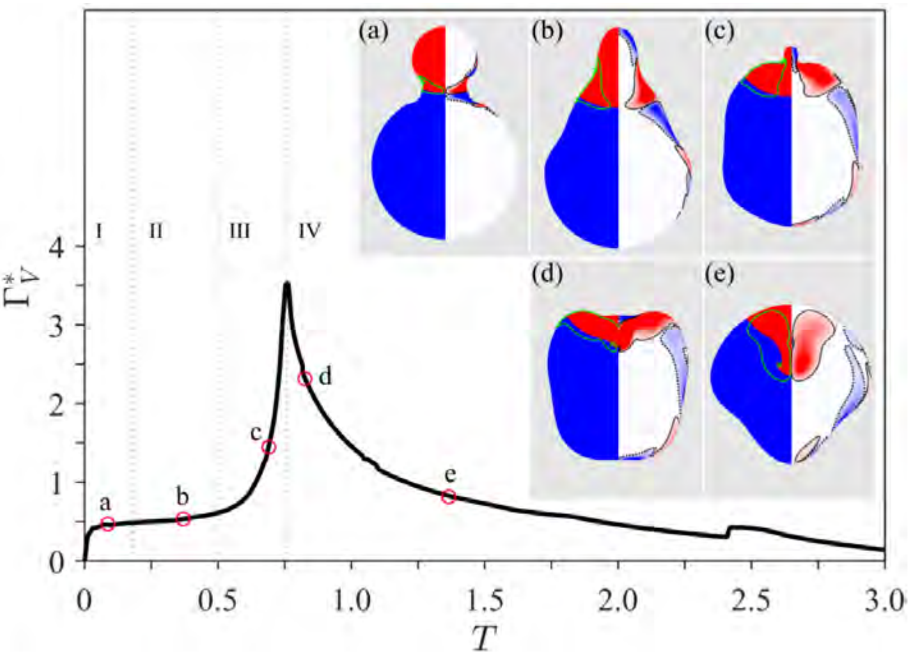

Figure 7.8 The main plot shows the evolution of the non-dimensional circulation of the main vortex for n-decane droplet coalescence with $\Delta = 2.2$, and $Oh = 1.56 \times 10^{-2}$. The subfigures (a)-(e) are the tracer variable plot (left) and vorticity contour (right) at the typical times (red circlets) on the vorticity evolution curve. In each subfigure, the green contour on the left side of the droplet represents the boundary of the main vortex identified through the vorticity-contour approach. The green cross marks the center of the main vortex corresponding to the local maximum vorticity. For clarity of illustration, positive and negative vortices in the vorticity contour are encircled by solid and dashed contour lines, respectively.

The identification of the main vortex region also enables the estimation of the total vorticity within the main vortex. The total vorticity is evaluated by calculating the circulation

$$\Gamma_V = \int_{A_V} \omega \, dA \tag{7.3}$$

where A_V is the cross-section area of the main vortex. It should be noted that the volumetric integration over the volume, V_V, of the main vortex, $\int_{V_V} \omega \, \mathrm{d}V$, is not an appropriate quantity for measuring the total vorticity. This is because Kelvin's circulation theorem[136, 153] dictates that Γ_V is a conserved quantity in an ideal axisymmetric flow, but the volumetric integration is dependent on the radial distance of the vortex from the axis (Saffman[136], Eq. 1.5.22). It is seen in Figure 7.8 that Γ_V first increases and then decreases at a slower rate, implying the existence of two physical processes: vorticity generation and vortex detachment, that will be discussed in detail in Section 7.4.2 and 7.4.3.

The calculation of the total vorticity provides further justification for the correlation between the main vortex ring and the internal jet-like mixing at different stages of droplet coalescence.

1) **Stage I**: as the initial droplet coalescence occurs, it can be observed from Figure 7.8(a) that vorticity develops only in the vicinity of the initial coalescence point, where surface deformation and its induced flow start. The rapid, outward expansion of the contacting region between the two droplets causes dramatic changes in the droplet geometry and velocity, thereby contributing to a fast rate of vorticity generation.

2) **Stage II**: when the initial coalescence region has sufficiently expanded as shown in Figure 7.8(b), the initial conversion from surface energy to kinetic energy gradually reaches stagnant. As a result, the velocity and the geometry of the droplet enter a slow-variation stage, causing a gradual vorticity generation inside the main

vortex. By the end of this stage, the remainder of the smaller droplet becomes an axial finger-like liquid bulge, forming a new neck which would lead to the next peak of surface energy discharge.

3) **Stage III**: the fluid bulge collapses into the large droplet under surface tension as shown in Figure 7.8(c). Similar to Stage I, a substantial amount of surface energy of the merged interface is rapidly converted to the kinetic energy of the induced flow around the confined neck region of the small fluid bulge, resulting in massive vorticity production in the main vortex.

4) **Stage IV**: after the complete merge of the fluid bulge into the large droplet, the main vortex ring starts to detach from the droplet surface and eventually forms the internal jet, as shown in Figure 7.8(d) and Figure 7.8(e). During this detaching process, the circulation of the main vortex ring first declines rapidly because of the diffusion of negative vorticity from the surface, and then drops gradually because of viscous dissipation after the complete detachment of the vortex ring.

7.4.2 Formation and growth of main vortex ring in stage I and III

In this section, we focus on the process of vorticity generation associated with the main vortex. As has been discussed in the Background, Batchelor[145] extended Helmholtz’s third theorem[136] or Kelvin’s circulation theorem[136] to the viscous flows, and summarized that “vorticity cannot be created or destroyed in the interior of a homogeneous fluid under normal conditions, and is produced only at boundaries" (p. 266 of Ref.[145]). Therefore, the initial generation of vorticity associated with the main vortex must happen at the gas–liquid interface. For the present problem, the significantly smaller density and viscosity of gas compared with those of liquid enable us to approximate the liquid-gas interface as a free surface with a vanishing shear stress[151, 154] on it. In the reference frame defined in Figure 7.1, the shear stress has the form

$$\sigma = \hat{\boldsymbol{n}} \cdot \nabla \boldsymbol{u} \cdot \hat{\boldsymbol{t}} + \hat{\boldsymbol{t}} \cdot \nabla \boldsymbol{u} \cdot \hat{\boldsymbol{n}} = 0 \tag{7.4}$$

and hence

$$\omega = \hat{\boldsymbol{n}} \cdot \nabla \boldsymbol{u} \cdot \hat{\boldsymbol{t}} - \hat{\boldsymbol{t}} \cdot \nabla \boldsymbol{u} \cdot \hat{\boldsymbol{n}} = -2\hat{\boldsymbol{t}} \cdot \nabla \boldsymbol{u} \cdot \hat{\boldsymbol{n}} \neq 0 \tag{7.5}$$

According to Lundgren and Koumoutsakos[154], the interface vorticity in Equation (7.5) could be further decomposed into two parts by

$$\omega = -2\frac{\partial \boldsymbol{u}}{\partial s} \cdot \hat{\boldsymbol{n}} = -2\frac{\partial u_n}{\partial s} + 2\,\kappa u_t \tag{7.6}$$

where $\kappa = \hat{\boldsymbol{t}} \cdot \partial \hat{\boldsymbol{n}} / \partial s$ is the local curvature of the surface; u_n and u_t are the velocity components normal and tangential to the surface, respectively. Equation (7.6) means that the only source of vorticity for the current problem is the interfacial flow and is affected by both the interface geometry and the interfacial flow velocities (gradients). For steady flows where the free surface is stationary, u_n becomes zero and the first term of Equation (7.6) could be dropped out. For the present problem that is highly unsteady and involves significant deformation of the interface, both terms of Equation (7.6) individually affects the vorticity generation of the main vortex at different stages. Furthermore, Equation (7.6) can be interpreted that vorticity generation at a free surface is inevitable in the presence of either surface deformation or flow along curved surface. Due to the effect of viscosity, the vorticity generated at the interface would be diffused into the bulk fluid. In a low viscosity fluid, the diffusion mainly happens at a thin layer close to the interface, thus forming a surface-attached viscous shear layer or boundary layer, outside of which the flow is primarily convective. In this sense, the viscous shear layer should be considered more as an evidence of the diffusive vorticity transportation from the interface to the bulk fluid of low viscosity, rather than a source of vorticity itself.

Figure 7.9 shows the distribution of vorticity at the gas–liquid interface where massive vorticity is being generated initially inside the main vortex at Stage I. We can observe that a main peak of positive vorticity is located between s_2 and s_3, which corresponds to the portion of the interface overlapping with the boundary of the main vortex. This verifies that the growth of the total vorticity inside the main vortex shown in Figure 7.8 is indeed related to the non-zero vorticity generation at the interface. Furthermore, the vorticity contributions from the two terms of Equation (7.6) are also plotted in Figure 7.9. It is seen that the first term, $-2\partial u_n/\partial s$, almost equals the vorticity itself, and the second term, $2\kappa u_t$, is negligible. This implies that the initial vortex generation in Stage I is mainly caused by the normal velocity gradient in the tangential direction of the outwardly moving surface, as the movement of surface is normal to the surface and u_n decreases from s_2 to s_3. It is interesting to note that vorticity generation is approximately symmetric with respect to the contacting plane of the two droplets during Stage I. Specifically, a counter-rotating vortex is created on the large droplet side from the surface between s_1 and s_2, with the $-2\partial u_n/\partial s$ term again dominating the vorticity generation. Although this “negative” vortex is only slightly weaker than the main vortex, it gradually decays in later stages, whereas the main vortex will be further enhanced.

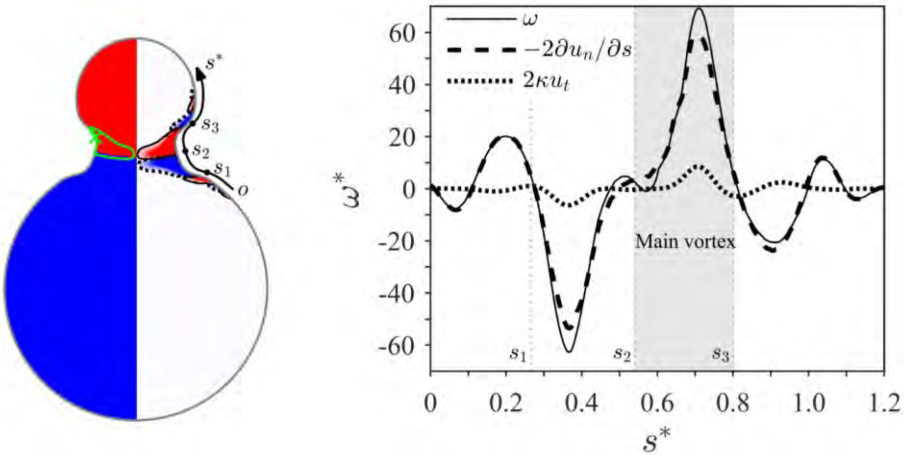

(a) (b)

Figure 7.9 (a) The tracer variable plot (left) and vorticity contour (right) at a representative instant of Stage I [Figure 7.8(a)] for n-decane droplet coalescence with $\Delta = 2.2$, and $Oh = 1.56 \times 10^{-2}$. The green contour marks the boundary of the main vortex. (b) The vorticity distribution along the gas–liquid interface near the main vortex. The s^* coordinate is along the surface of the droplet, as indicated by the black arrow in (a).

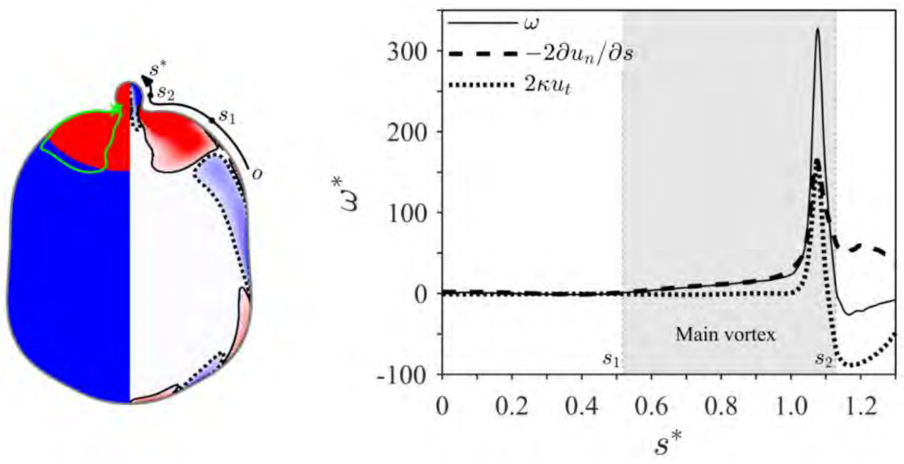

(a) (b)

Figure 7.10 (a) The tracer variable plot (left) and vorticity contour (right) for a representative instant of Stage III [Figure 7.8(c)] for n-decane droplet coalescence with $\Delta = 2.2$ and $Oh = 1.56 \times 10^{-2}$. (b) The corresponding vorticity distribution along the gas–liquid interface near the main vortex.

In Section 7.4.1, we have seen that Stage III corresponds to the primary vorticity generation phase for the main vortex. To understand the underlying mechanism of vortex growth during this stage, Figure 7.10 plots the vorticity distribution along the gas–liquid interface at the instant corresponding to Figure 7.8(c). Here, the curve between s_1 and s_2 represents the portion of the gas–fluid interface associated with the main vortex. It can be observed that major vorticity generation occurs in the vicinity of the connecting point between the bulge and the main droplet. The two vorticity components in Equation (7.6) are also plotted in Figure 7.10, and their peaks are comparable to each other along the interface of the main vortex. This indicates that both the interface deformation and the large curvature equally contribute to the significant vorticity generation during this stage. It is also noted that, in the region beyond the main vortex and towards the axis, the tangential velocity and curvature combined generate negative vorticity, which exceeds the positive vorticity generated by interface deformation, causing the emergence of a negative vortex inside the small bulge.

7.4.3 Detachment of main vortex ring in stage IV

The above analysis answers the question about where the vorticity inside the internal jet comes from, but it does not explain how the concentrated vorticity becomes a self-induced vortex ring that subsequently translates within the droplet to form an internal jet. In other words, the cumulation of vorticity inside a vortex ring does not guarantee the formation of a jet. Taking the starting jet problem as an example, the jet formation criterion requires that the non-dimensional formation time is larger than a certain value[151] (a typical number is 4), when the vortex ring is strong enough to "rip-off" its own vorticity-feeding shear layer; otherwise, the vorticity would keep growing inside the vortex ring without detachment and thereby no jet can be formed.

For the formation of the internal jet due to droplet coalescence, we hypothesize that a similar mechanism exists such that the internal jet does not form until the main vortex ring detaches from the surface of the droplet. Consequently, there must be an additional mechanism that "peels" the original vortex ring off the surface. This problem resembles that of flow separation on a smooth body, where vorticity inside the boundary layer detaches from the surface to become a free vortex in the wake. It is well-known that flow separation happens where the adverse pressure gradient is strong enough to generate vorticity opposite to the original shear layer. Analogically, we hypothesize that the emergence of negative vorticity at the liquid-gas interface would be responsible for the detachment of the main vortex ring.

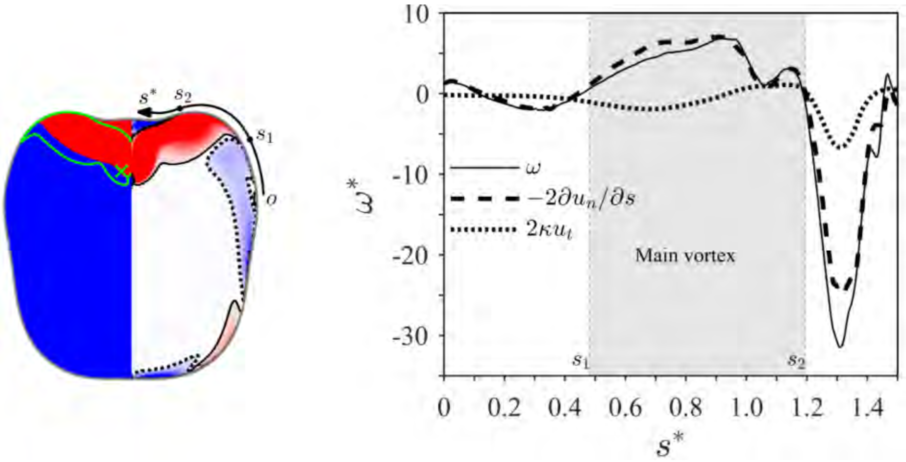

(a) (b)

Figure 7.11 (a) The tracer variable plot (left) and vorticity contour (right) for a representative instant of Stage IV [Figure 7.8(d)] for n-decane droplet coalescence with $\Delta = 2.2$ and $Oh = 1.56 \times 10^{-2}$. (b) The corresponding vorticity distribution along the gas–liquid interface near the main vortex.

To verify this hypothesis, we plot the vorticity distribution along the surface of the droplet at the beginning of Stage IV, as shown in Figure 7.11. It is confirmed that the main vortex starts to detach from the central portion of the interface ($s^* > s_2$) where significant negative vorticity is generated. Moreover, Figure 7.11 also shows that the negative vorticity generation near the axis is largely attributed to the first term of

Equation (7.6), $-2\partial u_n/\partial s$. We further recognize that this negative vorticity generation actually corresponds to an outward retraction of the dented surface subsequent to the complete merge of the droplet. In analogy to flow separation, s_2 can be considered as a dynamic flow separation point, which moves in the radial direction as the negative vortex region expands out, and cut off the main vortex from the surface in a razor-like fashion. After the main vortex completely detaches from the surface, it becomes a free vortex ring translating with its self-induced velocity to form an internal jet.

Here, the new information obtained in this section is emphasized. Ever since the phenomenon of the jet-like mixing following droplet coalescence was reported by Anilkumar *et al.*[44], researchers have been curious about its formation mechanism. Nobari and Tryggvason[144] calculated the evolutions of the surface and kinetic energies, and attributed the formation of the internal jet to a rapid release of surface energy during the injection of the small drop. This explanation is further substantiated by Liu *et al.*'s recent work[22]. We noted that, while this "surface energy" theory covers the fundamentals of the jet formation, it does not give the whole picture to the phenomenon as sufficient details about the process are still lacking. Specifically, from the vortex dynamics perspective, two conditions are necessary for a vortex ring to evolve into a jet: the accumulation of vorticity and the separation from the vorticity source. Through the current analysis, we managed to trace the origination of the main vortex ring back to the initial coalescence stage. Furthermore, we found that the vortex ring grows substantially due to a combined effect of dramatical interface deformation and large interface curvature during the entry of the small droplet, which coincides with the period of rapid surface energy discharge found by Nobari and Tryggvason[144]. Finally, after the entry of the small droplet a reverse motion of the interface induces a negative shear layer, which facilitates the detachment of the main vortex ring from the liquid-gas and consequently initiates the formation of the internal jet.

7.5 Vortex-ring-criterion for internal jet formation

Previous sections have demonstrated that the emergence of the internal jet after droplet coalescence is closely related to the generation and detachment of the main vortex. In this section, we shall seek quantitative criterion of the internal jet based on the main vortex ring.

We start by comparing the evolution of the main vortex between cases with the internal jet (water droplets with $\varDelta = 1.8, 2.2$ and n-decane droplets with $\varDelta = 2.2$) and those without the internal jet (n-decane droplets with $\varDelta = 1.8$ and n-tetradecane droplets with $\varDelta = 1.8, 2.2$), as shown in Figure 7.12. The droplet configurations and vorticity contours at the instant when the vortex ring completely detaches from the droplet surface are also presented in the figure, with their corresponding total vorticities being marked on the circulation evolution curves, respectively. It is seen that, at the instant of vortex detachment, the cases without jet formation have significantly lower total vorticity compared with the cases with jet formation. Moreover, the lower circulation for the cases without jet formation should be attributed to either shorter period or smaller rate of vorticity generation during Stage III. It is noted that the less total vorticity generated during Stage III is related to the diminished bulge structure created at the end of Stage II, which does not possess enough surface energy to be converted during Stage III.

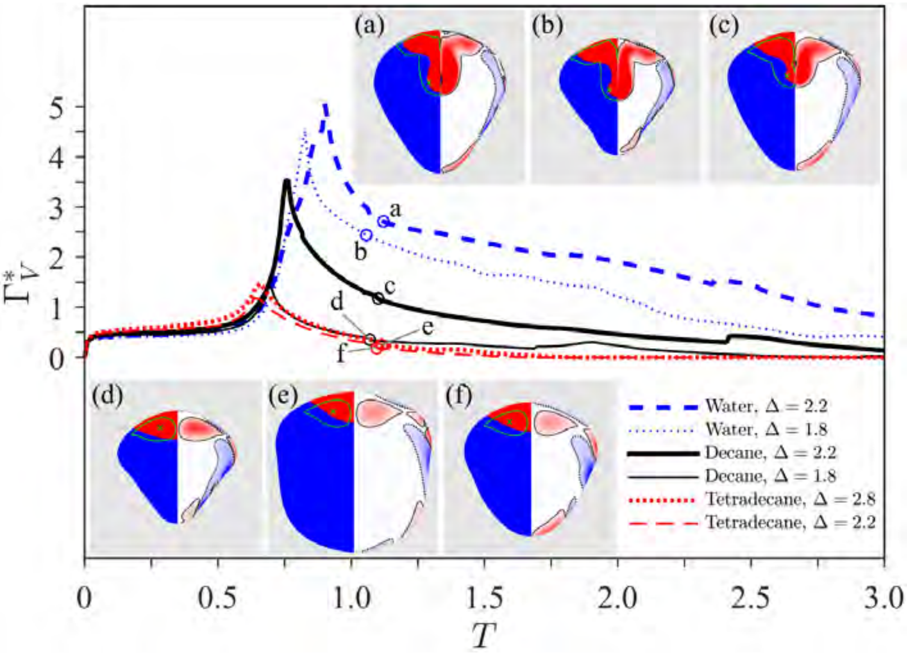

Figure 7.12 Evolution of the non-dimensional circulation around the main vortex for different cases of droplet coalescence. The subfigures (a)-(f) present the tracer variable plot (left) and vorticity contour (right) for the instants when the main vortex completely detaches from the surface of the droplet. The circulations corresponding to these instants are also marked on the evolution curves.

The above analysis qualitatively indicates that the internal jet appears only if the vortex ring is strong enough by the end of the vortex detachment. Physically, an ideal free vortex ring would readily translate downstream and form a jet under its self-induced flow, unless the viscosity significantly dissipates the vortex ring. Consequently, the formation of the internal jet after the vortex detachment is determined by the competition between the advective momentum associated with the vortex ring and the momentum lost due to viscous diffusion. To characterize this competition, a Reynolds number can be defined by

$$Re_J = \frac{U_V r_V}{\nu} \tag{7.7}$$

where U_V and r_V are the characteristic translational velocity and the radius of the free vortex ring, respectively. Based on the dynamics of a vortex ring[136], U_V can be expressed as

$$U_V = \frac{\mathit{\Gamma}_V}{4\pi r_V} \tag{7.8}$$

Combining Equations (7.7) and (7.8) gives

$$Re_J = \frac{\mathit{\Gamma}_{VD}}{4\pi\nu} = \frac{\mathit{\Gamma}_{VD}^*}{4\pi Oh} \tag{7.9}$$

where $\mathit{\Gamma}_{VD}$ (and its non-dimensional form $\mathit{\Gamma}_{VD}^*$) represents the circulation of the main vortex ring when it completely detaches from the droplet surface.

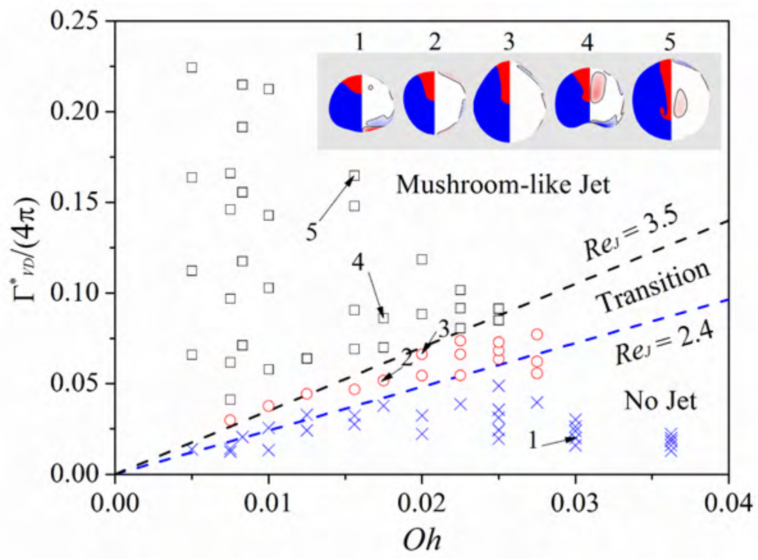

Figure 7.13 Validation of the vortex criterion for the jet formation for different cases of droplet coalescence. The slopes of the two dashed lines correspond to $Re_J = 2.4$ and $Re_J = 3.5$, marking the transition from the no-jet regime to the mushroom-like jet regime. Here, all data points correspond to the cases of different $\mathit{\Delta}$ and Oh plotted in Figure 7.6.

With $\mathit{\Gamma}^*_{VD}$ calculated in a similar approach to Figure 7.12 (circulations associated with the circlets), Equation (7.9) can be validated for different cases of droplet coalescence, as shown in the $Oh - \mathit{\Gamma}^*_{VD}$ regime nomogram in Figure 7.13. The mushroom-like jet formation occurs with about $Re_J > 3.5$, no jet formation with $Re_J < 2.4$, and in-between is a transition regime. The transition from the "no-jet" regime to the "mushroom-like jet" regime with increasing Re_J is manifested by the five typical cases from 1 to 5, as shown in the subfigures of Figure 7.13. Thus, the jet number Re_J serves as a phenomenological criterion for jet formation subsequent to the coalescence of two initially stationary droplets. It is noted that the data points presented in Figure 7.13 were calculated from their corresponding simulation cases in

Figure 7.6. While Figure 7.6 introduces the phenomenological observation of the dependence of the internal jet on the initial conditions (Δ and Oh), Figure 7.13 provides the fundamental mechanism explaining how the internal jet forms. Last, we emphasize that this jet-formation criterion does not depend on any presumption or initial condition of the merging droplets, indicating a prospect of extending this criterion to determining internal jet formation in more general situations, such as droplet collision and other microfluidic interactions.

7.6 Correlation between vortex-induced jet and internal mixing

As discussed in the Background, the present work was motivated to understand the influence of the jet-like structure on internal mixing. It is noted that the word "mixing" is used to describe the mass interminglement between two droplets. In general, the mass interminglement is twofold, namely, convective and diffusive. In the current study, the mass diffusion is neglected for two reasons. One is that the two droplets contain the same type of fluid, thus the concept of "mass diffusion" does not apply as there is no species concentration gradient. Second, even if two miscible fluids are considered, the Peclet number, which can be defined by $Pe = \sqrt{\sigma D_S/\rho_l}/D_m$, where D_m is the mass diffusivity, is estimated to be greater than $O(10^2)$ for the current problem, meaning that the effect of convection significantly overweighs the mass diffusion. Therefore, mixing in this study primarily reflect the effect of mass convection.

The comparative study in Section 7.3 has qualitatively demonstrated that mixing between the two droplets is intimately related to the mushroom-like jet. Specifically, the occurrence of the jet seems to cause large stretching and roll-up of the interfaces of two droplets, thereby increasing the contacting surface and contributing to enhanced mixing performance. To further quantify this observation on the internal mixing within the merged droplet, a mixing index M independent of Oh and Δ can be defined as follows[15, 143],

$$M = 1 - \frac{\int_V |C - C_\infty| H(f-1) dV}{\int_V |C_0 - C_\infty| H(f-1) dV} \tag{7.10}$$

where the VOF function $f = 0$ in the gas and $f = 1$ in the droplets; the Heaviside step function $H(f-1)$ limits the integration domain to be within the droplets. C, C_0, and C_∞ are the distribution functions of the time-dependent "concentration" of the small droplet liquid in the merged mass, in the unmixed droplets, and in the fully mixed mass, respectively, and are defined by

$$C = |2\varphi - 1| C_0, \quad C_0 = \begin{Bmatrix} 0, \varphi = 0 \\ 1, \varphi > 0 \end{Bmatrix}, \quad C_\infty = \frac{1}{1 + \Delta^3} \tag{7.11}$$

where φ is the spatially and temporally varying dye function, which is defined as 1 in the small droplet and 0 in the large droplet. Therefore, M varies between 0 and 1 with larger value indicating better mixing.

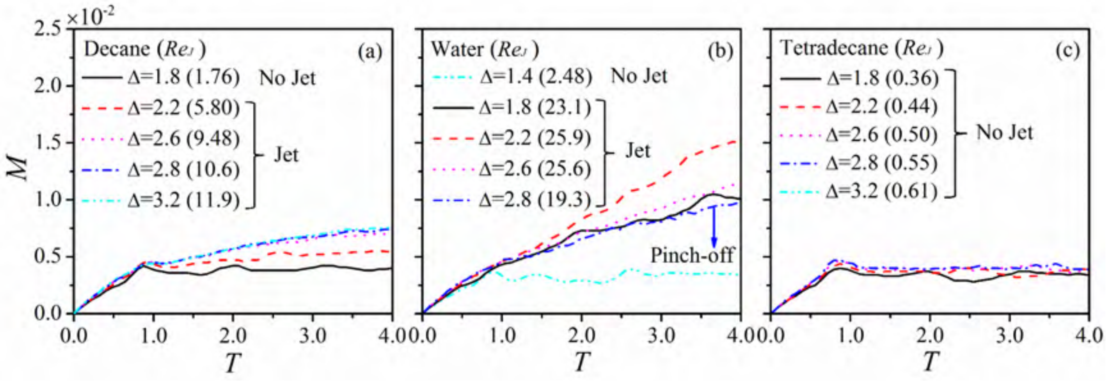

Figure 7.14 Time evolution of the mixing index for n-decane ($Oh = 1.56 \times 10^{-2}$), water ($Oh = 8.29 \times 10^{-3}$), and n-tetradecane ($Oh = 3.62 \times 10^{-2}$) droplets of various size ratios. Re_J for each case is presented in the parentheses to relate the performance of mixing to the formation of internal jet.

The time evolution of the calculated M for n-decane, water and n-tetradecane and for various Δ are shown in Figure 7.14. The slope of the curves quantifies the rate of mixing at different times. Several observations can be made about the mixing processes.

First, for all the cases, the mixing rate seems to be independent of Oh or Δ at Stages I-III (up to around $T = 0.8$), when the small droplet has not completely merged into the larger one. This is because mixing in the early stages are mostly caused by the geometrical changes of the two-droplet configuration. These changes are associated with the coalescence of interfaces around the initial contacting point (Stage I), the expansion of the contacting surface (Stage II), and the collapse of the liquid bulge (Stage III), which to a considerable extent are similar processes among cases with different Oh or Δ.

Second, the increase of M during Stage IV substantially varies with Oh and Δ, suggesting the important role of the jet-like structure that does not present until this stage. The values of Re_J for different cases are presented in the parentheses to indicate the correlation between jet formation and internal mixing. It is seen that, for small Re_J cases where no internal jet is formed, the average mixing rate is approximately zero in Stage IV and is almost independent of Re_J. Together with the above-discussed mixing independency during Stages I-III, it seems that mixing is intrinsically self-similar throughout the merging process if no internal jet presents. This, in turn, provides a direct evidence that the vortex-induced jet has a significant impact on the internal mixing of the merged droplet.

Third, for those cases where mushroom-like jet forms, Re_J measures the relative strength of the vortex ring associated with the internal jet. Therefore, larger Re_J corresponds to a stronger jet, and in turn indicates larger convective momentum or lower viscous dissipation or both; enhanced mixing rate is consequently expected. This can be readily verified by the n-decane cases shown in Figure 7.14(a), where the average mixing rate seems to monotonically increase with Re_J. Furthermore, comparing the n-decane cases with the water cases shown in Figure 7.14(b), we can also confirm that the water cases in general has larger mixing rates than the n-decane cases, as the water cases have larger Re_J.

Fourth, it is noted that the monotonic dependence of the mixing rate on Re_J seems to not hold exactly for the water cases. Specifically, the $\Delta = 2.2$ case has much larger mixing rate than the $\Delta = 2.6$ case, although Re_J for the two cases are nearly the same. This can be attributed to the tendency of droplet pinch-off for the water case with $\Delta = 2.6$, where the surface energy responsible for the interface oscillations at the later stage of internal mixing is significantly reduced. Moreover, for the cases with droplet pinch-off, the long-term mixing performance is also affected by the surface oscillations after the jet has penetrated through the merged droplet and hit the gas–liquid interface on the opposite side.

Finally, for the cases with internal jet but without droplet pinch-off, the average mixing rate also monotonically increases with Δ or decreases with Oh, which is consistent with our observation from Figure 7.5 that the jet-like mixing becomes more prominent with increasing Δ or decreasing Oh. It should be mentioned that the penetration depth of the fluid from the small drop was analyzed by Nobari and Tryggvason[144] to provide an indicator for the mixing effect, which is reasonable considering that the penetration depth is closely related to the strength of the internal jet. Thus, their results also show a similar monotonicity of the penetration depth with Δ for small Oh cases where internal jet exists. However, they did not quantify the mixing preformation for the internal jets, which have penetrated through the large drop and hit the surface of the other side. In this sense, the mixing index M of the current study is an improved approach in quantifying the mixing performance of droplet coalescence.

7.7 Concluding remarks

The coalescence of two initially stationary droplets of unequal sizes was investigated numerically, with emphasis on two key problems: the formation of the internal jet and its effect on mixing between the two droplets.

Phenomenologically, the jet-like mixing was perceived based on three representative fluids, water, n-decane, and n-tetradecane. It was found that both decreasing the fluid viscosity and increasing the size ratio would facilitate the emergence of the jet-like mixing. This observation was further justified by a regime nomogram describing the occurrence of the jet-like mixing with varying Δ and Oh.

The fundamental mechanism responsible for forming the internal jet was understood by first identifying the correlation between the jet-like structure and the main vortex ring inside the merged droplet. Based on the evolution of the main vortex ring, we identified three stages crucial to the jet formation, namely, vortex-ring formation, vortex-ring growth, and vortex-ring detachment. The initial vortex generation upon droplet coalescence, albeit being small in magnitude, is mainly caused by the normal velocity gradient in the tangential direction of the outwardly merging surface around the coalescence point. The rapid collapse of the small bulge into the large droplet, which results in dramatic interface deformation and local large-curvature interface, causes massive vorticity generation and therefore vortex-ring growth. The outward retraction of the dented surface promotes the generation of negative vorticity that detaches the main vortex ring from the surface to form a self-induced jet.

Furthermore, an analysis concerning the circulation of the main vortex ring was performed by comparing cases with and without the internal jet. The result points to a positive correlation between the occurrence of the internal jet and the circulation of the main vortex ring after its complete detachment. Recognizing that the formation of the internal jet is the outcome of a competition between the convective momentum carried with the vortex ring and the viscous dissipation, we defined a special Reynolds number, Re_J, as the criterion for jet formation. It was verified through various droplet coalescence cases that $Re_J > 3.5$ approximately gives the mushroom-like jet and $Re_J < 2.4$ predicts no jet formation, with in-between marking the transition regime.

A mixing index was defined to quantify the effect of the internal jet on mixing. For the cases without internal jet formation, the average mixing rate has a minor dependence on Δ or Oh, reflecting an intrinsic self-similarity associated with the configuration evolution of the two-droplet system during their coalescence. For the cases with internal jet formation, the average mixing rates are however significantly enhanced and the mixing index tends to monotonically increase with increasing Δ or decreasing Oh.

Because Re_J physically characterizes the relative strength of the detached vortex ring, which controls the strength of the forming jet, we compared Re_J among cases of different Δ or Oh to seek a direct correlation between the vortex-induced jet and internal mixing. It was confirmed that the average mixing rate of the vortex-ring detachment stage grows monotonically with Re_J for large Re_J cases with jet formation. It should be noted that the above observations and conclusions only hold for the cases without droplet pinch-off or the tendency of pinch-off, because pinch-off will dramatically reduce the surface energy driving the interface oscillation, which affects the mixing in the jet-formation stage.

8. Summary

In the present thesis, four problem-oriented numerical studies have been conducted based on a VOF method, mainly focusing on the kinetic energy dissipation factor after off-center droplet bouncing for the practical binary droplet collision modelling, the improvement of modelling by considering droplet spinning before collisions, the mass interminglement between two droplets of unequal sizes undergoing off-center collisions and its correlation with the ignition delay time for hypergolic propellants, and vortex-dynamical interpretation of the jet-like “mixing” upon the coalescence between two initially stationary droplets. Specifically, the main conclusions can be summarized as follows:

First, two droplets bouncing undergoing off-center collisions were simulated by using a modified VOF approach with two marker functions which avoids the unphysical numerical coalescence under relatively coarse mesh and increases the computational efficiency substantially. A non-monotonic kinetic energy recovery with varying impact parameter was observed, which is attributed to the enhanced viscous dissipation of moderately off-center collisions. A correlation formula has been proposed that could be useful for the droplet collision modeling in the Lagrangian simulation of sprays, particularly under the elevated gas pressure in the real combustion engines.

Second, by considering the spinning effects of droplets before collisions, the results show that the total kinetic energy recovery for the head-on collision between spinning droplets decrease monotonically with increasing θ from 0 to 90 degree. The helicity analysis was used to identify the “orthogonality” of the translational and spinning movement of droplets, which is the key assumption of the modeling simplification of binary droplet collision into the collision between two mass points by ignoring the droplet spinning effects.

Third, a correlation between the mass interminglement and hypergolic ignition delay time has been established and quantitatively verified by examining the defined “mixing index”. Although the present simulation captured the important physics of droplet mass interminglement that is crucial to the subsequent droplet behaviors, the simulation cannot capture the entire hypergolic ignition process due to the lack in heating and reactions. These absent physical effects should be accounted for in our future studies, including the transport phenomena and chemical reactions in the present VOF simulation.

Forth, a vortex-dynamical interpretation on the fundamental mechanism responsible for forming the internal jet was presented by the evolution of the main vortex ring under three stages of vortex-ring formation, vortex-ring growth, and vortex-ring detachment. The result points to a positive correlation between the occurrence of the internal jet and the circulation of the main vortex ring after its complete detachment. A special Reynolds number, Re_J, was defined as the criterion for jet formation.

Regardless of the effects of size ratio, Weber number, Ohnesorge number, and impact parameter on the above four specific problems, it is noted that the binary droplet collision is a multi-physics, multi-scale, and non-linear problem that includes various other factors influencing the collision dynamics. The future research interests related to the present thesis can be extended to the pressure effects on the binary droplet bouncing, the collision between non-Newtonian droplets, the visualization of the internal mixing between two reactive droplets, and more practically the sprays dynamics involving large amount of binary droplet collision. The experimental technics are still challenging for the microscopic flow field visualization and analysis and merits further developments. Particularly, the highly efficient numerical methods are always desired on the prediction of droplet coalescence and bouncing from the first principle, which is of great significance to understand the fundamental physics of binary droplet collision.

Reference

[1]. Van Dam D.B. and Le Clerc C., *Experimental study of the impact of an ink-jet printed droplet on a solid substrate.* Physics of Fluids, 2004. **16**(9): p. 3403-3414.

[2]. Sirignano W.A., *Fluid dynamics and transport of droplets and sprays*. 1999: Cambridge University Press.

[3]. Heywood J.B., *Internal combustion engine fundamentals*. Vol. 930. 1988: Mcgraw-hill New York.

[4]. Anna S.L., *Droplets and bubbles in microfluidic devices.* Annual Review of Fluid Mechanics, 2016. **48**: p. 285-309.

[5]. Teh S.-Y., Lin R., Hung L.-H. and Lee A.P., *Droplet microfluidics.* Lab on a Chip, 2008. **8**(2): p. 198-220.

[6]. Bird J.C., Dhiman R., Kwon H.-M. and Varanasi K.K., *Reducing the contact time of a bouncing drop.* Nature, 2013. **503**(7476): p. 385.

[7]. Liu T. and Kim C.-J., *Turning a surface superrepellent even to completely wetting liquids.* Science, 2014. **346**(6213): p. 1096-1100.

[8]. Lu Y., Sathasivam S., Song J., Crick C.R., Carmalt C.J. and Parkin I.P., *Robust self-cleaning surfaces that function when exposed to either air or oil.* Science, 2015. **347**(6226): p. 1132-1135.

[9]. Richard D., Clanet C. and Quéré D., *Surface phenomena: Contact time of a bouncing drop.* Nature, 2002. **417**(6891): p. 811.

[10]. Bradley S. and Stow C., *Collisions between liquid drops.* Philosophical Transactions of the Royal Society of London A: Mathematical, Physical and Engineering Sciences, 1978. **287**(1349): p. 635-675.

[11]. Brenn G., *Droplet collision*, in *Handbook of Atomization and Sprays*. 2011, Springer. p. 157-181.

[12].Orme M., *Experiments on droplet collisions, bounce, coalescence and disruption.* Progress in Energy and Combustion Science, 1997. **23**(1): p. 65-79.

[13].Israelachvili J.N., *Intermolecular and surface forces*. 2011: Academic press.

[14].Ashgriz N. and Poo J., *Coalescence and separation in binary collisions of liquid drops.* Journal of Fluid Mechanics, 1990. **221**: p. 183-204.

[15].Tang C., Zhao J., Zhang P., Law C.K. and Huang Z., *Dynamics of internal jets in the merging of two droplets of unequal sizes.* Journal of Fluid Mechanics, 2016. **795**: p. 671-689.

[16].Wang C., Fu S., Kung L. and Law C., *Combustion and microexplosion of collision-merged methanol/alkane droplets.* Proceedings of the Combustion Institute, 2005. **30**(2): p. 1965-1972.

[17].Zhang P. and Law C.K., *An analysis of head-on droplet collision with large deformation in gaseous medium.* Physics of Fluids, 2011. **23**(4): p. 042102.

[18].Popinet S., *Gerris: a tree-based adaptive solver for the incompressible Euler equations in complex geometries.* Journal of Computational Physics, 2003. **190**(2): p. 572-600.

[19].Popinet S., *An accurate adaptive solver for surface-tension-driven interfacial flows.* Journal of Computational Physics, 2009. **228**(16): p. 5838-5866.

[20].Chen X., Ma D. and Yang V. *Collision outcome and mass transfer of unequal-sized droplet collision*. in *50th AIAA Aerospace Sciences Meeting including the New Horizons Forum and Aerospace Exposition*. 2012.

[21].He C., Xia X. and Zhang P., *Non-monotonic viscous dissipation of bouncing droplets undergoing off-center collision.* Physics of Fluids, 2019. **31**(5): p. 052004.

[22]. Liu D., Zhang P., Law C.K. and Guo Y.C., *Collision dynamics and mixing of unequal-size droplets.* International Journal of Heat and Mass Transfer, 2013. **57**(1): p. 421-428.

[23]. Xia X., He C., Yu D., Zhao J. and Zhang P., *Vortex-ring-induced internal mixing upon the coalescence of initially stationary droplets.* Physical Review Fluids, 2017. **2**(11): p. 113607.

[24]. Jiang Y.J., Umemura A. and Law C.K., *An Experimental Investigation on the Collision Behavior of Hydrocarbon Droplets.* Journal of Fluid Mechanics, 1992. **234**: p. 171-190.

[25]. Qian J. and Law C.K., *Regimes of coalescence and separation in droplet collision.* Journal of Fluid Mechanics, 1997. **331**: p. 59-80.

[26]. Adam J.R., Lindblad N.R. and Hendricks D.D., *The Collision, Coalescence, and Disruption of Water Droplets.* Journal of Applied Physics, 1968. **39**(11): p. 5173.

[27]. Brazier-Smith P., Jennings S. and Latham J. *The interaction of falling water drops: coalescence*. in *Proceedings of the Royal Society of London A: Mathematical, Physical and Engineering Sciences*. 1972. The Royal Society.

[28]. Rabe C., Malet J. and Feuillebois F., *Experimental investigation of water droplet binary collisions and description of outcomes with a symmetric Weber number.* Physics of Fluids (1994-present), 2010. **22**(4): p. 047101.

[29]. Pan K.-L., Chou P.-C. and Tseng Y.-J., *Binary droplet collision at high Weber number.* Physical Review E, 2009. **80**(3): p. 036301.

[30]. Estrade J.-P., Carentz H., Lavergne G. and Biscos Y., *Experimental investigation of dynamic binary collision of ethanol droplets–a model for droplet coalescence and bouncing.* International Journal of Heat and Fluid Flow, 1999. **20**(5): p. 486-491.

[31]. Brenn G. and Kolobaric V., *Satellite droplet formation by unstable binary drop collisions.* Physics of fluids, 2006. **18**(8): p. 087101.

[32]. Willis K. and Orme M., *Experiments on the dynamics of droplet collisions in a vacuum.* Experiments in fluids, 2000. **29**(4): p. 347-358.

[33]. Willis K.D. and Orme M.E., *Binary droplet collisions in a vacuum environment: an experimental investigation of the role of viscosity.* Experiments in Fluids, 2003. **34**(1): p. 28-41.

[34]. Gotaas C., Havelka P., Jakobsen H.A., Svendsen H.F., Hase M., Roth N. and Weigand B., *Effect of viscosity on droplet-droplet collision outcome: Experimental study and numerical comparison.* Physics of fluids, 2007. **19**(10): p. 102106.

[35]. Sommerfeld M. and Kuschel M., *Modelling droplet collision outcomes for different substances and viscosities.* Experiments in Fluids, 2016. **57**(12): p. 187.

[36]. Finotello G., Kooiman R.F., Padding J.T., Buist K.A., Jongsma A., Innings F. and Kuipers J., *The dynamics of milk droplet–droplet collisions.* Experiments in Fluids, 2018. **59**(1): p. 17.

[37]. Al-Dirawi K.H. and Bayly A.E., *A new model for the bouncing regime boundary in binary droplet collisions.* Physics of Fluids, 2019. **31**(2): p. 027105.

[38]. O'Rourke P.J., *Collective drop effects on vaporizing liquid sprays*. 1981, Los Alamos National Lab., NM (USA): Ph.D. thesis, Princeton University.

[39]. Brenn G. and Frohn A., *Collision and merging of two equal droplets of propanol.* Experiments in Fluids, 1989. **7**(7): p. 441-446.

[40]. Roth N., Rabe C., Weigand B., Feuillebois F. and Malet J. *Droplet collision outcomes at high Weber number*. in *Proc. 21st Conf. Institute for Liquid Atomization and Spray Systems (IL ASS)*. 2007.

[41]. Pan K.-L., Law C.K. and Zhou B., *Experimental and mechanistic description of merging and bouncing in head-on binary droplet collision.* Journal of Applied Physics, 2008. **103**(6): p. 064901.

[42]. Testik F.Y., *Outcome regimes of binary raindrop collisions.* Atmospheric Research, 2009. **94**(3): p. 389-399.

[43]. Tang C., Zhang P. and Law C.K., *Bouncing, coalescence, and separation in head-on collision of unequal-size droplets.* Physics of Fluids, 2012. **24**(2): p. 022101.

[44]. Anilkumar A., Lee C. and Wang T., *Surface-tension-induced mixing following coalescence of initially stationary drops.* Physics of Fluids A: Fluid Dynamics (1989-1993), 1991. **3**(11): p. 2587-2591.

[45]. Ding H., Li E., Zhang F., Sui Y., Spelt P.D. and Thoroddsen S.T., *Propagation of capillary waves and ejection of small droplets in rapid droplet spreading.* Journal of Fluid Mechanics, 2012. **697**: p. 92-114.

[46]. Zhang F.H., Li E.Q. and Thoroddsen S.T., *Satellite Formation during Coalescence of Unequal Size Drops.* Physical review letters, 2009. **102**(10): p. 104502.

[47]. Chen R.-H., *Diesel–diesel and diesel–ethanol drop collisions.* Applied thermal engineering, 2007. **27**(2): p. 604-610.

[48]. Chen R.-H. and Chen C.-T., *Collision between immiscible drops with large surface tension difference: diesel oil and water.* Experiments in fluids, 2006. **41**(3): p. 453-461.

[49]. Gao T.-C., Chen R.-H., Pu J.-Y. and Lin T.-H., *Collision between an ethanol drop and a water drop.* Experiments in Fluids, 2005. **38**(6): p. 731-738.

[50]. Planchette C., Lorenceau E. and Brenn G., *Binary collisions of immiscible liquid drops for liquid encapsulation.* Fluid dynamics & materials processing, 2011. **7**(3): p. 279-301.

[51]. Roisman I.V., Planchette C., Lorenceau E. and Brenn G., *Binary collisions of drops of immiscible liquids.* Journal of Fluid Mechanics, 2012. **690**: p. 512-535.

[52]. Torza S. and Mason S., *Coalescence of two immiscible liquid drops.* Science, 1969. **163**(3869): p. 813-814.

[53]. Focke C., Kuschel M., Sommerfeld M. and Bothe D., *Collision between high and low viscosity droplets: Direct Numerical Simulations and experiments.* International journal of multiphase flow, 2013. **56**: p. 81-92.

[54]. Blanchette F., Messio L. and Bush J.W., *The influence of surface tension gradients on drop coalescence.* Physics of Fluids (1994-present), 2009. **21**(7): p. 072107.

[55]. Sun K., Zhang P., Che Z. and Wang T., *Marangoni-flow-induced partial coalescence of a droplet on a liquid/air interface.* Physical Review Fluids, 2018. **3**(2): p. 023602.

[56]. Blanchette F., *Simulation of mixing within drops due to surface tension variations.* Physical review letters, 2010. **105**(7): p. 074501.

[57]. Lasheras J., Fernandez-Pello A. and Dryer F., *Initial observations on the free droplet combustion characteristics of water-in-fuel emulsions.* Combustion Science and Technology, 1979. **21**(1-2): p. 1-14.

[58]. Law C.K., *A model for the combustion of oil/water emulsion droplets.* Combustion Science and Technology, 1977. **17**(1-2): p. 29-38.

[59]. Pal R., *A novel method to correlate emulsion viscosity data.* Colloids and Surfaces A: Physicochemical and Engineering Aspects, 1998. **137**(1-3): p. 275-286.

[60]. Chen R.-H., Wang W.-C. and Chen Y.-W., *Like-drop collisions of biodiesel and emulsion diesel.* European Journal of Mechanics-B/Fluids, 2016. **60**: p. 62-69.

[61]. Pan K.L., Tseng Y.H., Chen J.C., Huang K.L., Wang C.H. and Lai M.C., *Controlling droplet bouncing and coalescence with surfactant.* Journal of Fluid Mechanics, 2016. **799**: p. 603-636.

[62]. Planchette C., Lorenceau E. and Brenn G., *The onset of fragmentation in binary liquid drop collisions.* Journal of fluid mechanics, 2012. **702**: p. 5-25.

[63]. Planchette C., Lorenceau E. and Brenn G., *Liquid encapsulation by binary collisions of immiscible liquid drops.* Colloids and Surfaces A: Physicochemical and Engineering Aspects, 2010. **365**(1): p. 89-94.

[64]. Nisisako T., *Recent advances in microfluidic production of Janus droplets and particles.* Current opinion in colloid & interface science, 2016. **25**: p. 1-12.

[65]. Torza S. and Mason S., *Three-phase interactions in shear and electrical fields.* Journal of colloid and interface science, 1970. **33**(1): p. 67-83.

[66]. Pannacci N., Bruus H., Bartolo D., Etchart I., Lockhart T., Hennequin Y., Willaime H. and Tabeling P., *Equilibrium and nonequilibrium states in microfluidic double emulsions.* Physical review letters, 2008. **101**(16): p. 164502.

[67]. Chhabra R.P., *Non-Newtonian fluids: an introduction*, in *Rheology of Complex Fluids*. 2010, Springer. p. 3-34.

[68]. Motzigemba M., Roth N., Bothe D., Warnecke H.J., Prüss J., Wielage K. and Weigan B. *The Effect of Non-Newtonian Flow Behaviour on Binary Droplet Collisions: VOF-Simulation and Experimental Analysis*. in *Proc. 18th Annual Conf. Liquid Atomization and Spray Systems*. 2002. ILASS-Europe.

[69]. Finotello G., De S., Vrouwenvelder J.C., Padding J.T., Buist K.A., Jongsma A., Innings F. and Kuipers J., *Experimental investigation of non-Newtonian droplet*

collisions: the role of extensional viscosity. Experiments in Fluids, 2018. **59**(7): p. 113.

[70]. Focke C. and Bothe D., *Direct numerical simulation of binary off-center collisions of shear thinning droplets at high Weber numbers.* Physics of Fluids (1994-present), 2012. **24**(7): p. 073105.

[71]. Chen X. and Yang V. *Dynamics of Non-Newtonian Liquid Droplet Collision*. in *APS Meeting Abstracts*. 2012.

[72]. Sun K., Wang T., Zhang P. and Law C.K., *Non-Newtonian flow effects on the coalescence and mixing of initially stationary droplets of shear-thinning fluids.* Physical Review E, 2015. **91**(2).

[73]. Sun K., Zhang P., Law C.K. and Wang T., *Collision Dynamics and Internal Mixing of Droplets of Non-Newtonian Liquids.* Physical Review Applied, 2015. **4**(5).

[74]. Ristenpart W., Bird J., Belmonte A., Dollar F. and Stone H.A., *Non-coalescence of oppositely charged drops.* Nature, 2009. **461**(7262): p. 377.

[75]. Huo Y., Wang J., Qiu H., Zuo Z. and Fan Y., *Noncontact rebound and fission of oppositely charged droplets.* Experiments in Fluids, 2015. **56**(3): p. 65.

[76]. Yuan B., He Z., Fang W., Bao X. and Liu J., *Liquid metal spring: oscillating coalescence and ejection of contacting liquid metal droplets.* Science bulletin, 2015. **60**(6): p. 648-653.

[77]. Kavehpour H.P., *Coalescence of drops.* Annual Review of Fluid Mechanics, 2015. **47**: p. 245-268.

[78]. Law C.K., *Combustion physics*. 2010: Cambridge university press.

[79]. Wang C., Lin C., Hung W., Huang W. and Law C., *On the burning characteristics of collision-generated water/hexadecane droplets.* Combustion science and technology, 2004. **176**(1): p. 71-93.

[80]. Zhang D., Zhang P., Yuan Y. and Zhang T., *Hypergolic ignition by head-on collision of N, N, N', N'− tetramethylethylenediamine and white fuming nitric acid droplets.* Combustion and Flame, 2016. **173**: p. 276-287.

[81]. Bach G.A., Koch D.L. and Gopinath A., *Coalescence and bouncing of small aerosol droplets.* Journal of fluid mechanics, 2004. **518**: p. 157-185.

[82]. Stone H.A. and Leal L.G., *Relaxation and breakup of an initially extended drop in an otherwise quiescent fluid.* Journal of Fluid Mechanics, 1989. **198**: p. 399-427.

[83]. Sussman M., Almgren A.S., Bell J.B., Colella P., Howell L.H. and Welcome M.L., *An adaptive level set approach for incompressible two-phase flows.* Journal of Computational Physics, 1999. **148**(1): p. 81-124.

[84]. Tanguy S. and Berlemont A., *Application of a level set method for simulation of droplet collisions.* International journal of multiphase flow, 2005. **31**(9): p. 1015-1035.

[85]. Acevedo-Malavé A. and García-Sucre M., *Coalescence collision of liquid drops I: Off-center collisions of equal-size drops.* AIP Advances, 2011. **1**(3): p. 032117.

[86]. Acevedo-Malavé A. and García-Sucre M., *Coalescence collision of liquid drops II: Off-center collisions of unequal-size drops.* AIP advances, 2011. **1**(3): p. 032118.

[87]. Yue P., Feng J.J., Liu C. and Shen J., *A diffuse-interface method for simulating two-phase flows of complex fluids.* Journal of Fluid Mechanics, 2004. **515**: p. 293-317.

[88]. Yue P., Feng J.J., Liu C. and Shen J., *Diffuse-interface simulations of drop coalescence and retraction in viscoelastic fluids.* Journal of Non-Newtonian Fluid Mechanics, 2005. **129**(3): p. 163-176.

[89]. Sun Z., Xi G. and Chen X., *Numerical simulation of binary collisions using a modified surface tension model with particle method.* Nuclear Engineering and Design, 2009. **239**(4): p. 619-627.

[90]. Zhang Z. and Zhang P., *Kinetic energy recovery and interface hysteresis of bouncing droplets after inelastic head-on collision.* Physics of Fluids, 2017. **29**(10): p. 103306.

[91]. Chen X. and Yang V., *Thickness-based adaptive mesh refinement methods for multi-phase flow simulations with thin regions.* Journal of Computational Physics, 2014. **269**: p. 22-39.

[92]. Coyajee E. and Boersma B.J., *Numerical simulation of drop impact on a liquid–liquid interface with a multiple marker front-capturing method.* Journal of Computational Physics, 2009. **228**(12): p. 4444-4467.

[93]. Kwakkel M., Breugem W.-P. and Boersma B.J., *Extension of a CLSVOF method for droplet-laden flows with a coalescence/breakup model.* Journal of Computational Physics, 2013. **253**: p. 166-188.

[94]. Sun K., Jia M. and Wang T., *Numerical investigation of head-on droplet collision with lattice Boltzmann method.* International Journal of Heat and Mass Transfer, 2013. **58**(1): p. 260-275.

[95]. Sun K., Jia M. and Wang T., *Numerical investigation on the head-on collision between unequal-sized droplets with multiple-relaxation-time lattice Boltzmann model.* International Journal of Heat and Mass Transfer, 2014. **70**: p. 629-640.

[96]. Li J., *Macroscopic model for head-on binary droplet collisions in a gaseous medium.* Physical review letters, 2016. **117**(21): p. 214502.

[97]. Musehane N.M., Oxtoby O.F. and Reddy B.D., *Multi-scale simulation of droplet–droplet interaction and coalescence.* Journal of Computational Physics, 2018. **373**: p. 924-939.

[98]. Rajkotwala A.H., Mirsandi H., Peters E.A.J.F., Baltussen M.W., van der Geld C.W.M., Kuerten J.G.M. and Kuipers J.A.M., *Extension of local front reconstruction method with controlled coalescence model.* Physics of Fluids, 2018. **30**: p. 022102.

[99]. Liu M. and Bothe D., *Toward the predictive simulation of bouncing versus coalescence in binary droplet collisions.* Acta Mechanica, 2019: p. 1-22.

[100]. Sussman M., Fatemi E., Smereka P. and Osher S., *An improved level set method for incompressible two-phase flows.* Computers & Fluids, 1998. **27**(5-6): p. 663-680.

[101]. Sussman M. and Puckett E.G., *A coupled level set and volume-of-fluid method for computing 3D and axisymmetric incompressible two-phase flows.* Journal of computational physics, 2000. **162**(2): p. 301-337.

[102]. Cummins S.J., Francois M.M. and Kothe D.B., *Estimating curvature from volume fractions.* Computers & structures, 2005. **83**(6-7): p. 425-434.

[103]. Popinet S., *Numerical models of surface tension.* Annual Review of Fluid Mechanics, 2018. **50**: p. 49-75.

[104]. Chen X., Ma D., Khare P. and Yang V. *Energy and mass transfer during binary droplet collision*. in *49th AIAA Aerospace Sciences Meeting Including the New Horizons Forum and Aerospace Exposition*. 2011.

[105]. Thoraval M.-J., Takehara K., Etoh T.G., Popinet S., Ray P., Josserand C., Zaleski S. and Thoroddsen S.T., *von Kármán vortex street within an impacting drop.* Physical review letters, 2012. **108**(26): p. 264506.

[106]. Thoraval M.-J., Takehara K., Etoh T. and Thoroddsen S.T., *Drop impact entrapment of bubble rings.* Journal of Fluid Mechanics, 2013. **724**: p. 234-258.

[107]. Xia X., He C. and Zhang P., *Scalings in Coalescence of Liquid Droplets.* arXiv preprint arXiv:1803.05789, 2018.

[108]. Sun K., Zhang P., Jia M. and Wang T., *Collision-induced jet-like mixing for droplets of unequal-sizes.* International Journal of Heat and Mass Transfer, 2018. **120**: p. 218-227.

[109]. Krishnan K. and Loth E., *Effects of gas and droplet characteristics on drop-drop collision outcome regimes.* International Journal of Multiphase Flow, 2015. **77**: p. 171-186.

[110]. Reitter L., Liu M., Breitenbach J., Huang K.-L., Bothe D., Brenn G., Pan K.-L., Roisman I. and Tropea C. *Experimental and Computational Investigation of binary drop collisions under elevated pressure*. in *Ilass Europe. 28th european conference on Liquid Atomization and Spray Systems*. 2017. Editorial Universitat Politècnica de València.

[111]. Zhang Z., Chi Y., Shang L., Zhang P. and Zhao Z., *On the role of droplet bouncing in modeling impinging sprays under elevated pressures.* International Journal of Heat and Mass Transfer, 2016. **102**: p. 657-668.

[112]. Zhang Z. and Zhang P., *Cross-impingement and combustion of sprays in high-pressure chamber and opposed-piston compression ignition engine.* Applied Thermal Engineering, 2018. **144**: p. 137-146.

[113]. Zhang Z. and Zhang P., *Modeling kinetic energy dissipation of bouncing droplets for Lagrangian simulation of impinging sprays under high ambient pressures.* Atomization and Sprays, 2018. **28**(8).

[114]. Tang X., Saha A., Law C.K. and Sun C., *Bouncing drop on liquid film: Dynamics of interfacial gas layer.* Physics of Fluids, 2019. **31**(1): p. 013304.

[115]. Tang X., Saha A., Law C.K. and Sun C., *Bouncing-to-merging transition in drop impact on liquid film: Role of liquid viscosity.* Langmuir, 2018. **34**(8): p. 2654-2662.

[116]. Blanchette F., *Modeling the vertical motion of drops bouncing on a bounded fluid reservoir.* Physics of Fluids, 2016. **28**(3): p. 032104.

[117]. Hu C., Xia S., Li C. and Wu G., *Three-dimensional numerical investigation and modeling of binary alumina droplet collisions.* International Journal of Heat and Mass Transfer, 2017. **113**: p. 569-588.

[118]. Sakakibara B. and Inamuro T., *Lattice Boltzmann simulation of collision dynamics of two unequal-size droplets.* International journal of heat and mass transfer, 2008. **51**(11-12): p. 3207-3216.

[119]. Munnannur A. and Reitz R.D., *Comprehensive collision model for multidimensional engine spray computations.* Atomization and Sprays, 2009. **19**(7).

[120]. Gotaas C., Havelka P., Jakobsen H.A. and Svendsen H.F., *Evaluation of the impact parameter in droplet-droplet collision experiments by the aliasing method.* Physics of fluids, 2007. **19**(10): p. 102105.

[121]. White F.M. and Corfield I., *Viscous fluid flow*. Vol. 3. 2006: McGraw-Hill New York.

[122]. Aumann R., McCracken M. and Abraham J., *An evaluation of a composite model for predicting drop-drop collision outcomes in multidimensional spray computations.* SAE Transactions, 2002: p. 1593-1601.

[123]. Post S.L. and Abraham J., *Modeling the outcome of drop–drop collisions in Diesel sprays.* International Journal of Multiphase Flow, 2002. **28**(6): p. 997-1019.

[124]. Hill R. and Eaves L., *Nonaxisymmetric shapes of a magnetically levitated and spinning water droplet.* Physical review letters, 2008. **101**(23): p. 234501.

[125]. Brown R. and Scriven L., *The shape and stability of rotating liquid drops.* Proceedings of the Royal Society of London. A. Mathematical and Physical Sciences, 1980. **371**(1746): p. 331-357.

[126]. Maneshian B., Javadi K., Rahni M.T. and Miller R., *Droplet dynamics in rotating flows.* Advances in colloid and interface science, 2016. **236**: p. 63-82.

[127]. Kitahata H., Tanaka R., Koyano Y., Matsumoto S., Nishinari K., Watanabe T., Hasegawa K., Kanagawa T., Kaneko A. and Abe Y., *Oscillation of a rotating levitated droplet: Analysis with a mechanical model.* Physical Review E, 2015. **92**(6): p. 062904.

[128]. Janiaud E., Elias F., Bacri J., Cabuil V. and Perzynski R., *Spinning ferrofluid microscopic droplets.* Magnetohydrodynamics, 2000. **36**(4): p. 301-314.

[129]. Bernando C., Tanyag R.M.P., Jones C., Bacellar C., Bucher M., Ferguson K.R., Rupp D., Ziemkiewicz M.P., Gomez L.F. and Chatterley A.S., *Shapes of rotating superfluid helium nanodroplets.* Physical Review B, 2017. **95**(6): p. 064510.

[130]. Cresswell R. and Morton B., *Drop-formed vortex rings—The generation of vorticity.* Physics of Fluids, 1995. **7**(6): p. 1363-1370.

[131]. Agbaglah G., Thoraval M.-J., Thoroddsen S.T., Zhang L.V., Fezzaa K. and Deegan R.D., *Drop impact into a deep pool: vortex shedding and jet formation.* Journal of fluid mechanics, 2015. **764**.

[132]. Zhang D., He C., Zhang P. and Tang C., *Mass interminglement and hypergolic ignition of TMEDA and WFNA droplets by off-center collision.* Combustion and Flame, 2018. **197**: p. 276-289.

[133]. Jiang Y.J., Umemura A. and Law C.K., *An Experimental Investigation on the Collision Behavior of Hydrocarbon Droplets.* J. Fluid Mech., 1992. **234**: p. 171-190.

[134]. Qian J. and Law C.K., *Regimes of coalescence and separation in droplet collision.* J. Fluid Mech., 1997. **331**: p. 59-80.

[135]. Landau L.D. and Lifshitz E.M., *Course of theoretical physics*. 2013: Elsevier.

[136]. Saffman P.G., *Vortex dynamics*. 1992: Cambridge university press.

[137]. Davis S.M. and Yilmaz N., *Advances in hypergolic propellants: Ignition, hydrazine, and hydrogen peroxide research.* Advances in Aerospace Engineering, 2014. **2014**.

[138]. Erik D., Kevin C., Timothée P. and Stephen H., *Ignition of Advanced Hypergolic Propellants*, in *46th AIAA/ASME/SAE/ASEE Joint Propulsion Conference & Exhibit*. 2010, American Institute of Aeronautics and Astronautics.

[139]. Wang S. and Thynell S., *An experimental study on the hypergolic interaction between monomethylhydrazine and nitric acid.* Combustion and Flame, 2012. **159**(1): p. 438-447.

[140]. Law C.K., *Fuel options for next-generation chemical propulsion.* Aiaa Journal, 2012. **50**(1): p. 19-36.

[141]. Inamuro T., Tajima S. and Ogino F., *Lattice Boltzmann simulation of droplet collision dynamics.* International journal of heat and mass transfer, 2004. **47**(21): p. 4649-4657.

[142]. Sun Z., Xi G. and Chen X., *Mechanism study of deformation and mass transfer for binary droplet collisions with particle method.* Physics of fluids, 2009. **21**(3): p. 032106.

[143]. Yeh S.-I., Fang W.-F., Sheen H.-J. and Yang J.-T., *Droplets coalescence and mixing with identical and distinct surface tension on a wettability gradient surface.* Microfluidics and nanofluidics, 2013. **14**(5): p. 785-795.

[144]. Nobari M. and Tryggvason G., *The flow induced by the coalescence of two initially stationary drops.* 1994.

[145]. Batchelor C.K. and Batchelor G., *An introduction to fluid dynamics*. 2000: Cambridge university press.

[146]. Thoraval M.-J., Li Y. and Thoroddsen S.T., *Vortex-ring-induced large bubble entrainment during drop impact.* Physical Review E, 2016. **93**(3): p. 033128.

[147]. Thoroddsen S., Takehara K. and Etoh T., *The coalescence speed of a pendent and a sessile drop.* Journal of Fluid Mechanics, 2005. **527**: p. 85-114.

[148]. Eggers J., Lister J.R. and Stone H.A., *Coalescence of liquid drops.* Journal of Fluid Mechanics, 1999. **401**: p. 293-310.

[149]. Wu M., Cubaud T. and Ho C.-M., *Scaling law in liquid drop coalescence driven by surface tension.* Physics of Fluids, 2004. **16**(7): p. L51-L54.

[150]. Aarts D.G., Lekkerkerker H.N., Guo H., Wegdam G.H. and Bonn D., *Hydrodynamics of droplet coalescence.* Physical review letters, 2005. **95**(16): p. 164503.

[151]. Gharib M., Rambod E. and Shariff K., *A universal time scale for vortex ring formation.* Journal of Fluid Mechanics, 1998. **360**: p. 121-140.

[152]. Shusser M. and Gharib M., *Energy and velocity of a forming vortex ring.* Physics of Fluids, 2000. **12**(3): p. 618-621.

[153]. Mohseni K., Ran H. and Colonius T., *Numerical experiments on vortex ring formation.* Journal of Fluid Mechanics, 2001. **430**: p. 267-282.

[154]. Lundgren T. and Koumoutsakos P., *On the generation of vorticity at a free surface.* Journal of Fluid Mechanics, 1999. **382**: p. 351-366.